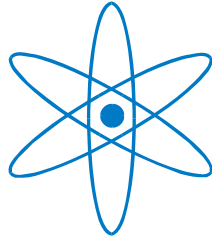


PHYSICS–DEPARTMENT

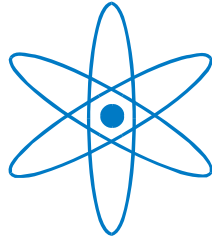


Optimization of the Relation between
Image Quality and Dose in
Pediatric Projection Radiography
(Exemplified by the Examination of the Chest)

Dissertation

Felix H Schöfer

PHYSIK-DEPARTMENT



Optimierung der Relation von Bildqualität
und Dosis in der pädiatrischen
Projektionsradiographie
(am Beispiel von Thoraxuntersuchungen)

Dissertation

Felix H Schöfer

Technische Universität München

Physik-Department

Optimization of the Relation between Image Quality and Dose

in Pediatric Projection Radiography

(Exemplified by the Examination of the Chest)

Felix H. Schöfer

Vollständiger Abdruck der von der Fakultät für Physik

der Technischen Universität München zur Erlangung des akademischen Grades eines

Doktors der Naturwissenschaften

genehmigten Dissertation.

Vorsitzender: Univ.-Prof. Dr. J. L. van Hemmen

Prüfer der Dissertation:

1. Hon.-Prof. Dr. H. G. Paretzke

2. Univ.-Prof. Dr. K. Schreckenbach

Die Dissertation wurde am 22.11.2007 bei der Technischen Universität München

eingereicht und durch die Fakultät für Physik

am 28.04.2008 angenommen.



NATIONAL RESEARCH CENTER FOR
ENVIRONMENT AND HEALTH

MEMBER OF THE HELMHOLTZ ASSOCIATION



TECHNISCHE UNIVERSITÄT

MÜNCHEN

THIS IS DEDICATED
TO THE ONES I LOVE

1 Abstract

This work is aiming at the optimization of the relation between image quality and dose in digital pediatric projection radiography.

Today's application of X-ray tube technology is leading to a wide spectrum of exposures. In conventional analogue techniques there exist definite relations between image generation and visualization. Thus for example the choice of a screen-film combination fixes the dependence of the film blackening from the exposure. In contrast digital radiographic methods allow the flexible adaptation of the image visualization to a clinical question even after the image generation. This fact necessitates a physically substantiated optimization of the image generation process. Its quality fixes the relation between the information content of the image and the exposure required.

The optimization presented in this work is concentrated on thorax projection radiography of premature and newborn children. Here high demands on the imaging quality, a relatively high frequency of the examination and significant size variations of the individual patients are connected with their increased radiation sensitivity.

This work is mainly based on three different approaches, namely Monte Carlo x-ray photon transport calculations of anthropomorphic and physical phantoms, analytical modeling and phantom experiments at clinical X-ray systems. It relies mainly on the consideration of large area contrasts. The results of the different approaches especially for optimal photon energies are in good agreement.

The highest exposure and highest necessary photon energy is always needed for the lowest contrast to be resolved in the thickest or most dense part of a patient. The optimal range of photon energy becomes smaller for thinner specimens. This clearly stresses the need for individual optimization especially in pediatric radiology.

The optimal use of digital detectors in pediatric radiology allows fewer repetitions for thoracic investigations due to higher information content and lower doses especially for the youngest patients.

2 Table of Contents

1	ABSTRACT	1
2	TABLE OF CONTENTS	2
3	INTRODUCTION AND CONCEPT	4
3.1	INTRODUCTION	4
3.2	CONCEPT	4
4	BASICS.....	7
4.1	OPTIMIZATION OF IMAGE QUALITY AND DOSE IN PEDIATRIC RADIOLOGY	7
4.2	IMAGING THEORY	9
4.2.1	<i>Basic Imaging Theory</i>	9
4.2.2	<i>Rose Model</i>	12
4.2.3	<i>Detective Quantum Efficiency</i>	13
4.3	DOSIMETRIC MEASUREMENT CATEGORIES AND UNITS	17
4.3.1	<i>Interaction of Photon Radiation and Matter</i>	17
4.3.2	<i>Dosimetric Quantities</i>	22
4.3.3	<i>Beam Quality</i>	24
4.4	RISK ESTIMATION	25
4.5	MONTE CARLO RADIATION TRANSPORT CALCULATIONS	27
4.5.1	<i>History and Introduction</i>	27
4.5.2	<i>EGS Code System</i>	29
5	CALCULATIONS.....	31
5.1	MONTE CARLO RADIATION TRANSPORT CALCULATIONS	31
5.1.1	<i>Monte Carlo Calculation of the Imaging Process</i>	31
5.1.2	<i>Tomographic Phantom</i>	35
5.1.3	<i>Step Phantom</i>	41
5.1.4	<i>Error Discussion for Monte Carlo Simulations</i>	42
5.1.5	<i>Results of the Monte Carlo Calculations</i>	43
5.2	CONNECTION BETWEEN IMAGE INFORMATION AND EXPOSURE	56
5.2.1	<i>Model</i>	56
5.2.2	<i>Results for Large Area Contrast</i>	62
5.2.3	<i>Results for Areal Resolution</i>	72
5.2.4	<i>Results for Noise Consideration</i>	73
6	MEASUREMENTS.....	75
6.1	X-RAY TUBE BEHAVIOR.....	75
6.2	IMAGING AND IMAGE EVALUATION	80
6.3	IMAGING PROPERTIES OF CLINICAL CR SYSTEMS	83

7	CONCLUSIONS AND OUTLOOK.....	89
7.1	CONCLUSION	89
7.2	OUTLOOK	92
8	LIST OF REFERENCES.....	94
APPENDIX.....		99
A	LIST OF FIGURES.....	99
B	ACKNOWLEDGEMENTS	103
C	EXAMPLE OF MATHEMATICA CODE FOR MODEL CALCULATIONS	104
D	CURRICULUM VITAE.....	113
	<i>D.i Contact Information.....</i>	<i>113</i>
	<i>D.ii Private Information.....</i>	<i>113</i>
	<i>D.iii Education</i>	<i>113</i>
	ERKLÄRUNG.....	115

3 Introduction and Concept

3.1 Introduction

This work is aiming at the optimization of the relation between image quality and dose in digital pediatric projection radiography considering in particular thoracic imaging.

The development of digital techniques offers new chances and challenges in the process of optimization between image quality and exposure. In conventional radiography there are definite relations between image generation and visualization. For example the choice of a screen-film combination fixes the dependence of the film blackening from the exposure. In contrast digital radiographic methods allow the flexible adaptation of the image visualization to a clinical question even after the image generation. The optimization of the image generation process itself is fundamental as its quality fixes the relation between the information content and the exposure employed. For this optimization inevitable influences of image processing had to be compensated for.

Thorax projection radiography has very high demands regarding the imaging quality in respect to object size, image contrast and dynamic range. The plane image of the thorax is still the most frequent radiological examination [1].

In pediatric radiology the great variation of the patient dimensions in a range of low overall contrast demands the individual matching of the radiological setup. Also because of the sensitivity of the younger patients the effects of x-ray radiation exposure are expected to be most harmful, the effort to optimize radiography is promising significant improvements.

This work concentrates on large area contrast consideration comparable to the imaging of pneumonia. This provides the opportunity for direct examination of image properties for each region of an image separately. In contrast especially the determination of the noise level for a small contrast detail by experiments is not easily possible. Some theoretical proposals for the extension of the results to detail contrast imaging are made.

The evaluation and optimization methods used for chest imaging in pediatric digital radiography are expected to be applicable in various fields of digital radiology.

3.2 Concept

Optimization in medical radiology means that the irradiation is brought to a level where a further increase would turn around the relation between the benefit of additive diagnostic information and the detriment of additional radiation risk.

In this work the actual optimization process was divided into three major parts which are building up on top of one another. These are

- a) Monte Carlo x-ray photon transport simulations,
- b) direct calculations performed at a model imaging system, and
- c) phantom experiments in the clinical environment.

After giving fundamental information about these different approaches (chapter 4) the application of the methods and the results are presented:

Monte Carlo calculations of photon transport and energy deposition were performed in order to study qualitatively the spectral absorption behavior in pediatric x-ray imaging in respect to the imaging process and the dose quantities absorbed by different organs of the patient. The calculations are making use of an anatomically shaped virtual model of an eight week old baby [2]. This so-called Voxel-model has been rescaled in this work to fit the dimensions of a premature or newborn child. The dataset was derived from data obtained by computed tomography. The main advantage of models like this one is their realistic dimensioning of organs, tissues, and skeleton of the baby. Therefore it delivers most realistic results for organ and total body equivalent doses and photon transport in general. It belongs to a family of Voxel-models created at the GSF [3] from which now models were modified to represent ICRP reference man [4, 5]. The adoption of the dimensions of a real child is expected to make the results of the performed calculations somewhat individual. It should be stressed that this was wanted for all previous models used for Monte Carlo calculations. The previously used mathematical models are composed by combinatorial geometry mathematical expressions describing plane, cylindrical, conical, spherical or elliptical surfaces approximating an “average” human being. Now as the accuracy of the voxel-models is so high that individual properties gain relevance [3]. This leads for example to the necessity to examine the influence of dimension changes onto the results [6, 7]. In this work methods were developed in order to gain information about the radiographic properties of an individual represented by a voxel-model. These methods were implemented into a preexisting software code developed to perform dosimetric calculations (e.g. [5, 8]) using the Monte Carlo radiation transport calculation system EGSnrc [9]. The resulting system was applied to the virtual model of a premature infant.

The simulations were performed in order to analyze the influence different irradiation setups used in pediatric thorax radiology have on image quality and dose. One main interest is to find out about the relative change in radiation exposure with different irradiation parameters, such

as filtering and tube voltage and current. Additionally the share of incident radiation was calculated that is getting through the phantom to an imaging screen and the distribution was imaged. This helped to characterize the voxel-phantom as a specimen of projection imaging. The calculations were performed for a set of monoenergetic photon fields in order to gain a clear view of the physical properties of the phantom as well as for different photon fields of the spectral composition adapted to clinical x-ray tube units.

The results of the simulation allow the prediction of doses connected with a radiographic examination and give first information about the dose reduction possibilities.

Numerical calculations of photon statistics for different settings of primary radiation, filtering, and detector parameters are performed aiming for dose reduction and improvement of image quality. The simulations give input parameters for the optimization process connecting properties of the applied radiation to organ and effective doses. They connect exposure parameters to quantities describing the possible detriment for a pediatric patient.

In a second step a connection between the physical properties of a radiographic exposure and the quality of the image is calculated quantitatively. For this purpose a mathematical model is designed in order to quantify the information gain connected to a rise of the applied dose. It is built up from modules connected to the different parts of a digital imaging system like radiation source, observation setup and detection method. This was in order to allow step by step the inclusion of all information available about realistic clinical x-ray units and patient properties. The model quantifies the expense needed in order to fulfill a fundamental imaging task and how the expense changes with changing parameters that define that task. Modifications allow the application of the results in clinical application.

Thirdly experiments were performed in different pediatric x-ray departments in order to substantiate the theoretical results found and relate them to real clinical radiographic systems. The measurements mainly concentrated on image analysis and included the analysis of the x-ray units' radiation power up, running and shut down characteristics. The digital representation of the radiographs offers the advantage of computed analysis by the concepts developed in this work. The information contents of such images were evaluated in comparison to the needs for reliable diagnostic findings in the clinical environment.

4 Basics

Digitalization of radiography has led to the need for a new approach to optimization. Concepts of optimization established in classic radiography have to be reviewed (cf. section 4.1) and adapted to the digital imaging process. It is also essential to base this optimization on the review of established theories describing the quality of an imaging process (cf. section 4.2), established methods of dosimetry (cf. section 4.3) and attribution of a risk to medical x-ray exposures (cf. section 4.4). The last the use of Monte Carlo radiation transport calculations for this work is constituted (cf. section 4.5).

4.1 Optimization of Image Quality and Dose in Pediatric Radiology

The establishment of digital methods in digital radiography has led to the necessity of a new approach for the optimization of radiological methods. In this field the radiography of the thorax as one of the most frequent examination [1] and as an examination demanding high image quality over a large dynamic range of the image is challenging [10]. A minimization of the applied dose and the optimization of the image quality for avoidance of unnecessary repetition are highly desirable. Pediatric radiology combines this with increased sensitivity of the patient [11] and lower radiographic contrast. Therefore methods developed in this work were applied to pediatric thoracic radiography.

In screen-film imaging there is a practical optimal dose for the adaptation of the imaging characteristics to the structures that are to be seen: small doses lead to insufficient optical density of the film, high doses bring about the loss of structures of interest in blackened parts of the image. This is in contrast to digital radiology where higher exposures generally (and unfortunately) result in improved image quality. Image processing makes it possible to transfer the information gained into pictures similar to conventional x-ray images. Optimization of digital radiography indicates a rise in the applied dose as long as the connected improvement of diagnostic information is justifying the rise of the risk attributed to the x-ray exposure (cf. chapter 4.4). In practice the exposure is often increased until a maximum of diagnostic significance of the images is reached. However the pictures should better be taken at the lower limit of dose securely leading to the desired and needed diagnostic information. For this way of optimization which connects applied dose and information gain this work provides a theoretical analysis (chapter 5.2) and confirms the results by comparison to the results of experiments and photon transport calculations.

Connected with classical film and intensifying screen systems optimizations have accompanied decades of clinical application. Reductions of exposure have been reached by screen-film combinations of higher sensitivity, pre-filtration of the applied radiation in order to reduce the share of low energy radiation, the use of moving grids eliminating scattered radiation, and the improvement of the training of the staff. The special demands in pediatric imaging have been examined in many studies (e.g. [12-16]). The European guidelines on quality criteria for diagnostic radiographic images in pediatrics [13] give information about general principles associated with optimal imaging performance. They provide recommendations for the technical adjustment of the examination setup and diagnostic image criteria which allow for the assessment of the diagnostic quality of an x-ray procedure. The guidelines have been developed from experience in pediatric screen-film radiography. Some of the recommendations e.g. about the omitting of an anti-scatter grid can be applied directly for digital techniques, too. In spite of that it is not possible to translate the statements concerning optimal radiographic beam quality - depending on peak voltage and filtration - directly into the application in digital radiography systems. Recommendations aim at the optimum reproduction of clinically relevant structures in connection with the characteristic curve of the chosen screen-film system. The choice of the system itself imposes necessities of the production of film emulsions and amplification screens onto the system. In contrast to that characteristic curves implemented in digital imaging systems are extremely flexible by mathematical processing of image data. As soon as the resolution of digital radiography became comparable to conventional systems this advantage was one of the decisive factors for digital systems gaining importance. It is possible to evaluate one dataset by application of "characteristic curves" adapted to each specific structure that is to be visualized. In addition to the optimization of this adapted post processing the imaging system of radiation source, patient and detector has to deliver the imaging information.

The image processing has to be evaluated mainly based on studies about its influence on clinical quality criteria like in observer performance studies [17]. This work in contrast provides methods that assess the information gain by application and detection of x-ray quanta. They are based on direct evaluation of the information content using physical measures like contrast to noise ratio and modulation transfer measured with phantoms. The information content was related to quantities of radiation quality and patient exposure and through that ideally to risk estimates for the individual patient.

4.2 Imaging Theory

Basics of modern imaging theory applied to digital radiography have been developed over 50 years ago [18]. Theories have been developed by the assumption of linear behavior [19, 20] and the application of Fourier methods to quantum imaging [21, 22]. Reviews about the assessment of image quality in Medical imaging are published [17]. In the following the theoretical concepts this work is based on are introduced.

4.2.1 Basic Imaging Theory

A starting point for imaging theory is the spatial distribution of observable unit quanta in the imaging plane, the quantum image $q(\vec{r})$. If there is no property useful for individual discrimination of the image quanta, the quantum image can be represented by a sum of delta functions [19]:

$$\text{Eq. 4.2-1: } q(\vec{r}) = \sum_{i=1}^{N_q} \delta(\vec{r} - \vec{r}_i)$$

where \vec{r} is the spatial position vector, N_q is the number of incident quanta, \vec{r}_i represents the position of quantum i , and $\delta(\vec{r} - \vec{r}_i)$ is the Dirac delta function. In screen-film systems the quantum image is transformed into the analog image which is described by a spatially varying function $d(\vec{r})$ of optical density. In digital imaging the transformation produces an array of numerical values, the digital image d_n . Analog and digital images are treated analogous either in discrete operations on d_n or continuous operations on $d(\vec{r})$ (e.g. summation or integral).

In linear systems theory whole imaging systems can be split up into a cascade of transformations of the image content for stepwise analysis. Each transformation – e.g. the conversion of $q(r)$ to $d(r)$ or d_n or the conversion from $d(r)$ to d_n – is described by a linear function:

$$\text{Eq. 4.2-2: } S(\tilde{d} + d) = S(\tilde{d}) + S(d)$$

$$\text{Eq. 4.2-3: } S(\alpha \cdot d) = \alpha \cdot S(\tilde{d})$$

with d and \tilde{d} representing images of one kind, α an arbitrary real number and S the imaging function. The restriction to linear transformations in the context of digital radiography as in the context of radiography in general is an approximation (cf. chapter 5.2).

For large homogeneous areas of images transfer factors are defined which describe the change of image properties by the process. The “contrast transfer factor” relates differences relative to

the overall signal before and after the imaging process. The transfer factor relating the number of incident quanta and the number of quanta detected is the “quantum efficiency”. It is determined by the examination of the noise properties of the image of a homogeneous area (cf. chapter 4.2.2)

Quantum imaging processes are stochastic: if experiments are repeated the results are subject to variation. In order to describe these variations the “noise variance” σ_d^2 is introduced as

$$\text{Eq. 4.2-4:} \quad \sigma_d^2 = \langle (d - \langle d \rangle)^2 \rangle$$

where d represents an image ($q(\vec{r})$, $d(\vec{r})$ or d_n) and $\langle d \rangle$ denotes the expectation value of d . In general the expectation value is found by averaging over many equivalent representations of the image at one point, but as radiographic imaging systems are ergodic, repetitions of the imaging process can be avoided: expectation values as averages at a particular location in many realizations can be taken to be equal to spatial averages about homogeneous regions. All statistics can be determined from a single realization [22].

The characteristics of imaging data sets are taken to result from statistically independent point processes and fully described by Poisson statistics. One of the consequences is that all properties of an imaging process can be summed up from its “impulse response function” or - in the two-dimensional case - its “point spread function” (PSF). It is defined as

$$\text{Eq. 4.2-5:} \quad \text{irf}(\vec{r}, \vec{r}_i) := S(\delta(\vec{r} - \vec{r}_i)).$$

The PSF describes the blur produced by an infinitely sharp point as imaged by a sensor (Figure 4.2-1). It can be computed from the modulation transfer function, which is its Fourier transform (cf. section 4.2.3.1).

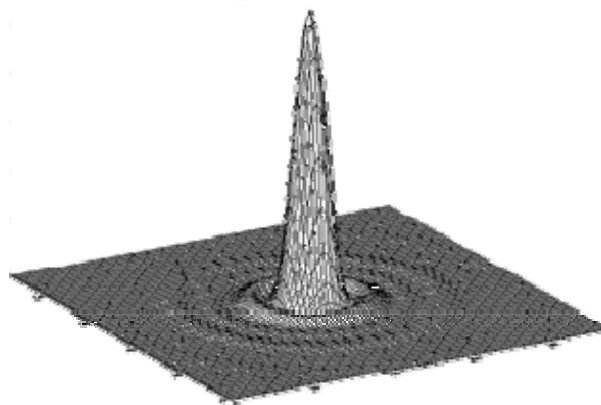


Figure 4.2-1: Typical shape of a Point Spread Function.

The image of an analogue function $d(\vec{r})$ can be calculated as its convolution with the impulse response function:

$$\text{Eq. 4.2-6: } S(d(\vec{r})) = \int d(\vec{r}') \cdot \text{irf}(\vec{r} - \vec{r}') d\vec{r}'.$$

In translation invariant systems it is optimally determined from images of line or step functions (cf. section 4.2.3.2).

Two other important functions characterizing images $d(\vec{r})$ are the autocorrelation function $R_d(\vec{r}, \vec{r} + \vec{r}')$ as a measure of average crosstalk and the autocovariance $K_d(\vec{r}, \vec{r} + \vec{r}')$ as a measure of noise crosstalk. In shift invariant systems both are independent of the position in the image r :

$$\text{Eq. 4.2-7: } R_d(\vec{r}') = \langle d(\vec{r}) \cdot d^*(\vec{r} + \vec{r}') \rangle$$

$$\text{Eq. 4.2-8: } K_d(\vec{r}') = \langle (d(\vec{r}) - \langle d(\vec{r}) \rangle) \cdot (d^*(\vec{r} + \vec{r}') - \langle d^*(\vec{r} + \vec{r}') \rangle) \rangle$$

where d^* is the complex conjugate of d .

The discrete counterparts for these two equations for pixel values of digital imaging are

$$\text{Eq. 4.2-9: } R_{d_n}(n') = \langle d_n \cdot d_{n+n'}^* \rangle$$

$$\text{Eq. 4.2-10: } K_{d_n}(n') = \langle (d_n - \langle d_n \rangle) \cdot (d_{n+n'}^* - \langle d_{n+n'}^* \rangle) \rangle$$

Digital imaging of a photon field produces measurements on a regular pattern of detectors. The distances between neighboring points in this pattern are the “sampling lengths”. The process is modeled as a sampling operation making use of the so-called “sifting property” of the delta function picking image values at the sampling points. In one-dimension the sampling $d^+(x)$ of an analog function $d(x)$ with a sampling length x_0 is

$$\text{Eq. 4.2-11: } d^+(x) = d(x) \sum_{n=-\infty}^{\infty} \delta(x - nx_0).$$

The original function can be fully reconstructed from its sample function if the sampling distance is smaller than half the inverse of the highest spatial frequency it contains [21]. The highest spatial frequency that can be reconstructed after equidistant sampling is called the “Nyquist frequency” of a system. Spatially periodic signals of higher frequencies present before sampling can lead to artifacts in the low spatial frequency range of the sampling result. These so-called “aliasing artifacts” can be understood as a Moiré pattern created by the overlay

of the pixel pattern defining one spatial frequency and structures in the object that are periodic at a spatial frequency higher than half that frequency.

4.2.2 Rose Model

In radiography as in general imaging quantum fluctuations are ultimately limiting system performance. In evaluation of the quality of an imaging process this limit has to be specified and can be used as a benchmark. In the 1940s Albert Rose lay important theoretical and experimental foundations in this process [18]. The work was consistent with earlier work on signal transfer theory in telegraphy [23].

Rose designed a model in order to introduce a signal difference to noise ratio (ΔSNR_{Rose}), a quantity is clearly defined and accessible for experiments. The model is based on a system imaging a uniform object of area A in a uniform background. The contrast C was defined as the relative change of the mean number q_o of quanta detected per unit area in the region of the object in relation to the mean number q_b of quanta per unit area in the background region:

$$\text{Eq. 4.2-12: } C = \frac{q_o - q_b}{q_b}.$$

The Rose signal difference ΔS_{Rose} is defined as the difference between the mean number of quanta in the area connected to the object and in an area A in the region of the background of the same size:

$$\text{Eq. 4.2-13: } \Delta S_{Rose} := (q_o - q_b) \cdot A$$

Rose defined noise as the standard deviation σ_b of q_b in an area equal to A in the background region. The property of uncorrelated quanta forming the image directly leads to Poisson statistics in the behavior of σ_b :

$$\text{Eq. 4.2-14: } \sigma_b = \sqrt{A \cdot q_b}$$

The Rose Signal to Noise Ratio ΔSNR_{Rose} is defined as the quotient of ΔS_{Rose} and σ_b :

$$\text{Eq. 4.2-15: } \Delta SNR_{Rose} := \frac{(q_o - q_b) \cdot A}{\sqrt{A \cdot q_b}}$$

It turns out to be directly proportional to the contrast C as well as linearly connected to the square root of the number of incident quanta:

$$\text{Eq. 4.2-16: } \Delta SNR_{Rose} = C \cdot \sqrt{A \cdot q_b}$$

This model was designed in order to find the values for ΔSNR_{Rose} that are required in order to detect uniform objects in photon-noise-limited images. Rose searched for the minimal ΔSNR_{Rose} for this task experimentally.

Rose's results were the first ones to stress that an imaging system will always suffer limitations from the quantum nature of the imaging process: there is a minimal noise level present that is directly connected to the number of input quanta. This minimal noise level can be compared with the noise present in the image. This leads to a measure of system performance in imaging large homogeneous areas called the "quantum efficiency" (cf. section 4.2.1). It has been developed further into a spatial-frequency-dependent quantity (cf. section 4.2.3).

The quantum limit to imaging performance is especially important for techniques where the number of quanta is to be minimized like in every medical radiographic imaging procedure. The concepts derived in the Rose Model are fundamental for every analysis of image properties performed in this work (cf. chapter 5.1 and part 6). The model is modified in order to find a quantitative measure of system performance: The experimental search for a minimal signal to noise ratio is replaced by the calculation relying on the clear definition of an imaging task (cf. chapter 5.2).

4.2.3 Detective Quantum Efficiency

4.2.3.1 Definition of the Detective Quantum Efficiency

The modeling of spatial-frequency-dependent properties of imaging processes is efficiently performed in the Fourier representation. This way the imaging transfer of patterns can be analyzed in respect to the spatial frequencies they contain. The Fourier transform is defined as

$$\text{Eq. 4.2-17: } F(f(x, y))(u, v) := \int_{-\infty}^{\infty} \int_{-\infty}^{\infty} f(x, y) e^{-2\pi i(u x + v y)} dx dy$$

with Cartesian coordinates x and y and spatial frequencies u and v .

The calculation of convolution integrals with an impulse response function (cf. Eq. 4.2-6) is turned into a simple multiplication with its Fourier transform. The Fourier transform of the impulse response function of a system is called its "characteristic function" $T(u)$,

$$\text{Eq. 4.2-18: } T(u) = F(irf(r)).$$

This function can be normalized by its zero value to find the “Optical Transfer Function” *OTF* of the system:

$$\text{Eq. 4.2-19: } OTF = \frac{T(u)}{T(0)}$$

In order to characterize the transformation of spatially periodic signals their input and output modulation are compared. In one dimension – or one direction – the periodic input signal can be represented by a sinusoidal function $h(x)$:

$$\text{Eq. 4.2-20: } h(x) = a + b e^{i2\pi u x},$$

with a zero offset a , an amplitude b and a spatial frequency value u . If the imaging process is linear the output then turns out as

$$\text{Eq. 4.2-21: } d(x) = S(h(x)) = aT(0) + bT(u) e^{i2\pi u x}.$$

The input modulation M_{in} and the output modulation M_{out} are defined as

$$\text{Eq. 4.2-22: } M_{in} := \frac{|h_{\max} - h_{\min}|}{|h_{\max} + h_{\min}|} \quad \text{and} \quad M_{out} := \frac{|d_{\max} - d_{\min}|}{|d_{\max} + d_{\min}|}.$$

In general the *OTF* can be used to describe the transfer of any Fourier transform of an optical signal through an imaging system. It describes the transfer of modulation and phase components. The ratio describing just how the amplitudes of periodic variations are transferred into the image is called the “Modulation Transfer Function” *MTF*:

$$\text{Eq. 4.2-23: } MTF := \frac{M_{out}}{M_{in}}.$$

Radiographic imaging does not capture phase information and the output modulation can be calculated from the input modulation by the multiplication with the *OTF*

$$\text{Eq. 4.2-24: } M_{out} = M_{in} \cdot OTF.$$

For these two reasons *OTF* and *MTF* are represented by the same function.

In order to extend the idea of the Rose model to compare noise present in an image to its share introduced by quantum fluctuations one needs to introduce spatial frequency resolution in the noise distribution of image quanta.

The Fourier transform of the autocovariance function (cf. Eq. 4.2-8) of an image d is the “Wiener Spectrum” or “Noise Power Spectrum” NPS (Wiener-Khintchin theorem [17, 22]):

$$\text{Eq. 4.2-25: } NPS_d(u, v) := F(K_d(r')).$$

It gives information about the spatial frequency dependence of pixel to pixel fluctuations in a digital image. In images created by a pure Poisson process the Wiener spectrum would be independent of the spatial frequencies. In radiography factors like heel effect (cf. section 6.2), aliasing (cf. section 4.2.1), and the quality of algorithms like the flat-field correction influence the NPS [24].

A number of Poisson-distributed quanta is corresponding to every SNR connected by the assumption of ideal imaging of a Poisson process. The number corresponding to the SNR produced by an imaging system is called its “Noise Equivalent Quanta” NEQ [17]. It is calculated as:

$$\text{Eq. 4.2-26: } NEQ(q, u) = \frac{|q \cdot T(u)|^2}{NPS_d(u)} = \frac{q^2 \left(\frac{\partial d}{\partial q} \right)^2 MTF^2(u)}{NPS_d(u)}$$

where q stands for the number of quanta used for imaging. The value is set into relation with the number of quanta used in order to make the image. The result is the “Detective Quantum Efficiency” DQE which is connected to measurable values in several ways:

$$\text{Eq. 4.2-27: } DQE(\bar{q}, u) := \frac{NEQ(q, u)}{q} = \frac{q \left| \frac{\partial q}{\partial d} \right|^2 MTF^2(u)}{NPS_d(u)}$$

and in linear systems

$$\text{Eq. 4.2-28: } DQE(\bar{q}, u) = \frac{q \bar{G}^2 MTF^2(u)}{NPS_d(u)} = \frac{d^2 MTF^2(u)}{q NPS_d(u)}.$$

In the special case that photon noise is the only source of input noise and the input quanta are not correlated the DQE equals the spatial frequency dependent ratio of the squares of the output and the input signal to noise ratio [20].

The DQE of a perfect imaging system with quantum imaging being the only source of noise variations in the image would equal one (cf. Eq. 4.2-27). In digital radiography it is reduced by various parameters (cf. section 4.2.3.2).

4.2.3.2 Detective Quantum Efficiency in Digital Imaging

The detective quantum efficiency is taken to be one of the most important physical measures of imaging performance and can be used e.g. for optimization by changing beam quality. In diagnostic radiology it is reduced below a value of one by all variations introduced into the imaging process in addition to the Poisson noise (cf. section 5.2.1.4). One has to keep in mind that some of these variations are disturbing the requirements for the application of linear systems theory and pure Poisson statistics. In spite of that the approach gives deep insight into the imaging process and leads to reliable means of quality evaluation.

In quality assurance and measurement of radiography units the DQE is usually determined separately in the two directions of a two-dimensional image. Equalities from the definition (Eq. 4.2-27) give different possibilities. In order to get a maximum comparability between the results of different institutions for digital systems the procedure was standardized by the International Electrical Commission [25]. A detailed description of the measurement setup and calculation procedure is given. It relies on a sophisticated step function measurement of the MTF. The input SNR is fixed by the definition of five radiation qualities.

In digital imaging computational means offer various possibilities to influence figures like contrast and noise properties. For example filtering of high spatial frequencies can be used in order to decrease image noise directly. In digital imaging the regular pixel structure of the imaging system inherently imposes a filter at the Nyquist frequency. The application of a band pass filter is perfectly adequate if the interesting range of frequencies is known. In spite of that filters effectively cutting of image content at higher spatial frequencies act equally on noise and possibly present information content. The DQE is put to zero for these frequencies.

In general quantities like DQE or localized NEQ evaluate the transfer of the image information through the imaging chain. They show how signals of different spatial frequency are lost or preserved. It is not possible to improve their values by image processing.

The idea to analyze imaging techniques based on information content is taken up by this work. Especially the theoretic derivations about image resolution and noise properties (cf. chapter 5.2) are related to the techniques developed in connection with DQE estimation.

4.3 Dosimetric Measurement Categories and Units

In order to assess the radiation that is connected to a radiographic examination it is important to define dose quantities. The physical approach to x-ray application at humans especially in medical radiology is well established. An introduction into dosimetric measures of exposure in medical radiography is found more detailed in available reviews and legal rules [26-30]. Most relevant is the report about patient dosimetry for x-rays used in medical imaging [28] published by the International Commission on Radiation Units and Measurements (ICRU) in 2005.

Here after the description of the relevant mechanisms of the general mechanisms of interaction between radiation and matter, the dosimetric quantities connecting absorption and measures of risk are introduced. The last section describes ways to determine the spectral composition of X-radiation.

4.3.1 Interaction of Photon Radiation and Matter

Photons interact with matter in different ways. Elastic scattering processes are “Thomson Scattering” and “Rayleigh Scattering”. Thomson scattering as elastic interaction of a photon and an electron is the low-energy boundary case of Compton scattering (see below). Rayleigh scattering as elastic interaction of a photon and a whole atom contributes only a few percent or less of the narrow beam attenuation coefficient [31]. The process is negligible for radiographic imaging especially for imaging of a large area contrast. Also processes converting photons into electron-positron pairs (“Pair Production”) are neglected as these do not occur at energies below 1022 keV. The interaction processes relevant for medical radiography are the “Photoelectric Effect” and the “Compton Effect”. The linear attenuation coefficient due to the Photoelectric effect τ is equal to the probability of a photo interaction per unit distance of propagation in matter. It is proportional to the fourth power of the atomic number Z and to the inverse of the third power of the photon energy:

$$\text{Eq. 4.3-1: } \tau \propto \frac{Z^4}{E_p^3}.$$

Secondary particles of the Photoelectric effect are released electrons with kinetic energies up to the energy of the incident photons and photons with energies up to the K-radiation energy of the interacting matter (cf. section 4.3.2).

The Compton linear attenuation coefficient σ is defined analogously. It is proportional to Z and falls with the square root of E_p :

Eq. 4.3-2:
$$\sigma \propto \frac{Z}{\sqrt{E_p}}$$

The Photoelectric effect is dominant at high atomic numbers and at lower energies while the Compton effect is dominant for lower Z and higher photon energy (Figure 4.3-1).

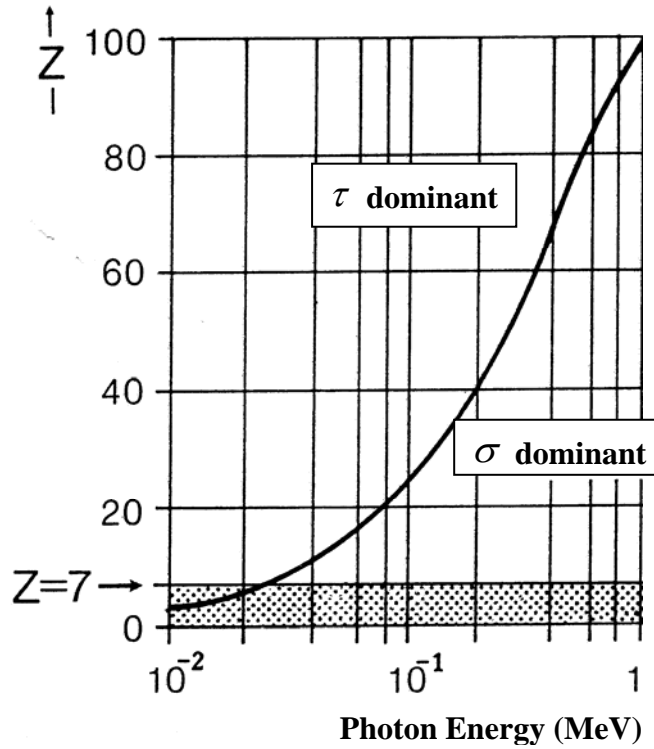


Figure 4.3-1: Dominance of Photoelectric Effect (τ) or Compton Effect (σ) for photons of different energy penetrating matter of different atomic number (Z). The line indicates equal probability for both processes (adapted from [32]).

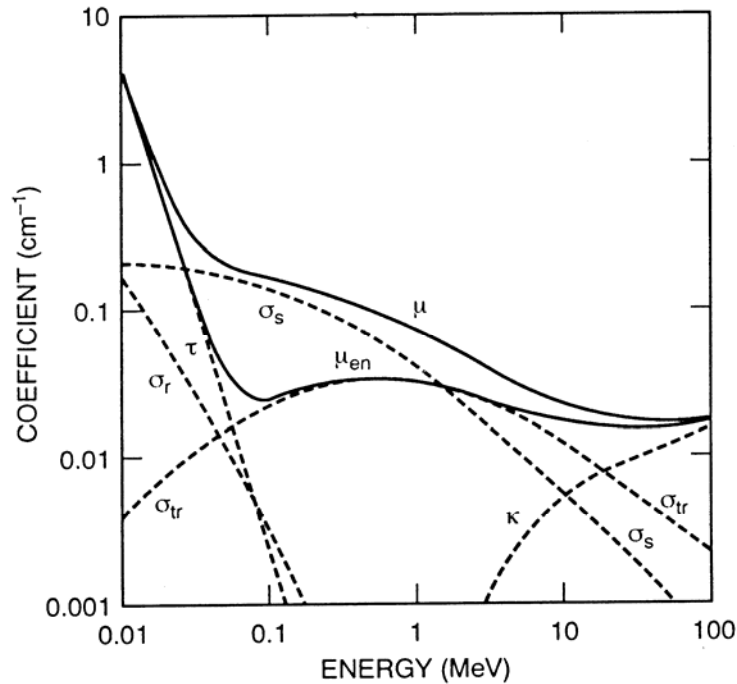


Figure 4.3-2: Linear attenuation coefficient μ , energy-absorption coefficient μ_{en} and the contributions from Photoelectric effect τ , Compton scattering σ_s , Compton energy transfer σ_{tr} and pair-production κ as functions of energy for photons in water [27].

As photons are electrically neutral they do not continuously lose energy when propagating through a material. The interaction between photon radiation and matter can (as above) be described by its probability per distance traveled. This quantity is called the “macroscopic cross section” or the “linear attenuation coefficient” μ . It can be split up into the contributions from different interaction processes ($\mu = \tau + \sigma + \dots$). The sum of all components leading to energy absorption is the “energy-absorption coefficient” μ_{en} . The attenuation coefficients can be visualized as material dependent functions of the photon energy (Figure 4.3-2).

The assumption of a constant probability of interaction per unit length for monoenergetic photons in homogeneous material directly leads to their exponential attenuation and the inverse exponential relation between the probability of transmission without interaction p through a layer of thickness x :

$$\text{Eq. 4.3-3: } p = e^{-(\mu \cdot x)}$$

For radiography the Photo effect is the main process of absorption producing image contrast while the Compton effect is the main source of angular scattering [27] degrading the contrast.

The distribution of secondary particles resulting from Photoelectric effect and Compton effect is depending on energy and direction of the input photons. In the range of radiographic energies most photoelectrons are directed more than 45° away from the direction of the incident photon (Figure 4.3-3). This is in contrast to the mainly forward-directed distribution given for higher energies.

Electrons and photons released by Compton interaction are also redirected further from the direction of the incident photon and also distributed over a wider range than for higher incident photon energies (Figure 4.3-4 and Figure 4.3-5). The exact spatial distribution of Compton scattering products can be calculated by quantum-mechanical theory [27].

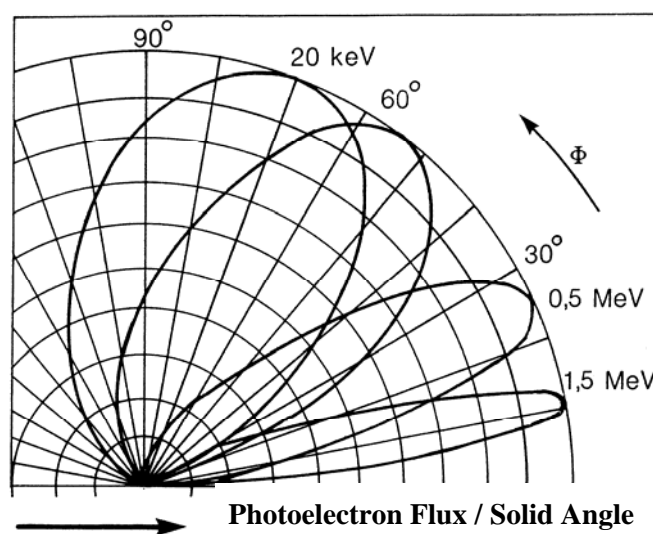


Figure 4.3-3: Angular distribution of photoelectrons in dependence of the incident photon's energy; the arrow indicates the forward direction [32].

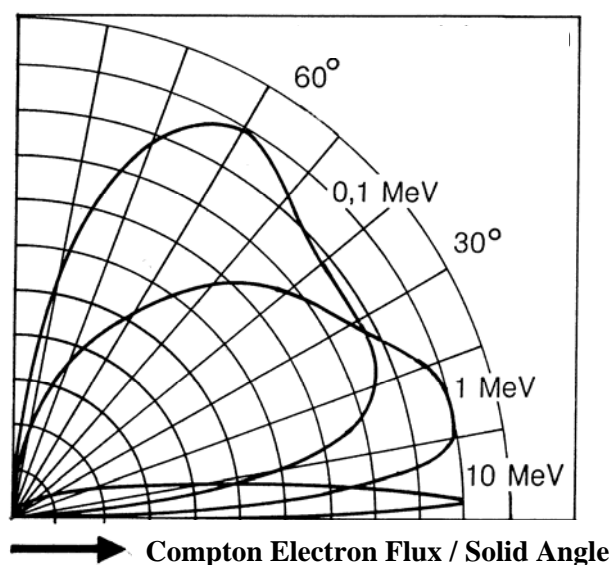


Figure 4.3-4: Angular distribution of Electrons released in Compton interactions in dependence of the incident photon's energy; the arrow indicates the forward direction [32].

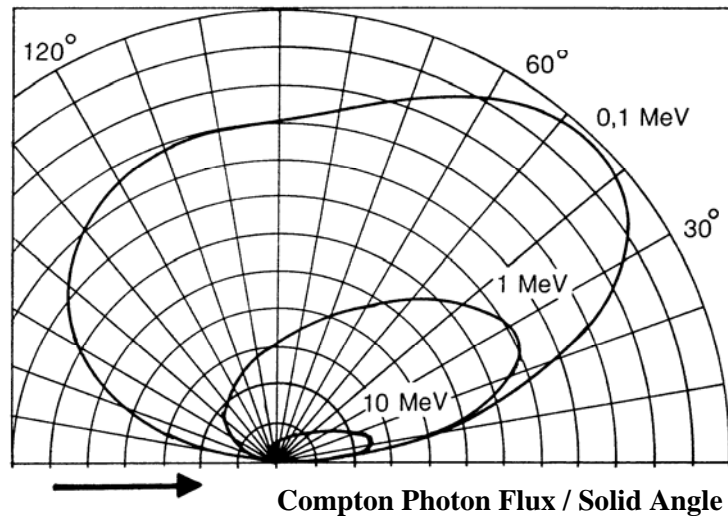


Figure 4.3-5: Angular distribution of Photons after Compton scattering in dependence of the incident photon's energy; the arrow indicates the forward direction [32].

In pediatric radiography the energy of electrons released is always below 100 keV (cf. e.g. [13]). Their depth of penetration in lung tissue is below 0.5 mm, the average fraction of their energy radiated as bremsstrahlung (“radiation yield”) is below 0.1% [27]. Photons emitted from fluorescence after photoelectric interaction in organic material can be assumed have energies up to the K-edge energy of Calcium (4.0 keV [33]). For this energy about 3 mm of lung tissue (ICRP) represent ten half-value layers [33].

In pediatric radiography the ranges and the angular distributions of secondary particles do not result in a build-up effect as strong as known from radiation therapy. Especially for considerations of large area contrast imaging, the influences of the distribution of secondary particles can be neglected. This is confirmed by the agreement of the experimental results (cf. section 6.3) and the results of the Monte Carlo calculations (cf. section 5.1.5) with the results of the analytical model based on exponential attenuation (cf. section 5.2.2).

The understanding of transmission, scattering and absorption, as well as the knowledge about the angular distribution of secondary particles is fundamental for the theoretical examination of radiographic imaging processes. It is completely included in the photon transport calculations in this work (cf. chapter 5.1) and necessary to understand the definitions of quantities of exposure (cf. section 4.3.2).

The model developed in order to directly quantify the properties of radiographic imaging (cf. chapter 5.2) relies in the first approach on a concept of linear attenuation (Eq. 4.3-3): x-ray photons are assumed not to reach the detector after any interaction (“narrow-beam geometry”). On the other hand scattering radiation is an important factor in radiographic imaging. It can be

included by introducing an energy dependent and depth dependent quantity relating the intensity in a homogeneous radiation field to the intensity calculated for a narrow beam, the “buildup factor” [27]. In the model introduced later in this work the buildup factor had to be splitted into two components in order to keep the inclusion of a scattering fraction consistent with the statistical approach used (cf. section 5.2.1.4).

4.3.2 Dosimetric Quantities

In this chapter physical measures quantifying the exposure connected with the medical application of radiation are introduced. Quantities describing the impact of ionizing radiation to a target are based on the absorption of energy connected with the interaction (cf. section 4.3.1).

As fundamental quantity the “absorbed dose” is defined as the quotient of the mean energy \overline{dE} imparted to a volume by the total mass dm of that matter [28]:

$$\text{Eq. 4.3-4:} \quad D = \frac{\overline{dE}}{dm}$$

Its unit is J/kg with the special name “Gray” (Gy).

A quantity used for uncharged ionizing radiation is the “kerma”. It is defined as the infinitesimal ratio between the sum of the initial kinetic energies of all the charged particles released in a volume of matter and the mass of that volume. Absorbed dose and kerma are numerically equal when expressed in the same material in the case of charged-particle equilibrium and in absence of bremsstrahlung losses [28]. These requirements are not always met, e.g. close to interfaces between matters of different atomic numbers [34-36].

In most cases it is not possible to perform direct measurements of a radiation field in a human being. The measurement of patient exposure or the exposure of individual organs in medical radiology therefore has to be performed indirectly by measurements of the applied external radiation field. The air kerma measured free-in-air on the central axis of the radiation field at a specified distance from the focal spot is the most common quantity specifying the output of x-ray systems used in medical imaging [28]. Free-in-air means in a mass volume of air without radiation scattered back from the patient into the measurement region. The values are combined with calculated proportionality factors relating them to organ doses (cf. section 5.1.5.1). These so-called “dose conversion coefficients” are defined as the ratio of the absorbed dose in an organ to the air kerma measured free-in-air at the patient location. The

quantity defined as the kerma in a plane perpendicular to the central beam right in front of the patient location is called the “entrance dose”.

Organ or tissue doses D_T are the energies absorbed by organs or tissues (T) divided by their masses; this is equal to the absorbed dose averaged in the organ or tissue. In general also a radiation weighting factor w_R for the relative radiation risk for a particular kind of radiation (R) has to be taken into account to derive the “equivalent doses” H_{TR} from these values.

$$\text{Eq. 4.3-5: } H_{TR} = w_R D_T.$$

The factor w_R is set to unity for x-ray quanta [37]. The unit of H_{TR} still is J/kg, the special name for the quantity weighted for risk assessment is “Sievert” (Sv).

Additional organ specific weighting factors w_T take into account the organ’s different sensitivities to lethal or other severe radiation health effects. These tissue weighting factors w_T add up to one. The recommended values [37] are listed below (Table 4.3-1). Here the “remainder tissues” are adrenals, extra thoracic region, gall bladder, heart, kidneys, lymphatic nodes, muscle, oral mucosa, pancreas, prostate, uterus and cervix, small intestine, spleen and thymus.

Tissue	w_T
Bone-marrow, Colon, Lung, Stomach, Breast, Remainder Tissues	0.12
Gonads	0.08
Bladder, Oesophagus, Liver, Thyroid	0.04
Bone surface, Brain, Salivary glands, Skin	0.01

Table 4.3-1: Tissue weighting factors.

To derive a single valued, risk related quantity for health effects the organ doses D_T are multiplied with these tissue weighting factors w_T and summed up over all organs and tissues T of the human body considered to be sensitive to the induction of stochastic effects. The result is the “effective dose” E [37]:

$$\text{Eq. 4.3-6: } E = \sum_T w_T H_T$$

This value relates any exposure to a risk-related comparable exposure of the whole body. The effective dose is the dosimetric quantity recommended for operational, practical radiological protection in many circumstances. The nominal risk coefficients do not apply to the sub population of pediatric patients [37]. For the estimation of the likely consequences of exposures in pediatric radiology, it is preferable to use the absorbed dose of the different organs.

Dose quantities for radiation safety of persons exposed occupationally are monitored mainly using personal dosimeters. Here another quantity is needed in addition: the skin dose $H_p(0.07)$ is the dose equivalent in 0.07 mm depth in the body at the application point of the personal dosimeter and the depth dose $H_p(10)$ is the dose equivalent at a body depth of 10 mm at the point of application of the personal dosimeter. $H_p(0.07)$ and $H_p(10)$ monitors are used to monitor personal exposure at work. In contrast patient dosimetry relies on monitoring the exposure parameters and geometry exactly and allows precise calculations and simulations.

4.3.3 Beam Quality

The beam quality describes the spectral composition of x-ray radiation. In general the energy spectrum of medical x-radiation is influenced by the parameters of its generation like the tube voltage, the anode material and the anode angle, the filtering material and thicknesses [38]. The spectra used in pediatric radiology are according to the European guidelines on quality criteria for diagnostic radiographic images in paediatrics [13] standard tube spectra with added filtration of about 1 mm aluminum and a minimum of 0.1 mm copper. The spectra used for photon transport simulations were calculated adding aluminum filtration equivalent to the inherent filtration of a standard x-ray system (cf. section 5.1.1 and Figure 5.1-1).

For measurements of the beam quality the spectral composition is reduced to measurements of connected properties like “effective energy” or “half value thicknesses” of beam absorbance. These do not give the whole field information but are by far easier to be measured. Based on this measurements and adjustments that are possible on every common x-ray tube one can get beam qualities from different sources equal to a reasonable degree [39]. This is especially crucial for the evaluation of the quality of x-ray imaging devices [25].

In this work we either refer directly to the detailed spectral composition of the radiation applied [38] or calculate results for monoenergetic radiation which can be combined to give estimates for different incident photon spectra.

4.4 Risk Estimation

Radiographic imaging is one of the most common methods of modern medical diagnostics. This applies also to pediatric and neonatal medicine. The application of x-rays in order to produce images is extremely widespread because it is leading to valuable diagnostic information. Compared to many other diagnostic procedures attendant risks (e.g. risk of infection of the wound) are heavily reduced. Nevertheless patients of x-ray examinations are taking a risk of suffering a late health effect detriment.

Biological effects from radiation have been observed and examined for more than 100 years [40]. Deterministic effects of high dose irradiations are well described. They are utilized to combat cancer in radiation therapy as well as for sterilization. Exposure of the whole body to a high dose of penetrating radiation causes the “acute radiation syndrome”, an acute illness resulting from damage of vitally important organ systems like the bone marrow, the gastro intestinal system, the cardio vascular system or the nervous system. The radiation doses used in medical radiography are about three orders of magnitude below the dose range where macroscopic deterministic effects become observable.

The long term so-called stochastic effects of the introduction of cancer and hereditary disease are subject to radiobiological and epidemiological studies. Both cases are summed up by the United Nations Scientific Committee on the Effects of Atomic Radiation (UNSCEAR) in a series of reports [41-43]. The epidemiological approach suffers from the need for large and high quality cohorts that is connected with the goal of quantification of the effect of low dose exposure despite a relatively large background, the long time of detriment expression and the difficult exclusion of confounding factors. Nevertheless children are expected to be most sensitive to late effects of radiation exposure due to their dynamic growth process. Additionally the life span in that detrimental mutations can take effect is the longer the younger the patients are. The risks connected with radiation exposure are expected to be a two or threefold higher for children than for the average population [43-45] (Figure 4.4-1).

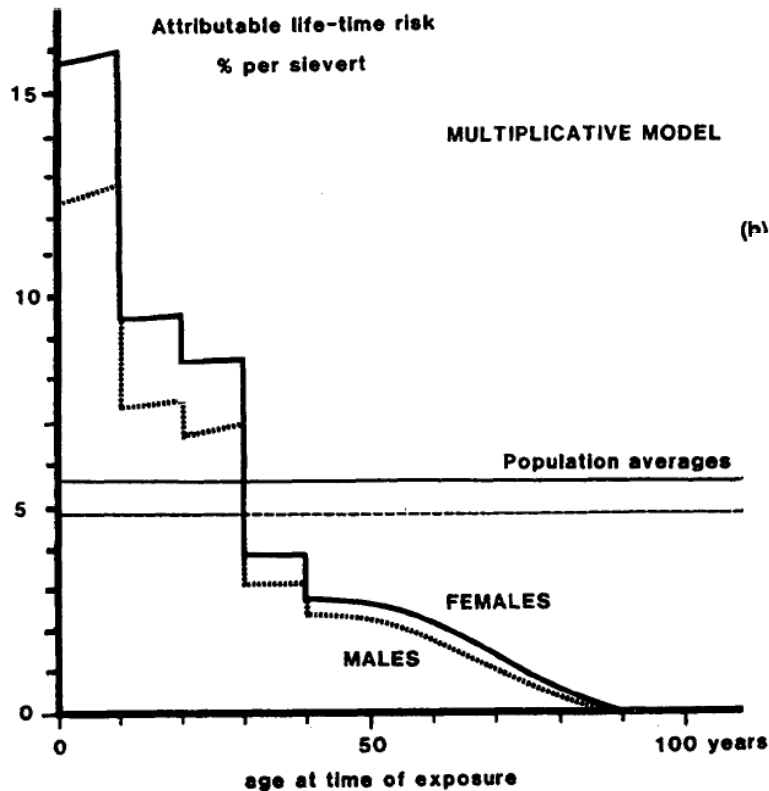


Figure 4.4-1: The attributable lifetime risk from a single small dose at various ages at the time of exposure, (multiplicative model, assuming a DDREF of 2). The higher risk for the youngest age group will not be expressed until late in life (adapted from [45]).

Regarding medical x-ray exposures, practical risk estimation often uses a working-hypothesis in which the risk is taken to increase linearly with increasing radiation dose the so-called linear no threshold (LNT) model. This LNT hypothesis is challenged by different scientific studies stating an overestimation or underestimation of radiation induced detriment or the disregard of a positive net effect of low dose irradiation the so-called hormesis. Wall et al. [46] give a review about this discussion as well as about general difficulties in risk estimation.

In practical application the LNT model leads to a simple concept of minimization and justification: there is a (low) risk assumed to be attributable to the low-dose exposure in connection with medical x-ray application which has to be outweighed by the diagnostic benefit of the procedure. This assumption was used in this work.

4.5 Monte Carlo Radiation Transport Calculations

Monte Carlo calculation of radiation transport and energy deposition is common in the field of determination of dosimetric quantities connected with medical application of electromagnetic radiation or beams of accelerated particles [47, 48]. Here the general method as well as the code system used in this work are introduced.

4.5.1 History and Introduction

Monte Carlo methods were investigated systematically in the calculation of radiation transport e.g. in building a nuclear weapon in the Manhattan Project [49-51]. The underlying principle of random sampling was used at least some hundred years earlier in simpler questions e.g. Buffon's needle problem in the eighteenth century [48] which delivers an estimate of the value of the number pi from throwing a needle onto a pattern of parallel stripes. The fundamentally new approach of Monte Carlo simulation was to use random numbers in order to sample a set of variables in accordance with predefined probability distributions [48, 52]. The approach was designed for computed evaluation by the first electronic computers and its success is closely connected to computer development.

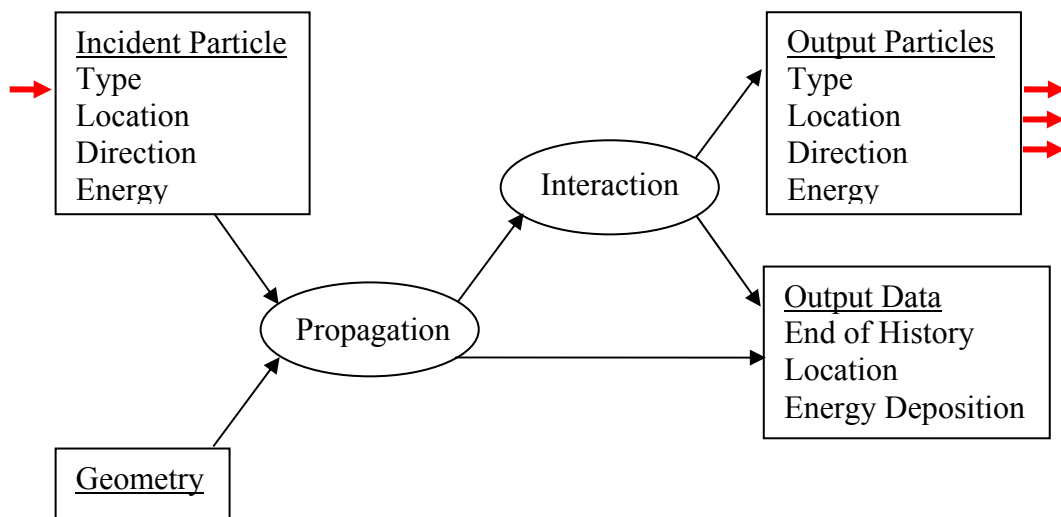


Figure 4.5-1: Principle of Monte Carlo calculation of photon histories

In the Monte Carlo calculations of radiation transport sequences (“histories”) of interaction processes and intermediate propagation are determined for every radiation particle. Variables of location, direction and energy are repeatedly calculated or sampled. At the beginning a primary photon is generated according to the probability distributions of direction and energy

chosen for the radiation source. The propagation distance without interaction is sampled from the corresponding probability distribution that results from the properties of the particle, the geometry of the setup and the interaction processes included. The properties of a subsequent interaction are sampled from the connected probability distributions e.g. the angular distribution or energy of the secondary particles. The history is ended if a particle leaves the geometry or has deposited all its energy. Propagation and interaction processes are repeated for every particle (Figure 4.5-1) until all histories are ended and then the next primary photon is generated.

The energy transfer connected to the processes can be recorded. The overall distribution of the energy deposited in the virtual material setup can be recorded as an output of the simulation.

Mathematically the input probability density functions $p(r)$ defined in a range $[a;b]$ for a variable r are transferred into a normalized, cumulative form $P(r)$.

$$\text{Eq. 4.5-1: } P(r) = \frac{\int_a^r p(\tilde{r}) d\tilde{r}}{\int_a^b p(\tilde{r}) d\tilde{r}}$$

The sampling from $P(r)$ can then be performed by random numbers of the range $[0;1[$. For computational evaluation the integrals are often discretized into sums.

The accuracy of the results depends directly on the number of particles reaching into a region of interest. It can be improved by a larger number of primary input particles. Modern Monte Carlo computer codes offer further methods of variance reduction. One example called “splitting” performs the calculation of a late part of a particle track repeatedly while suitably reducing the weight of the results. The complementary method of “Russian Roulette” is used to gain computation speed by discarding particles with further histories of low importance (cf. section 4.5.2).

The quality of the results is dependent on the quality of the random number generator and of the cross section dataset used. For example periodicity of random numbers used for a certain input value imposes an upper boundary on the number of input photons that can be simulated. High quality random number generation is therefore of high practical interest for the calculation.

A universal way of determination of radiation transport is the solution of the Boltzmann equation which accurately describes any kind of particle transport far from equilibrium. However an analytical solution is not always possible e.g. in complex geometries. In general geometries Monte Carlo simulations offer the most accurate way to calculate radiation

transport and dose distributions [50, 51]. Different modern codes ([9, 53-56]) are in use in different fields like material physics, nuclear physics and radiation physics. They are applicable to medical topics e.g. radiation therapy for a wide range of radiation energies and different sources and geometries [47, 48, 57]. In the beginning of calculations of exposure to different organs connected with different setups of irradiation, mathematical models of patients were used. The different organs were represented by the combination of regular geometrical objects. These virtual phantoms were subsequently replaced by models generated from tomographic data of real humans [2, 58-60] which are called voxel phantoms due to their composition from volume elements (voxels). Today's models reach an individual accuracy for the estimation of specific organ doses that leads to the possibility to examine the influence of individual variations between different patients, e.g. size and weight of separate organs [7].

4.5.2 EGS Code System

All Monte Carlo calculations of radiation transport and energy deposition connected to this project were performed using EGS (Electron-Gamma-Shower) in the version EGSnrc [9]. EGSnrc evolved from previous versions (EGS3, EGS4, EGS4/PRESTA) developed since the late seventies of the last century [61].

EGSnrc has been compared to other simulation systems [62-64] and various dosimetric applications. Publications related to EGSnrc are listed at the EGSnrc homepage [65]. Kawrakow and Rogers give a fully self contained description and user manual of EGSnrc [9].

EGS is a software code system made for analogue Monte Carlo simulation of the coupled transport of photons and electrons. In this context analogue states the abstraction and use of probability densities as functions derived from the properties of the physical transport. For example distances between collisions are sampled from exponential distributions. Detailed interactions between the passing particle and each nuclide along its path are averaged this way. The step lengths used are also randomly coupled to mean free path and material borders to gain higher accuracy.

EGSnrc is set up modularly. The user is intended to interact with the code system through diverse subroutines. HATCH and SHOWER, both subroutines of the main code, are used to establish media data and to initiate a cascade. HOWFAR and HOWNEAR are to specify the geometry of the virtual setup and in AUSGAB the user specifies how to score and output the results and controls means of variance reduction. Common blocks give the opportunity to change values of variables. The user can define or re-define features in the collection of macro definitions.

The code system is capable of simulating radiation transport of electrons and photons in any element compound or mixture in an energetic range from 1 keV to 10 GeV. The package has a flexible user interface written in the FORTRAN based macro programming language MORTRAN. The splitting of the code into diverse subroutines and block data and the use of MORTRAN reduces the risk that user edits introduce bugs into the code. EGSnrc allows for the flexible use of Bremsstrahlung splitting and Russian Roulette (cf. section 4.5.1):

If the Bremsstrahlung splitting option is set, the result of a bremsstrahlung event is split into several photons, each having the fraction of the inverse of their number of the weight of the incoming electron and an electron with an energy given by its initial energy minus the energy of the last bremsstrahlung photon produced. This violates energy conservation on an event-by-event basis but energy is conserved on average.

If the option Russian Roulette is enabled e.g. for a secondary photon the routine will randomly pick a number between zero and one when it is produced and compare it to a predefined level. If the number picked is greater than this level the photon is discarded. In the other case that the number picked is smaller than the predefined level the weight of the photon is increased by the inverse of this level and the calculation proceeds.

Physics processes that are taken into account are Bremsstrahlung production, positron annihilation during slowing-down and at rest, inclusively the follow-up of the annihilation quanta, multiple coulomb scattering from nuclei using a multiple scattering theory which overcomes shortcomings of Molière theory, Møller scattering, Bhabha scattering, pair production, Rayleigh scattering, fluorescence, Auger and Coster-Kronig electrons, and - most important for the simulation of X-Ray radiography - Photoelectric effect and Compton scattering [9]. In our approach photons and electrons are followed down to kinetic energies of 1 keV and then deposited locally.

Between discrete hard collision interactions the continuous slowing down approximation is applied to the simulation of charged particle tracks.

The data for the material used is prepared by the stand-alone data preprocessing code PEGS4. This part of the distribution also creates piecewise-linear fits of branching ratios and cross section data from cross section tables for elements of atomic number 1 to 100. The cross sections used for the different interactions are published [9], e.g. the cross sections used for the bremsstrahlung process are modeled according to the NIST bremsstrahlung cross section data base [66, 67] which is the basis for the radiative stopping powers recommended by the ICRU [68].

5 Calculations

In order to optimize radiographic imaging it is useful to examine the imaging process theoretically in a first approach. Calculations can give insight into the radiographic imaging process without use of clinical imaging systems and manpower. The knowledge gained is valuable for the planning and preparation of experiments as well as for the evaluation of experimental results.

There are different ways based on theoretical knowledge to gain results about. In this work Monte Carlo radiation transport calculations (cf. chapter 5.1) were employed as a well established and reliable method to give information about the exposure of different organs connected with various radiographic examinations of the chest of an infant. For these calculations a voxelphantom of a newborn was constructed from the existing dataset of a baby (cf. section 5.1.2). Subsequently the system was extended by an imaging setup. Imaging of a step structure was adapted to the imaging calculation of the antropomorphic phantom in order to get results comparable to a experimental setup.

In a second theoretical approach (cf. chapter 5.2) the imaging process was traced back to a binomial sampling experiment fulfilling a clearly defined imaging task. A conceivable model was developed reducing the complexity of radiographic imaging in order to examine quantitatively the relations between the information content of an image and the exposure at that it was taken.

The calculation results were evaluated in comparison to eachother as well as in comparison to experimental data (cf. chapter 6).

5.1 Monte Carlo Radiation Transport Calculations

In the following the simulated systems are described and the calculation results and their errors are given. The simulations performed here deliver dosimetric conversion coefficients as well as information about the transmission behavior of a paediatric patient and a physical phantom.

5.1.1 Monte Carlo Calculation of the Imaging Process

The Monte Carlo Code system offers a variety of input options and diverse imaging setups can be modeled. In the following the irradiation types and geometry used are specified. For the radiation quality input we discriminate two possibilities.

One approach is to simulate exposure to monoenergetic radiation. This is useful in examinations of dependences of a result from the energy. Results are obtained at certain energies and can be compared directly.

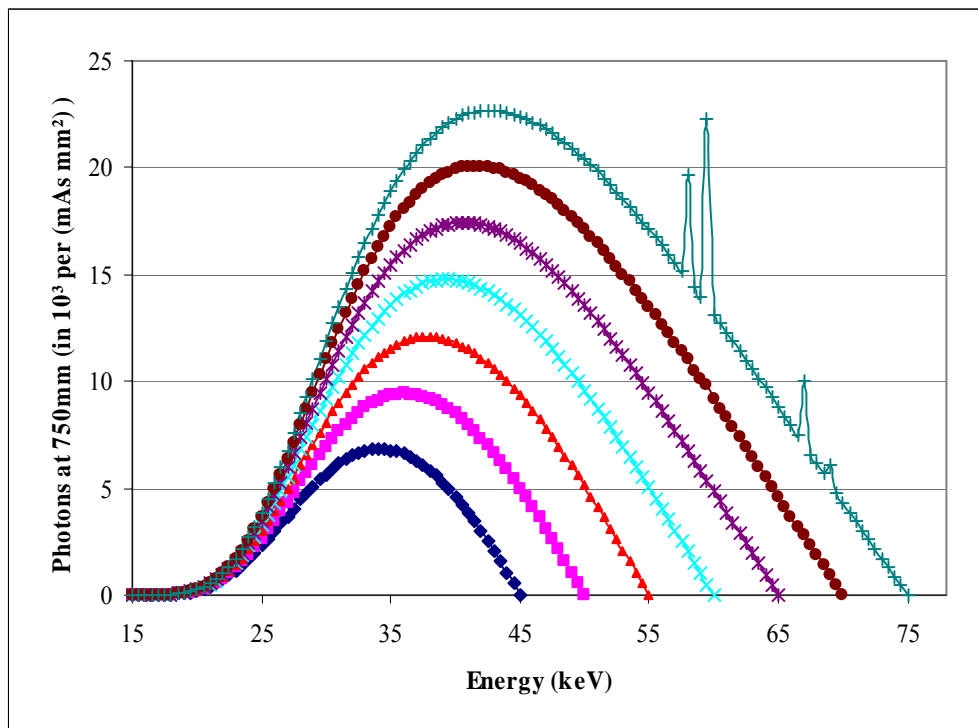


Figure 5.1-1: Spectra of an x-ray tube with wolfram cathode and filtered by 3 mm aluminum and 0.1 mm copper, peak voltage from 45 kV to 75 kV.

In order to get quantitative findings for scenarios of poly-energetic exposure like exposure with standard x-ray tube spectra the monoenergetic results are to be weighted and combined in connection with their occurrence in the spectrum.

Alternatively realistic spectral datasets were used mainly for the calculation of organ exposures. The spectral composition of differently produced and filtered radiation was obtained from listed data [69]. As an example Figure 5.1-1 shows a series of x-ray spectra.

The source geometry was chosen to be defined by an isotropic point source located at 1 m from the surface of the virtual phantom. Imaging was implemented into this virtual system as a quadratic flat photon counting screen with 100 % detection probability for all energies (Figure 5.1-2).

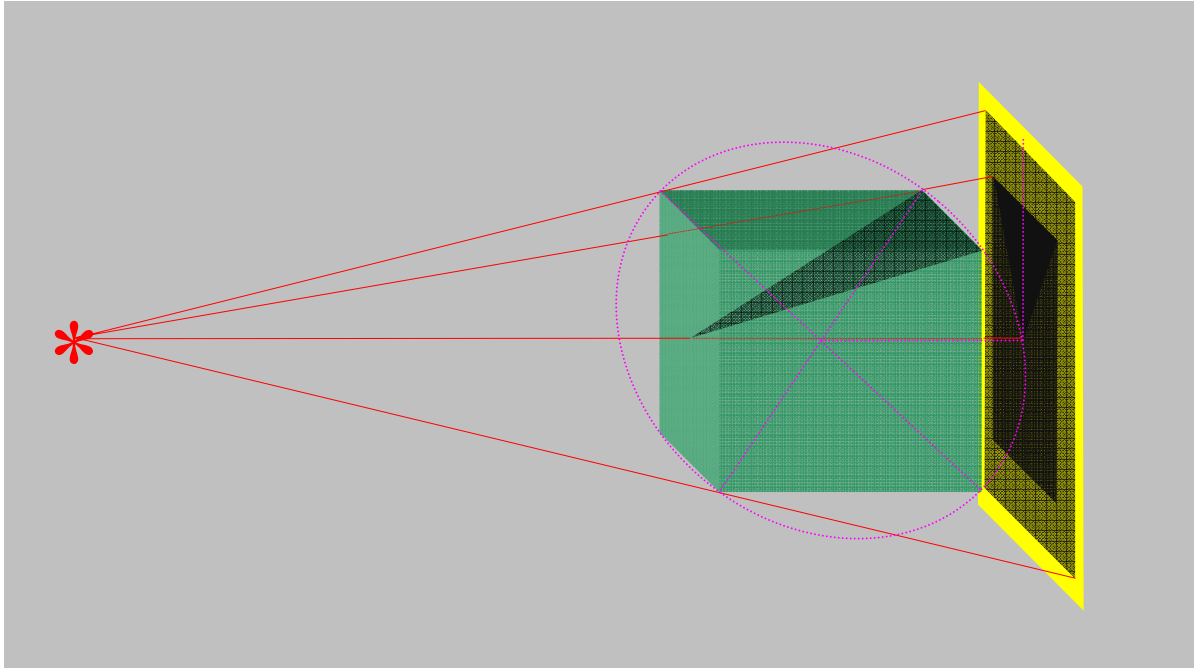


Figure 5.1-2: Imaging simulation.

Seen from the radiation source the screen is placed on the opposite side of the virtual phantom. The phantom is complemented to a full cuboid by empty volume elements (voxels) without effect on the radiation interaction properties. In a distance of half the diagonal of that box around the phantom from its center, the line from the source hits the screen normally at its midpoint. One axis of the screen is set parallel to one of the edges of the phantom box. The second axis is rectangular to the first one. The screen edge length was chosen 10 % longer than the length of the phantom box diagonal. The location and size of the screen are chosen in a way ensuring that the screen does not intersect the phantom region and is large enough to cover the whole image region (cf. pink lines in Figure 5.1-2). The screen was divided into 500 x 500 areas of equal size, the “pixels”. The quantities describing the image process are defined accordingly as follows:

The “pixel value” t_e is defined as the overall count of photons incident on one of the pixels. The “image” \hat{d}_e is the 500 x 500 matrix of pixel values, an “image region” d_e is a sub-matrix of \hat{d}_e . The “transmission” \tilde{p}_e of a material composition in front of a pixel is the quotient of the pixel value t_e and the average number of quanta \tilde{n}_e started into the solid angle of an image pixel:

$$\text{Eq. 5.1-1:} \quad \tilde{p}_e = \frac{t_e}{\tilde{n}_e}$$

The “image contrast” c_e between two image regions d_e and d'_e of different homogeneous absorbers is defined as the difference between the average pixel values of the respective image regions:

$$\text{Eq. 5.1-2:} \quad c_e = \langle d_e \rangle - \langle d'_e \rangle$$

The “noise of an image region” $n_e(d_e)$ is defined as the standard deviation of the pixel values of d_e (cf. section 4.2.1):

$$\text{Eq. 5.1-3:} \quad n_e(d_e) = \sqrt{\langle (d_e - \langle d_e \rangle)^2 \rangle}$$

The “contrast to noise ratio” CNR_e for two regions d_e and d'_e is defined as the quotient of the image contrast c_e and the arithmetic mean of the noises $n_e(d_e)$ and $n_e(d'_e)$:

$$\text{Eq. 5.1-4:} \quad CNR_e = \frac{2 \cdot c_e}{n_e(d_e) + n_e(d'_e)}$$

The definition of CNR_e follows the model of the definition of ΔSNR_{Rose} (cf. chapter 4.2.2).

The “signal to noise ratio” SNR_e for a region d_e is defined as the quotient of the mean pixel value of that region $\langle d_e \rangle$ and the corresponding noise $n_e(d_e)$:

$$\text{Eq. 5.1-5:} \quad SNR_e = \frac{\langle d_e \rangle}{n_e(d_e)}$$

The detector screen is assumed to count impacts of photons that passed through the phantom region regardless of their energy and angle of incidence. In order to include energetic properties into the examinations monoenergetic exposures are simulated. Energy changes are attributed only to interacting photons and secondary photons. Imaging large area contrasts both are assumed to contribute to a homogeneous noise background. Under this approximation results derived for the monoenergetic exposure can be weighted by detector response properties and combined in order to imitate realistic tube spectra.

The analysis of the images was performed by the powerful imaging software program IDL [70]. The code made it possible to acquire, visualize and manipulate the simulated and measured image datasets as well as to calculate their characteristic properties and store those in files conveniently formatted e.g. for subsequent spreadsheet evaluation.

5.1.2 Tomographic Phantom

Two virtual phantoms were used to represent the specimen under radiographic examination and the imaging setup used. The first one was derived from clinical tomographic data. It was used in this work to determine conversion coefficients as well as in the imaging simulation.

5.1.2.1 Virtual Representation

In order to model an exposition scenario of a pediatric patient by Monte Carlo techniques a virtual representation of the patient is needed. These virtual phantoms should describe the three-dimensional distribution of different materials in the patient as well as the spatial segmentation of different organs.

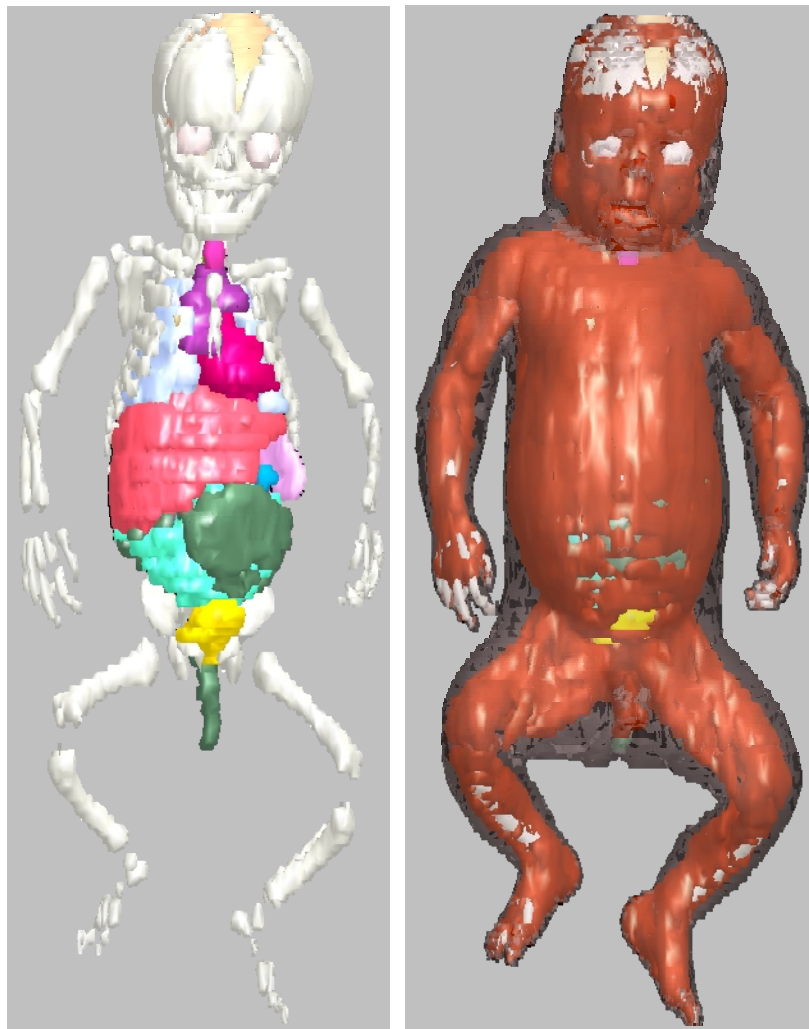


Figure 5.1-3 Anterior views of the virtual phantom:

Skeleton and main organs (left), additional muscle tissue and skin (left).

The phantom used here has been reconstructed and segmented from tomographic data of an eight week old baby corpse taken 24 hours after death by Zankl et al. [2]. The dataset was segmented into 90 regions representing either whole organs or parts of those. Partly those regions were combined into 23 organ groups.

A second layer of the process of segmentation is the attribution of material properties to each volume element (voxel) of the virtual phantom. The compositions of the different tissues of an infant were taken from different publications of ICRP and ICRU [71-73]. The tissues were grouped into seven types of bone and three types of soft tissue. Additionally the compositions of lung, muscle, adipose tissue and skin were directly adopted from those publications. The exact compositions used here are found in the next section (5.1.2.2).

The original edge lengths of the volume elements were 0.85 mm x 0.85 mm in each slice and each slice was 4 mm high. The baby weighed 4.2 kg and was 57 cm in length, 21.8 cm in width of the body, and 12.2 cm from front to back. In order to calculate results in this work with higher validity for a newborn or premature infant, the dataset was rescaled to half the original values in all three dimensions (0.425 mm x 0,425 mm x 2 mm). The resulting weight of the body is then 525 g. Figure 5.1-3 shows the composition of the voxel phantom in two types of volume rendered images.

The composition of the phantom out of the voxel-elements is smoothed but still visible. In comparison to the MIRD type phantoms [74, 75] which the voxel phantoms are meant to replace the higher accuracy in representing a human being is obvious (see also [59]). The model is a reliable basis for calculating quantities that are dependent on the relative distances between organs, on their sizes and on their compositions. These are in our case conversion coefficients for organ doses as well as transmission properties of the thorax region.

On the other hand it is clear that calculated results are hard to compare to experimental setups. The phantom following this computer phantom cannot be built in any way and it is not designed for physical measurements of image properties like contrasts and noise. A second phantom had to be designed for those purposes. This phantom is described in the next chapter (cf. chapter 5.1.3).

5.1.2.2 Voxelphantom Materials

Here we provide material compositions used for the virtual representation of the baby. The elemental composition of tissues and bones of infants are found from ICRP Publication 89 [73]. The elemental composition (in % by mass) is found in the following table (Table 5.1-1)

	H 1	C 6	N 7	O 8	Na 11	Mg 12	P 15	S 16	Cl 17	K 19	Ca 20	Fe 26	I 53
Active marrow (RBM)	10.5	41.4	3.4	43.9	0.1	0.2	0.2	0.2				0.1	
Bone mineral (cortical bone)	4.2	16	4.5	50.2		0.3	8	0.3			16.5		
Cartilage	9.6	9.9	2.2	74.4	0.5		2.2	0.9	0.3				
Adrenals	10.6	16.3	2	71				0.1					
Oesophagus													
Gallbladder													
Thymus													
Ovaries													
Testes													
Uterus													
Stomach	10.6	11.5	2.2	75.1	0.1		0.1	0.1	0.2	0.1			0
Liver	10.3	12.6	2.7	73.3	0.1		0.3	0.2	0.2	0.3			0
Spleen	10.5	8.6	2.4	77.6	0.2		0.2	0.1	0.2	0.2			0
Thyroid	10.4	11.9	2.4	74.5	0.2		0.1	0.1	0.2	0.1			0.1
Urinary bladder	10.5	9.6	2.6	76.1	0.2		0.2	0.2	0.3	0.3			0
Brain	10.8	5.5	1.1	81.6	0.2		0.3	0.1	0.2	0.2			
Heart	10.6	7.5	1.8	79.3	0.2		0.1	0.1	0.2	0.2			
Kidneys	10.7	6.4	1.6	80.4	0.2		0.2	0.1	0.2	0.2			

Table 5.1-1: Elemental compositions of tissues for the newborn (in % by mass).

Bones are composed of red bone marrow, cortical bone and cartilage. The composition of the different bones of the phantom was deduced from the masses of bone the constituents [72, 73], the specific gravities of bone constituents [72, 73, 76] and the volumes of single bones and the

whole skeleton in the Voxel-model [77]. The mass ratios between the different components are found in Table 5.1-2.

	RBM	Cortical bone	Cartilage
Sternum	0.0%	56.7%	43.3%
Ulnae, radii (lower arm bones)	10.0%	51.0%	39.0%
Ribs	11.3%	50.3%	38.4%
Skull (cranium)	10.9%	50.5%	38.6%
Thoracic spine	11.8%	50.0%	38.2%
Lumbar spine (+ sacrum)	9.3%	51.4%	39.3%
Humeri (upper arm bones)	14.5%	48.4%	37.0%
Clavicles	13.2%	49.2%	37.6%
Mandible (facial skeleton)	13.1%	49.2%	37.7%
Femora (upper leg bones)	14.5%	48.5%	37.1%
Scapulae	13.8%	48.9%	37.4%
Hand bones	21.9%	44.3%	33.8%
Tibiae, ... (lower leg bones)	19.1%	45.9%	35.1%
Pelvis (os coxae)	26.2%	41.8%	32.0%
Cervical spine	30.3%	39.5%	30.2%
Foot bones	59.6%	22.9%	17.5%

Table 5.1-2: Compositions of bones for the newborn (mass fraction).

For the Monte Carlo Simulation the different materials are collected into groups of similar elemental composition in order to lower the complexity of the segmentation process to a reasonable level. The result are material compositions for seven “bone mixtures” (Table 5.1-3) resulting from groups of bones of similar composition (cf. Table 5.1-2) and those for skin, muscle, adipose tissue, lung tissue and for three groups of other soft tissue (Table 5.1-4). The assignments between the groups and the original tissue are clear from comparison to the original composition (cf. groupings in Table 5.1-2).

	Element											Density
	H	C	N	O	Na	Mg	P	S	Cl	Ca	Fe	
	(% by mass)											(g/cm ³)
Bone mixture 1 0 % RBM 57 % cortical bone 43 % cartilage	6.5	13.4	3.5	60.6	0.2	0.2	5.5	0.6	0.1	9.4		1.356
Bone mixture 2 10 % RBM 51 % cortical bone 39 % cartilage	6.9	16.2	3.5	59.0	0.2	0.2	5.0	0.5	0.1	8.4		1.315
Bone mixture 3 15 % RBM 48 % cortical bone 37 % cartilage	7.1	17.6	3.5	58.2	0.2	0.2	4.7	0.5	0.1	7.9		1.297
Bone mixture 4 20 % RBM 45 % cortical bone 35 % cartilage	7.4	18.9	3.5	57.4	0.2	0.2	4.4	0.5	0.1	7.4		1.275
Bone mixture 5 25 % RBM 43 % cortical bone 33 % cartilage	7.6	20.5	3.5	57.1	0.2	0.2	4.2	0.5	0.1	7.1		1.256
Bone mixture 6 30 % RBM 40 % cortical bone 30 % cartilage	7.7	21.8	3.5	55.6	0.2	0.2	3.9	0.5	0.1	6.6		1.238
Bone mixture 7 60 % RBM 23 % cortical bone 17 % cartilage	8.9	30.2	3.4	50.5	0.1	0.2	2.3	0.3	0.1	3.8	0.1	1.141

Table 5.1-3: Groups of elemental compositions for bones of the newborn for Monte Carlo Simulation.

	Element										Density
	H	C	N	O	Na	P	S	Cl	K	I	
	(% by mass)										(g/cm ³)
Skin	10.4	10.4	2.8	75.5	0.2	0.1	0.2	0.3	0.1		1.100
Soft tissue 1 (adrenals, oesophagus, gallbladder, ...)	10.6	16.3	2.0	71.0			0.1				1.070
Soft tissue 2 (average of stomach, liver, spleen, thyroid, urinary bladder)	10.5	10.8	2.5	75.3	0.2	0.2	0.1	0.2	0.2	0	1.050
Soft tissue 3 (average of brain, heart, kidneys)	10.7	6.5	1.5	80.4	0.2	0.2	0.1	0.2	0.2		1.035
Muscle	10.4	10.3	2.4	76.2	0.1	0.1	0.1	0.2	0.2		1.050
Adipose tissue	11.1	29.7	0.9	58.0	0.1	0.1	0.1				0.950
Lung	10.6	7.6	1.8	79.2	0.2	0.2	0.1	0.2	0.1		0.260

Table 5.1-4: Groups of elemental compositions for soft tissues of the newborn for Monte Carlo Simulation. □

5.1.3 Step Phantom

In order to calculate the properties of imaging with results comparable to experimental images a simpler virtual physical phantom was created offering homogeneous areas with specific, known contrasts. It was designed to be easily built consisting of two crossed, step like structures one of aluminum and one of PMMA. These materials are commonly used to simulate bone (Al) and soft tissue (PMMA) like photon scattering behavior. The virtual generation in the simulation environment was made to be flexible in materials and step heights in order to generate a phantom in a range of transmission comparable to pediatric patients.

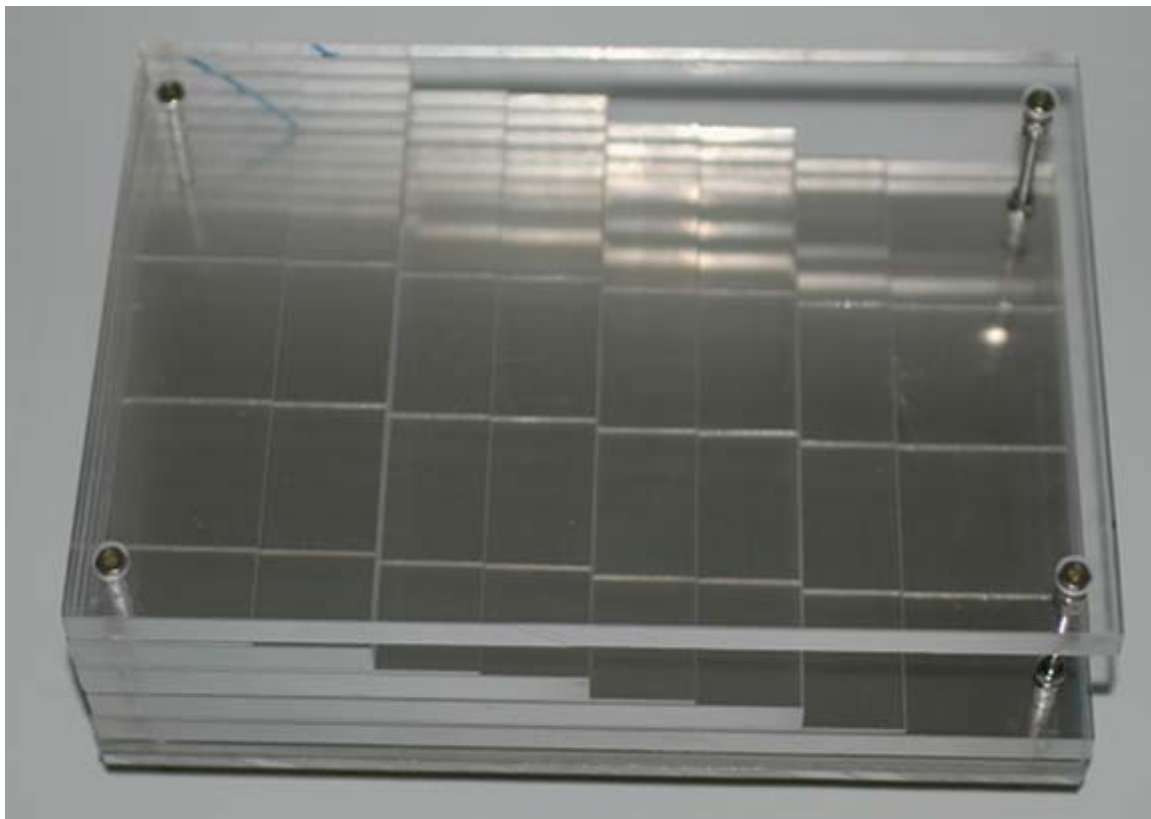


Figure 5.1-4: Step phantom of two crossed step like structures set up modularly of PMMA steps of 1 mm and 10 mm, and of aluminum steps of 1 mm and additional optional aluminum layers.

The phantom was actually built as a flexible setup of layers (cf. section 6.2). The used voxel-size was 1 mm x 1 mm x 0.5 mm. Figure 5.1-4 shows the real phantom represented by the virtual phantoms used in the simulations. The aluminum steps total thicknesses are selected from 1 mm or 5 mm base plates and three steps of 1 mm. The layers made from PMMA are selectable by two base plates and three steps each 10 mm thick. On each step an element of 1 mm or 1.5 mm PMMA can be added to provide a low contrast step in the resulting images.

5.1.4 Error Discussion for Monte Carlo Simulations

Differences in results of different Monte Carlo simulations for conversion coefficients (cf. section 5.1.5.1) are mainly due to differences between the individual voxel phantoms used. The variations result from the different size and distribution of organs [5]. These variations exceed the statistical uncertainties by far. The Monte Carlo simulations have been adapted to produce results of statistical variations below 1% in organ dose for all organs relevant in thoracic imaging.

The change from combinatorial-geometric, mathematical phantoms to CT-based voxel models (see 4.5.1) has been accompanied by examination of the differences resulting from that change [3]. Additionally the voxel models also allow for the calculation of variations due to the change of patient sizes [6, 7]. Results for organs thin in the direction of the incident beam can be dependent on the three-dimensional spatial resolution of the primary dataset. In this work the resolution in this direction (cf. section 5.1.2.1) is sufficiently high.

The results are also evaluated in order to estimate influences of different photon radiation qualities on the organ conversion coefficients. The examination of the connected relative changes is independent of their absolute value. The precision of the results should be smaller than the effects considered. The statistical variation of the results achieved below 1% is perfectly sufficient for this purpose.

The usual statistical variation of the Monte Carlo method leads to much higher variation when imaging is simulated. The randomized generation of x-ray quanta with respect to their spatial distribution leads to fluctuations in the pixel values (cf. section 5.1.1) even after penetration through homogeneous voxels. In order to evaluate the statistical properties of the imaging simulation the image of an absorber with 100% transmission (cf. section 5.1.1) is calculated and the transmission histogram determined (Figure 5.1-5). As expected for a Poisson process (cf. Eq. 4.2-14) the standard deviation of the pixel values of this image equals the square root of their average value.

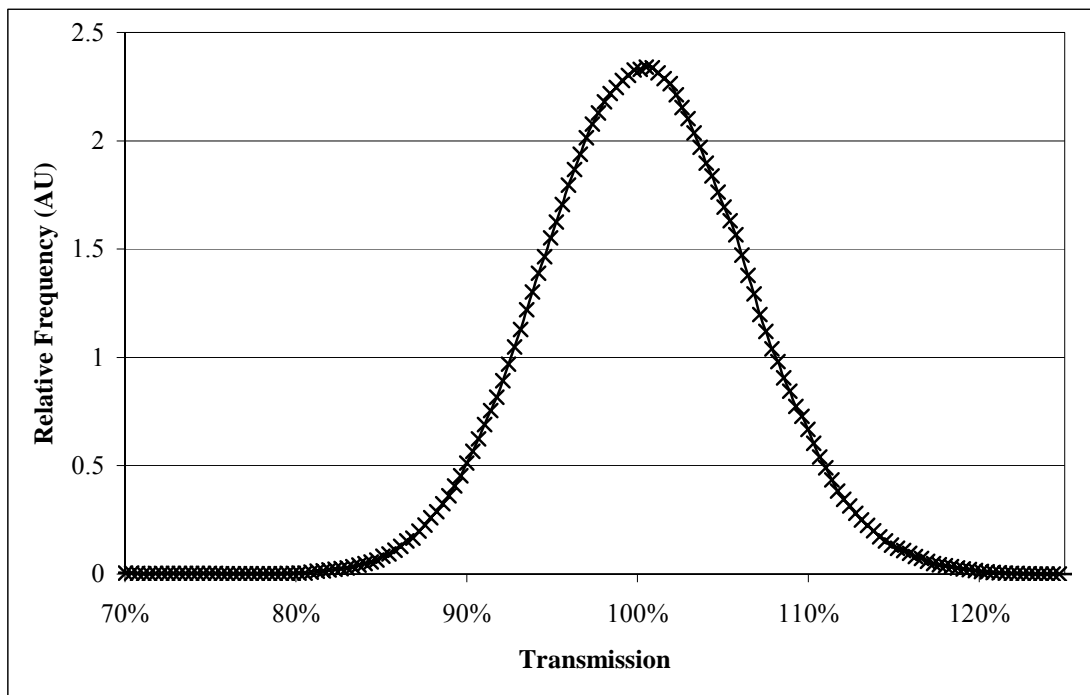


Figure 5.1-5: Transmission histogram of the pixel values of an “absorber” of 100% transmission. Here $4 \cdot 10^7$ quanta were incident to $1.4 \cdot 10^5$ pixels which results in an average of 290 incident quanta per image pixel and a standard deviation of the transmission of 6%.

The calculation of 10 million photon histories for one image of the thorax region of the voxel phantom with a resolution of 92x118 pixels took approximately 3.5 ± 1 hours on a standard PC (2.4Ghz, 512MB RAM) depending on the chosen energy (between 20 keV and 70 keV for monoenergetic calculations). This corresponds to an average calculation speed of about 800 histories per second. The average of about 940 incident quanta per pixel leads to the standard deviation of the transmission of a pixel imaging 100% transmission is about 3%.

This choice of the number of starting quanta (10^7) and of the imaging resolution was a compromise between random fluctuations and processing time.

5.1.5 Results of the Monte Carlo Calculations

The Monte Carlo calculations performed were used in order to quantify several characteristic properties of pediatric thorax examinations concerning the exposure of different organs and the transmission behavior of a newborn patient (cf. section 5.1.2) and relate them to connected properties of a physical phantom (cf. section 5.1.3). The imaging setup (cf. section 5.1.1) led to a resolution of the chest image of about 120 x 90 pixels and of 330 x 420 pixels for the physical phantom. The number of 10^7 starting quanta results in the average of 940 and 71.5

starting quanta per image pixel respectively. The field sizes at the phantom surface were adapted to the chest region of the newborn patient (65 mm x 50 mm; cf. Figure 5.1-11) and to the size of the physical phantom (200 mm x 160 mm; cf. Figure 5.1-16).

5.1.5.1 Conversion Coefficients for Thoracic Pediatric Radiography

When optimizing pediatric radiology, it is of interest to convert measurable parameters of x-ray exposures to equivalent doses received by the different organs of a patient. Monte Carlo calculations of radiation transport and energy deposition can serve to determine ratios between the exposure characterizing quantity “air kerma free in air” and equivalent doses for different organs under certain parameters of exposure. These conversion coefficients were calculated in this work for exposure of the thoracic region AP of the resized voxel phantom (see 5.1.1) to radiation from an x-ray tube at various peak voltages (see Figure 5.1-1). The region exposed was adjusted to the thorax region (see Figure 5.1-11). The results for the irradiation geometry specified in section 5.1.1 are given below (Figure 5.1-6 and Figure 5.1-7).

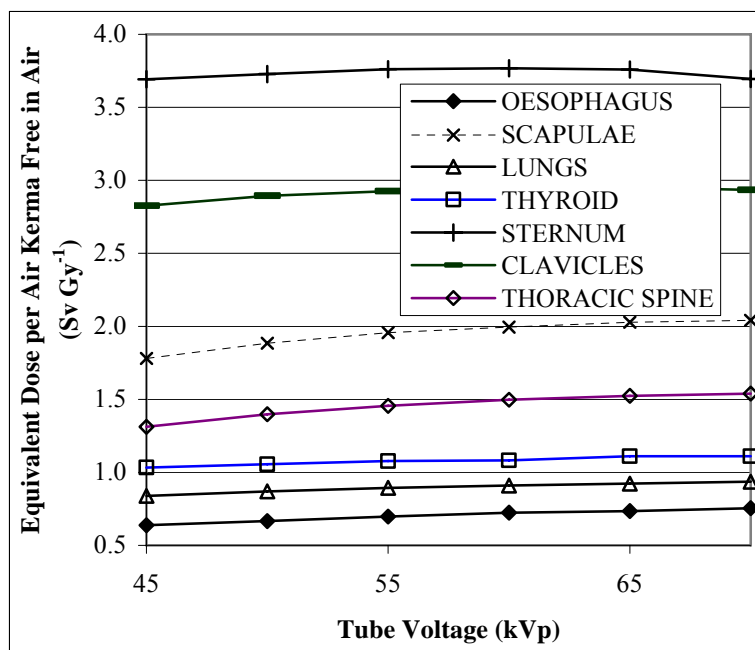


Figure 5.1-6: Conversion coefficients for equivalent organ dose per air kerma free in air for different organs exposed to primary radiation in thoracic radiography AP with spectra of various peak voltages (spectra as shown in Figure 5.1-1, irradiation geometry as specified in section 5.1.1).

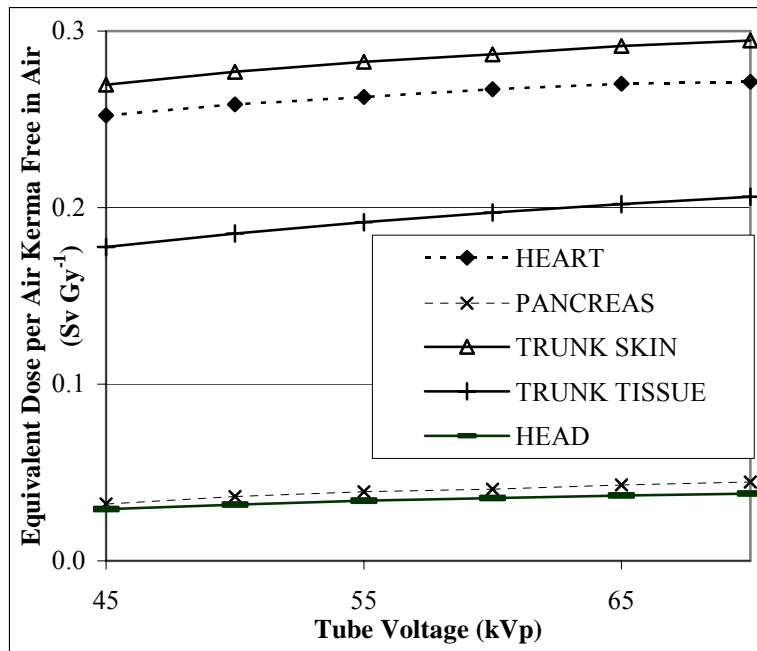


Figure 5.1-7: Change of conversion coefficients for equivalent dose per air kerma free in air for different organs not fully exposed to primary radiation in thoracic radiography AP with spectra of various peak voltages (spectra as shown in Figure 5.1-1, irradiation geometry as specified in section 5.1.1).

There are no strong variations in conversion coefficients for a tube voltage change in the diagnostically relevant range. The conversion coefficients for monoenergetic exposure are shown in Figure 5.1-9 and Figure 5.1-9. The highest coefficients are connected with bone structures at the entrance side of the radiation. There is a rise connected with the higher penetration depths to the location of an organ. Above the energy that is sufficient to “reach” an organ efficiently the coefficients decrease as more and more photons are transmitted without interaction. At very high energies the differences resulting from the different location in the body and material composition even out.

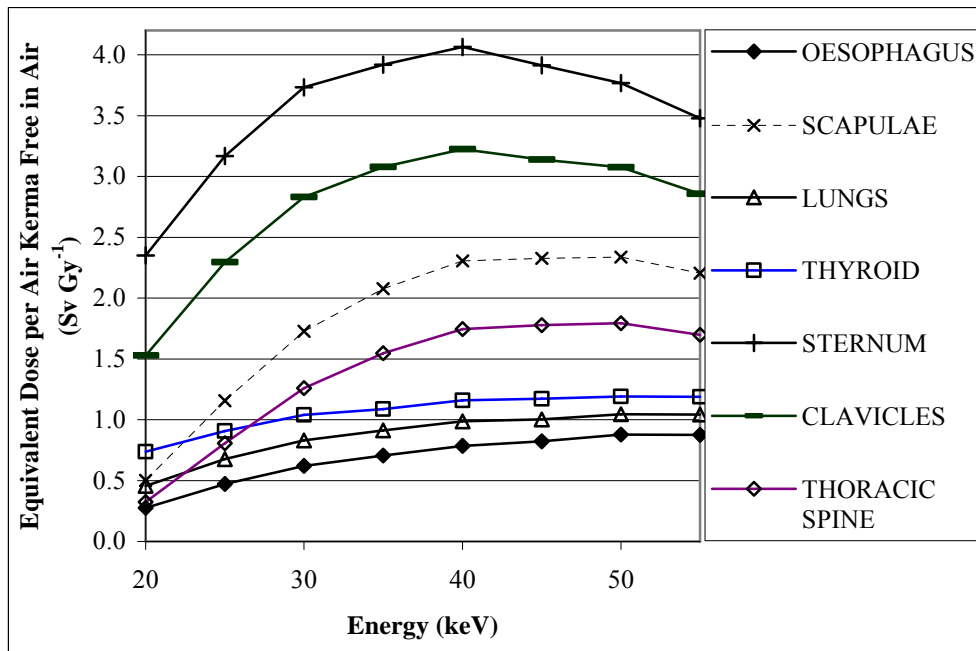


Figure 5.1-8: Conversion coefficients for equivalent organ dose per air kerma free in air for different organs exposed to primary radiation in thoracic radiography AP for monoenergetic photons (irradiation geometry as specified in section 5.1.1).

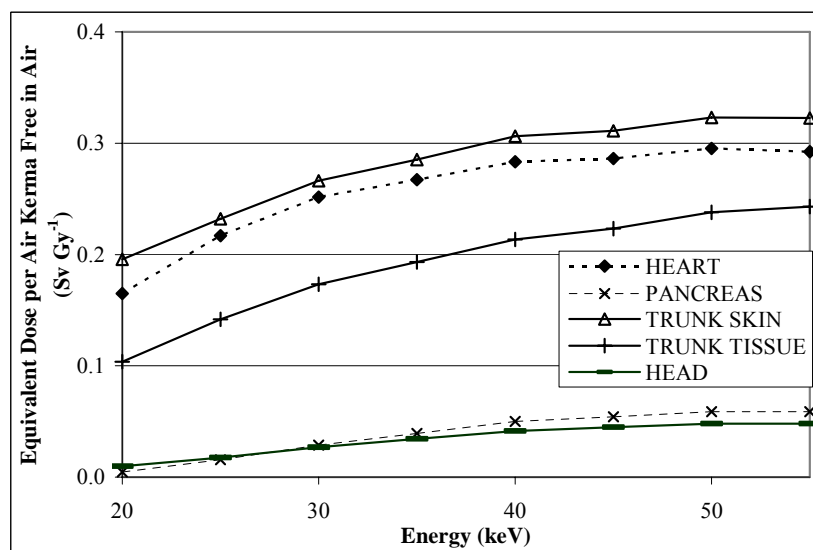


Figure 5.1-9: Conversion coefficients for equivalent organ dose per air kerma free in air for different organs not fully exposed to primary radiation in thoracic radiography AP for monoenergetic photons (irradiation geometry as specified in section 5.1.1).

5.1.5.2 Transmission Behavior of a Pediatric Patient

In order to study results about the transmission behavior of the thorax region of a neonate or premature infant (cf. section 5.1.2) monoenergetic photon imaging was simulated (cf. section

5.1.1). The images resulting from a simulation of 10^7 starting photons at different primary energies directly show the rise of the penetration strength and the degradation of the contrast with higher photon energies (Figure 5.1-10). Inversion of the presentation of the images shows the pictures darker where a film would be exposed higher like in conventional screen-film radiography (Figure 5.1-11).

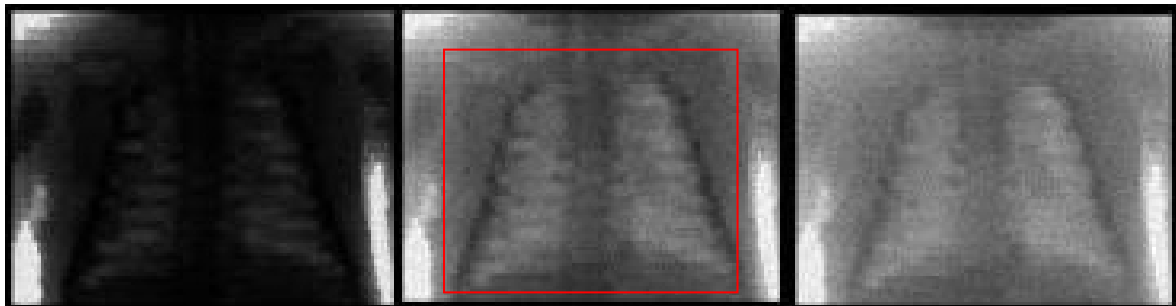


Figure 5.1-10: Imaging simulation of the transmission behavior of the thoracic region of the virtual baby phantom with 10^7 monoenergetic photons with 20 keV (left), 35 keV (middle), and 50 keV (right). The region of interest for the transmission examination is indicated by the red frame.

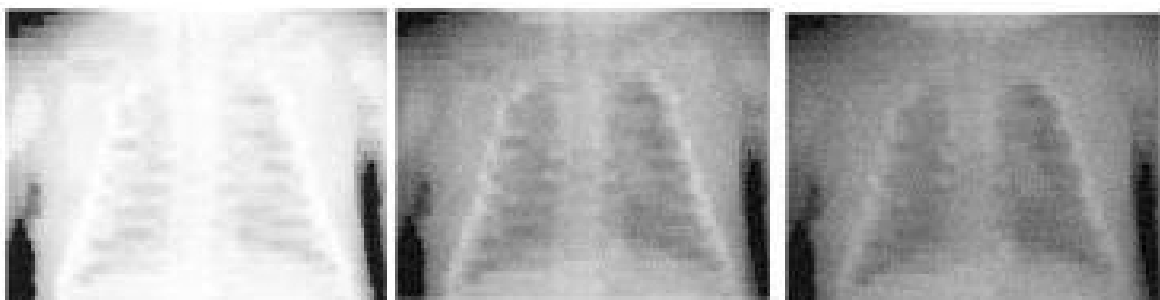


Figure 5.1-11: Inverted view of the same images shown in Figure 5.1-10 (dark = high photon count).

The average photon transmission $\langle \tilde{p}_e \rangle$ of the region of interest in thoracic radiography (95 x 75 pixels, 53 mm x 42 mm, red frame in Figure 5.1-10) rises from below 10 % to about 50 % with their primary energy rising from 20 keV to 55 keV (Figure 5.1-12).

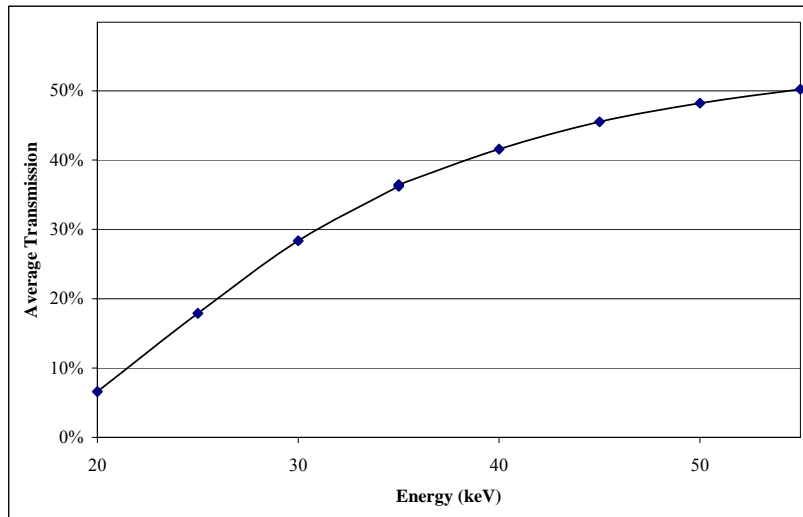


Figure 5.1-12: Transmission of the lung region of a pediatric patient as function of photon energy averaged over the region of interest (cf. Figure 5.1-10).

The rise in transmission led to a higher number of quanta reaching the screen and therefore of photons usable for screen-film imaging. Quantum noise was reduced thereby and the film got its designated exposure faster. In thoracic imaging these effects balanced the loss of contrast or resolution that could be accomplished with screen-film combinations optimized for lower energies which are necessary for high resolution of low contrasts e.g. in mammography.

Transmission histograms of the chest region make it possible to examine the contrast for different photon energies. A 100 % transmission value resulting from simulation without the phantom has a standard deviation of 3.3 % for 10^7 photons spread on 120×90 pixels in the image plane. Regarding this statistic noise the histograms are smoothed on this scale. To facilitate the comparison of all histograms they were normalized in such a way that their integral equals the overall transmission (Figure 5.1-13). The contrast between the different major thorax regions of similar transmission leads to a peaked structure (Figure 5.1-14). The height and width of these peaks can serve as a measure of contrast. The overall contrast between the brightest and the darkest region of each image shows up as the “overall width” of its histogram (Figure 5.1-15).

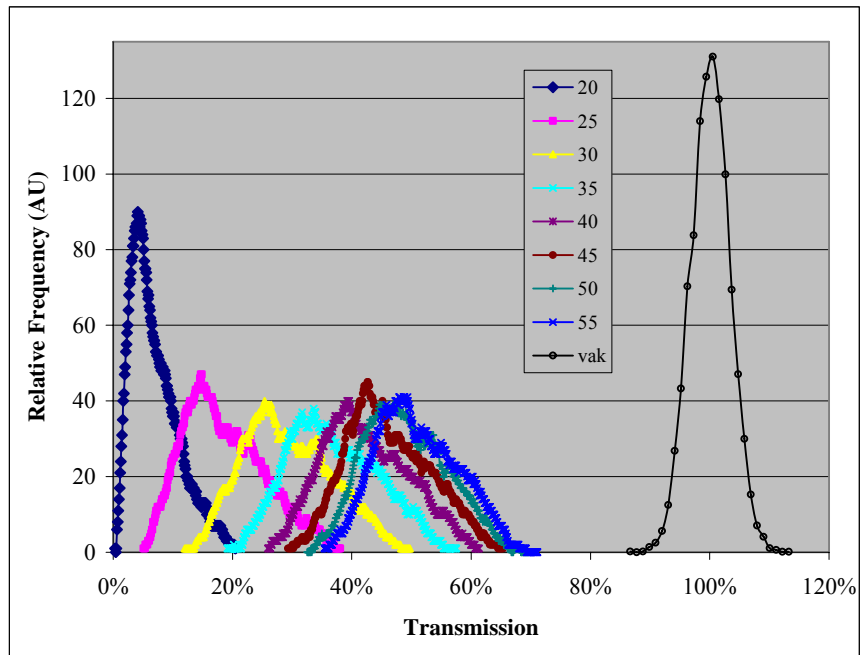


Figure 5.1-13: Transmission histograms of the lung region of the voxel phantom at different energies (keV) compared to the input distribution (linear scale).

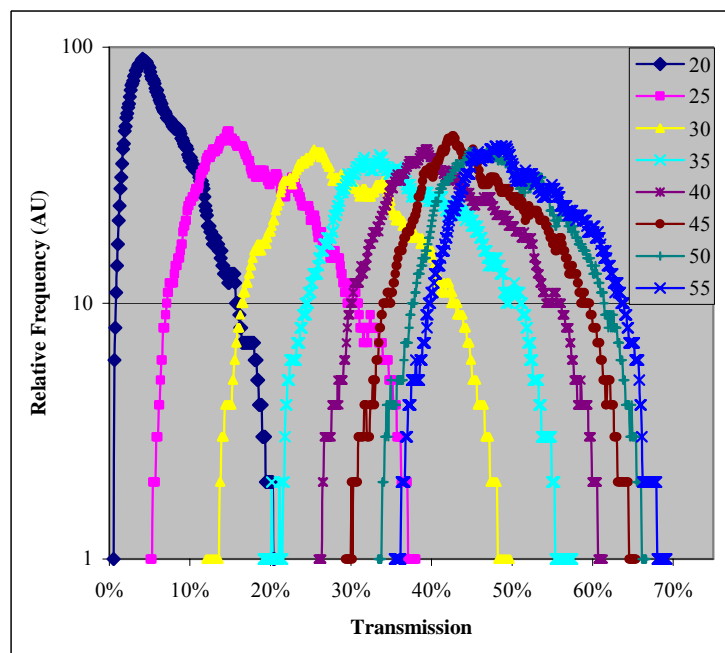


Figure 5.1-14: Transmission histograms of the lung region of the voxel phantom at different energies (keV).

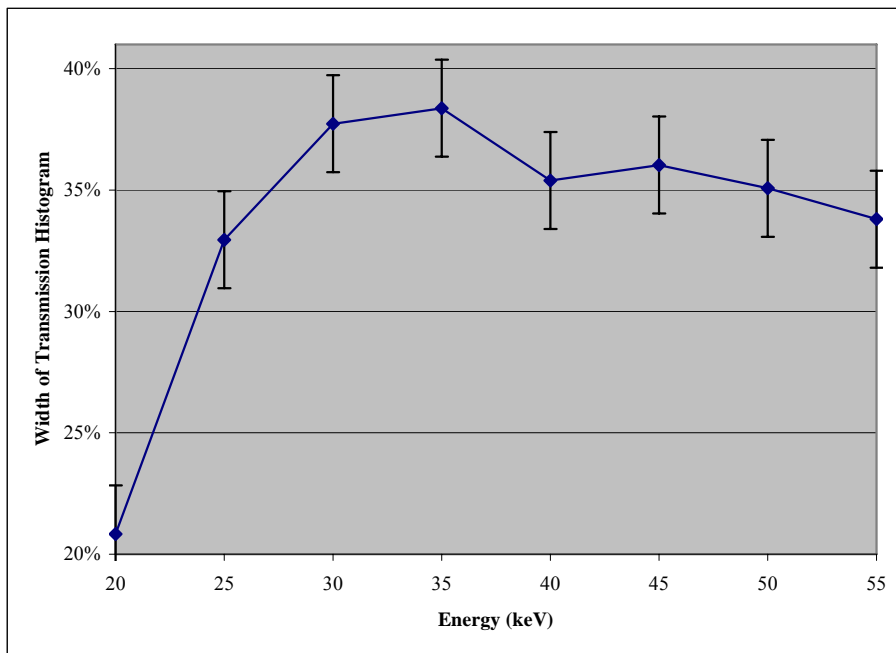


Figure 5.1-15: Overall width of the transmission histograms produced by a simulation of thoracic imaging of the baby voxel phantom vs. energy of incident photons.

The evaluation for the individual baby Voxel-model used here shows best discrimination between the peaks in the histogram connected to the regions like the lateral part of the ribs, the lung fields or the mediastinal region for the simulations of 25 keV and 30 keV photons (Figure 5.1-14, right). The best value for the overall contrast is found to be close to an energy in the region of 30 keV to 35 keV (Figure 5.1-15). Changes in the shape and width of the histogram are significant if the energy is lowered below this optimal range (cf. chapter 5.2.2.2).

The results of the transmission behavior of the pediatric voxelmodel can be compared to results of similar calculations on physically clearer structures (cf. section 5.1.5.3). The adaptation of the setups helps to connect phantom experiments and properties of pediatric imaging.

5.1.5.3 Transmission Behavior of a Step Phantom

The simulation of the imaging of two crossed, step like structures directly shows imaging properties like the change of transmission (cf. section 5.1.1) and contrast (cf. section 5.1.1) connected with different photon energies (Figure 5.1-16).

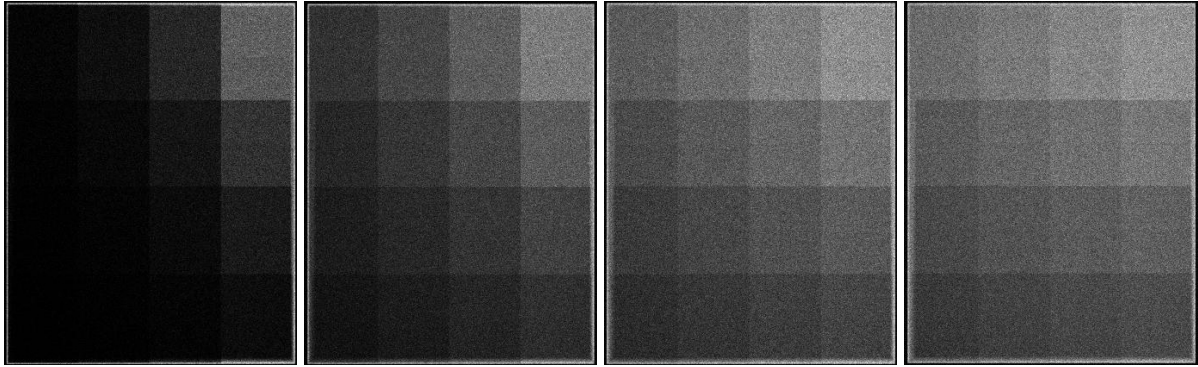


Figure 5.1-16: Monoenergetic imaging simulation of 10^7 incident photons at 20 keV, 30 keV, 40 keV and 50 keV (from left) to evaluate the transmission behavior of a phantom consisting of a aluminum step (3 mm, 2 mm, 1 mm, 0 mm; from the left in each image) crossed with a PMMA step (10 mm, 20 mm, 30 mm, 40 mm).

At low energies the contrast between the thinnest absorber steps is most significant while the contrast between thick steps is degraded due to very the low transmission through them. With higher energies the transmission rises (Figure 5.1-17) and the contrast especially between the thinner steps decreases.

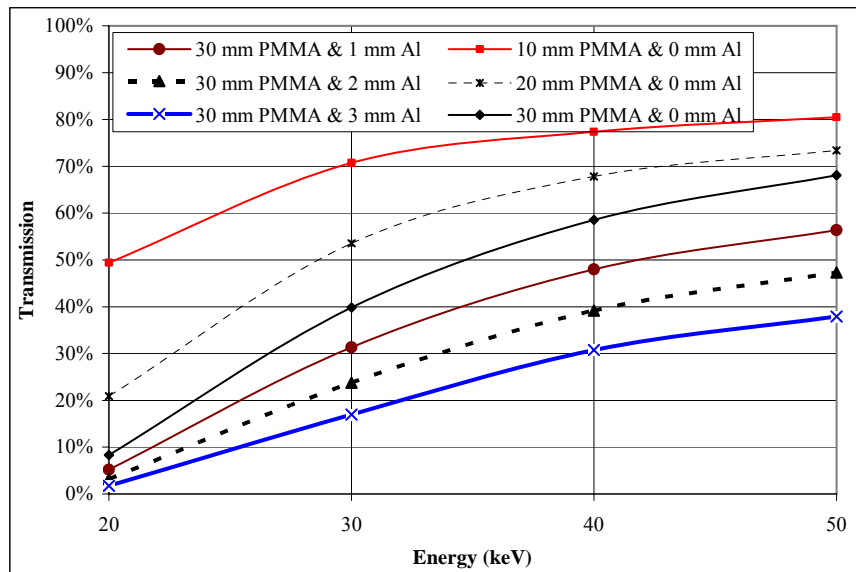


Figure 5.1-17: Transmission of different absorber steps versus energy of monoenergetic exposure. Here the average number of incident photons per image pixel was 71.5.

The average number of transmitted quanta per image pixel divided by the average number of incident quanta (here 71.5) per image pixel leads to the transmission values (cf. section 5.1.1). The error of the average number of transmitted quanta has been calculated as the standard deviation of an arithmetic average which equals the quotient of the noise (as defined in section

5.1.1) in the region of interest and the square root of the number of pixels in that region. The resulting error of the calculated transmission is below 0.5 %.

The vertical distance between two transmission curves is a measure of the contrast (as defined in section 5.1.1) between the two steps in the image they represent. Increasing the energy this distance shrinks between the upper curves which belong to thinner steps, while it is getting bigger for the thicker steps. The change can also be shown for contrasts introduced by an absorber of fixed thickness added behind differently thick main absorbers (Figure 5.1-18).

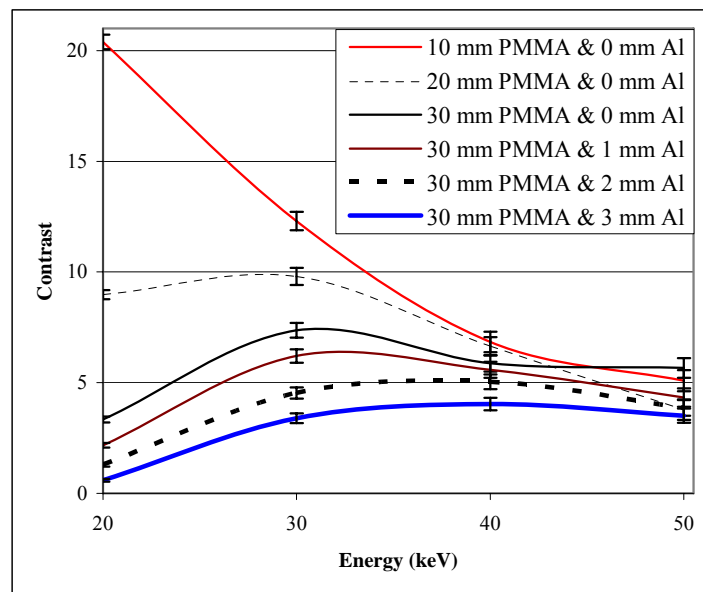


Figure 5.1-18: Energy dependence of the contrast between various main absorbers (see legend) and absorbers respectively thicker by an additional layer of 10 mm PMMA (71.5 incident quanta per image pixel).

These contrast curves show a maximum versus the energy that moves to higher energies with overall thickness of the specimen. The error of the contrast values is estimated by Gaussian error propagation. It increases with higher energies where the overall contrast gets lower. The contrast is always higher behind a thinner absorber.

The contrast introduced by a fixed absorber added to different main absorbers has to be put into relation with the arithmetic mean of noises (as defined in section 5.1.1) of the two related parts of the image. The mean noise increases with to the higher overall number of transmitted photons (Figure 5.1-19) and equals the square root of the mean pixel value as expected for Poisson statistics (cf. Eq. 4.2-14).

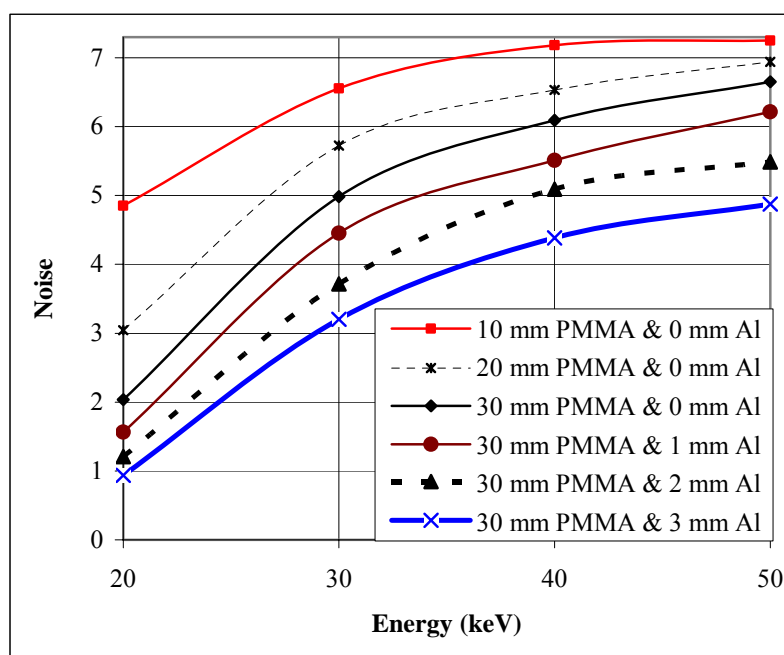


Figure 5.1-19: Energy dependence of the noise (as defined in section 5.1.1) behind differently thick absorbers (see legend) with and without an additional contrast element of 10 mm PMMA (for 71.5 incident quanta per image pixel).

The quantity giving the best information about the reproduction of contrast elements in an image is the “contrast to noise ratio” CNR_e (as defined in section 5.1.1) (Figure 5.1-20). The frequently used signal to noise ratio SNR_e (definition in section 5.1.1) for comparison is always rising with the photon energy. It is equal to the half of the CNR_e of a signal region and the zero level (cf. Eq. 5.1-4 and Eq. 5.1-5 with $d'_e = 0$). The quantity is very useful in evaluating sensor signals if they can be recorded before any processing. In digital imaging the adjustment of a zero level connected to the analog-to-digital conversion process manipulates the SNR_e . The CNR_e is not changed by this adjustment. Other processes of image preprocessing e.g. a reduction of the range of numbers all pixel values are transferred to (“pixel depth”) also change the SNR_e without a direct connection to a change in the information content of a picture. The CNR_e on the other hand is a direct measure of the representation of a contrast in the image.

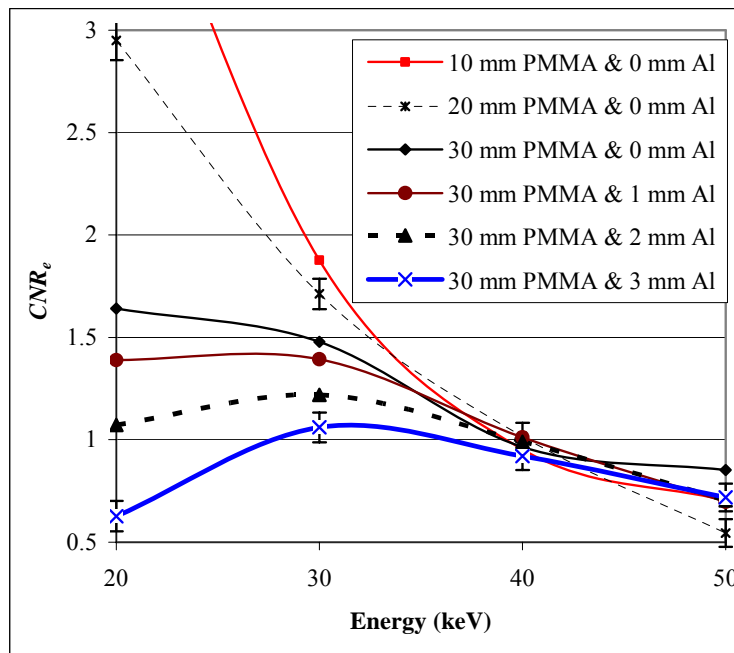


Figure 5.1-20: Energy dependence of the contrast to noise ratio CNR_e of a contrast introduced by an additional step of 10 mm PMMA behind differently thick absorbers (71.5 incident quanta per image pixel; the error bars exemplify results of Gaussian error propagation).

The division by the mean noise values does not fundamentally change the shape of the contrast curves versus the energy (Figure 5.1-20). As the noise is rising monotonously with the photon energy, the maxima of the CNR_e are slightly shifted to lower energy values. For high photon energies the noise rises higher than the contrast for all absorber thicknesses considered.

Simulations of thinner contrast elements (additional 1 mm or 1.5 mm PMMA) have not lead to further results. The contrast level was very low in connection with the limitation of the number of simulated photons (cf. section 5.1.4). Fundamental changes were not to be expected.

An additional aim of the Monte Carlo radiation transport calculation of the physical phantom was to adapt the behavior of the step structures to the regions of the voxelphantom that are of diagnostic interest. Here a scaling of the thicknesses of all present layers synchronously changes the transmission at all energies. An adjustment of the slope of the transmission curve versus the energy is achieved by the replacement of one step material by another one. E.g. the exchange of 10 mm PMMA by 1 mm aluminum lowers the transmission values for monoenergetic photons of an energy above 30 keV, at 20 keV the transmission is increased (Figure 5.1-21). This way the step structure was adapted to the overall transmission of the region of interest in a pediatric thoracic examination (Figure 5.1-21).

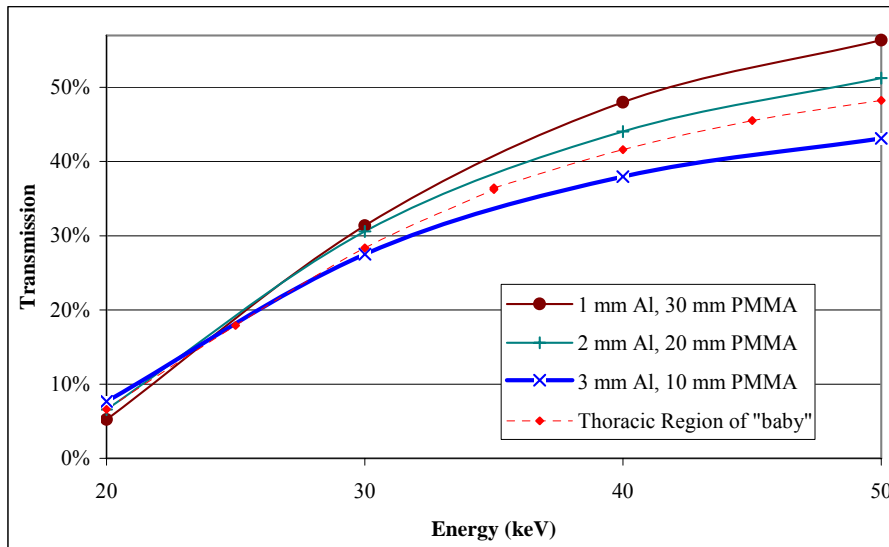


Figure 5.1-21: Comparison of the transmission curve of a step absorber phantom to the average transmission of the thorax region of the resized voxelmodel “baby” (cf. section 5.1.2).

In summary the contrast rises with increasing transmission through the main absorber and falls with the increased transmission through the contrast element. In between there can be a maximum. In order to optimize the information the contrast has to be put into its relation to the noise. The total noise rises with the energy of the incident photons as more of them reach the detector.

The energy dependence of the CNR_e is directly connected to the overall thickness of the specimen under observation: For thicker regions it rises with the transmission of the incident radiation. For thinner ones it falls as the absorption attributable to the contrast element is reduced. Voxel-models up to now do not offer an easy opportunity to analyze the imaging of fine detailed structures. Theoretical analysis will show (cf. chapter 5.2 below) that the optimum beam quality for an imaging task is to be deduced from overall transmission properties at different energies. The optimum exposure level depends on the needed contrast and spatial resolution.

5.2 Connection between Image Information and Exposure

A simplification of the imaging process to a simple model of radiography can help to aim for a task dependent quantification of its properties. Minimum exposures and corresponding beam qualities necessary for a certain gain of information in digital projection radiography can be calculated. The model is extended by the input of realistic parameters.

The model introduced below is designed from a view of imaging as a sum of statistical point processes. It therefore does not depend on system linearity or Poisson characteristics in contrast to linear systems theory (cf. chapter 4.2). Noise properties directly result from this setup without further approximation. The model developed here does not consider single interactions between radiation and matter like a modern Monte Carlo radiation transport code. Instead it employs integral absorption probabilities. Results of these different approaches are in good agreement.

It is examined how different expectations e.g. on the certainty of a result influence the radiation exposure needed. Dependencies on parameters describing the beam quality used and the detector are discussed as well. Additionally the calculations allow the determination of the best exposure in relation to patient dimensions and diagnostic needs. Especially in pediatric radiology adaptations to the patient are expected to result in great effects because of the large variations of patient sizes.

5.2.1 Model

As a simple and general approach to digital projection radiography the imaging system can be reduced to a source, a specimen, and a single detector (Figure 5.2-1). After the introduction of such a core model it is extended step by step to allow calculations of clinical relevance.

5.2.1.1 Basis

The imaging system is modeled to consist of a source of photons, a homogeneous specimen and single detector without spatial resolution properties. The basic setup is in “narrow-beam” or “good” scattering geometry where only photons that traverse the specimen without interacting reach the detector (Figure 5.2-1). This allows disregarding scattering radiation in large area contrast imaging. The later extension to “bad” geometry includes scattered radiation at the detector (cf. section 5.2.1.4).

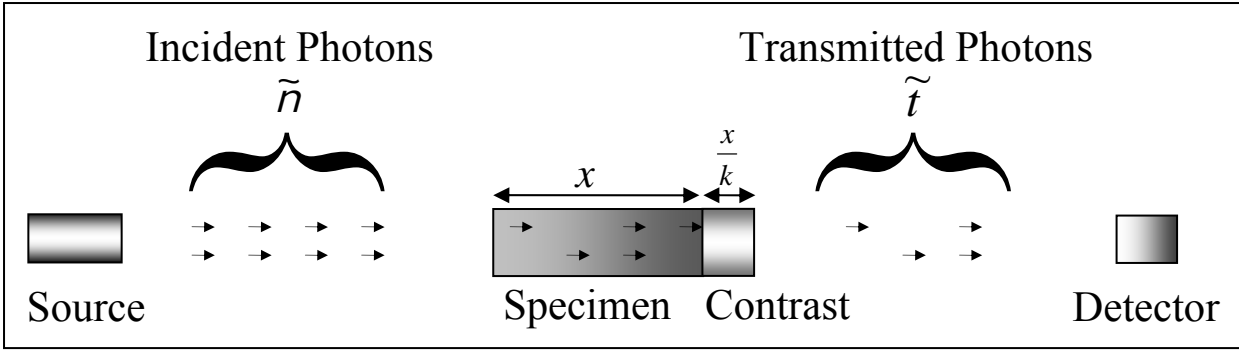


Figure 5.2-1: Model of a transmission imaging system without spatial resolution.

The source shall send \tilde{n} photons for one exposure through a main absorber (specimen) of the energy dependent absorption factor $1-p$ and an ideal detector counting all transmitted photons \tilde{t} . The measured transmission of the system \tilde{p} is given by

$$\text{Eq. 5.2-1:} \quad \tilde{p} = \frac{\tilde{t}}{\tilde{n}} .$$

The basic imaging task considered now is the identification of a change in absorption by an additional thin absorber (attenuation $(1-c)$) added in the beam line. We arbitrarily define a maximum acceptable error δ of the result for \tilde{p} to be half the difference of the transmission values with or without the “contrast” absorber

$$\text{Eq. 5.2-2:} \quad \delta(\tilde{p}) = \frac{1}{2}(p - p \cdot c).$$

The probability $P(\tilde{n})$ for \tilde{p} being in the range between $p - \delta$ and $p + \delta$ is the same as the sum of the probabilities for the count value \tilde{t} to be in a range between a lower limit $dwn(\tilde{n}, p, \delta) = \tilde{n} \cdot (p - \delta)$ and an upper limit $up(\tilde{n}, p, \delta) = \tilde{n} \cdot (p + \delta)$. $P(\tilde{n})$ is therefore calculated as the sum of the connected binomial coefficients:

$$\text{Eq. 5.2-3:} \quad P(\tilde{n}) = P(\tilde{p} \in [p - \delta; p + \delta]) = \sum_{i=dwn(\tilde{n}, p, \delta)}^{up(\tilde{n}, p, \delta)} \binom{\tilde{n}}{i} p^i (1-p)^{\tilde{n}-i} .$$

In connection with the rise of $P(\tilde{n})$ with \tilde{n} the minimum number of photons n can be determined that is necessary to gain an estimate of p in the range between $p - \delta$ and $p + \delta$ with a certainty higher than a chosen level s .

$$\text{Eq. 5.2-4: } n = \text{Min} \{ \tilde{n} | P(\tilde{n}) \geq s \}.$$

The exact solution is dependent on p, c (or δ) and s and can be calculated directly from those values. For the estimation of different circumstances mathematical computer software [78] was used (cf. Appendix C).

5.2.1.2 Energy Dependencies

In order to examine energy dependencies of the minimum number of photons n (cf. section 5.2.1.1) energy and transmission quantities have to be related. Here Compton and Raleigh scattering radiation reducing the image quality are not included into the calculation (cf. section 5.2.1.1). The results for large area contrast imaging are in good agreement with the corresponding results of the Monte Carlo calculations (cf. section 5.1.5.3) and the experiments (cf. section 6.3).

The first approach to find the energy dependence for n is to assume that p and c describe absorbers of the same material. The two attenuations of those absorbers are calculated from only one common energy dependent attenuation coefficient $\mu(E)$ and two different thicknesses (cf. section 4.3.1). We define the thickness of the main layer x and its ratio to the thickness of the contrast layer k (cf. Figure 5.2-1). The transmission will decrease exponentially with the thickness of the material:

$$\text{Eq. 5.2-5: } p = e^{-(\mu * x)}$$

and

$$\text{Eq. 5.2-6: } c = e^{-\left(\mu * \frac{x}{k}\right)}.$$

This leads to the connection of c and p for all possible values of μ and therefore for all energies which is

$$\text{Eq. 5.2-7: } c = p^{\frac{1}{k}}.$$

Thus a certain relation between c and p at one energy level connects the values over the whole range of possible absorption. This simplification enables us to use p as an energy measure, which allows for the identification of the energy dependence of n . By the choice of the same material for main absorber and contrast absorber we avoid the necessity to include the ratio

between two different attenuation coefficients into the calculation. Only if this ratio is independent from the energy the change could be absorbed into a modified definition of k .

Up to here the change between energy scale and transmission scale is not fixed to monoenergetic exposure. Every result could be equally represented against a scale of transmission independently from the spectral composition of the input radiation as far as it led to the same overall transmission. In contrast to that the following inclusion of non equal spectral behavior of different elements of the model forces results to be based on monoenergetic input radiation.

For arbitrary material compositions Eq. 5.2-6 and Eq. 5.2-7 have to be generalized to

$$\text{Eq. 5.2-8: } p = e^{-(\mu_p(E) * x)}$$

and

$$\text{Eq. 5.2-9: } c = e^{-(\mu_c(E) * x_c)}$$

The energy dependent values for the attenuation coefficients $\mu_p(E)$ for the main absorber and $\mu_c(E)$ for the contrast defining layer are well known for various materials [33]. The composition of most materials of interest in the context of radiation research is found in an ICRU publication [76].

The introduction of energy dependences is also crucial for the implementation of non ideal detectors. Without the consideration of spatial resolution properties the signal of a photon reaching the detector must be result of an interaction process in modified by small in-detector effects due to the electronics or like lag effect. In a first approach the quantum efficiency η is taken to be equal to the probability of interaction:

$$\text{Eq. 5.2-10: } \eta = 1 - e^{-(\mu_d(E) * x_d)}$$

where $\mu_d(E)$ is the linear attenuation coefficient of the detector and x_d its thickness [79].

5.2.1.3 Areal Resolution

The introduction of sizes into the model is straightforward: up to this point the model estimates exposure needs for homogeneous areas compared to each other. Pixel images can be calculated by the identification of these areas as the image pixels.

At first we consider a setup of perfect alignment of the borders of the contrast to be detected and the pixel array. In this case all conclusions made above can be taken valid for the

distinction of a pixel in the area shaded by a small detail object from its surroundings. The lateral size of a contrast object can be determined exactly.

When the contrast element is not in line with the borders of the pixel array any more conclusions about the distinction of pixels in the area shaded by the contrast from those fully exposed still hold valid. Additionally there are now pixels shaded just to a share. Information about the lateral size of a contrast object is therefore limited to the extent of the pixel size in the respective direction. If there was an edge of a contrast some factor higher than the detectable limit, distinctions e.g. between half and quarter shaded imaging elements become possible. The model described is constructed in a way that replaces the discrimination of different attenuations by the discrimination of expectation values for the detected photons. The distinction of a pixel under full exposure from another one that is illuminated just to a share equals a connected change of transmission probability from the radiation source to the pixel. Values like the minimum number of photons can be calculated just like before.

Real pixel array detectors have a sensitive area of each pixel reduced below their share of the detector surface. In this case the minimal exposure calculated has to be incident on the sensitive region.

The equality between a pixel shaded to a share and those fully illuminated but with differently attenuated radiation is used the other way around when a MTF is deduced from imaging a step edge like in the standardized method to determine the DQE [25] (cf. section 4.2.3.2).

The presence of inhomogeneities resulting from the x-ray generation like the heel effect makes it necessary to include information about where in an image pixel values have to be distinguished. If for example the model is used to determine a minimum exposure per pixel for the predefined task, this minimum exposure is necessary at the area attenuated most by the heel effect. This leads to a nominal overexposure of the other areas of the image.

The model relies on describing the probability that changes in transmission behavior lead to distinguishable pixel values. The inclusion of areal resolution is performed by application of the results to single pixels of an imaging system. There is a second effect of additional quanta scattered into a pixel from neighboring regions and building up additional background noise. This is analyzed further in the next section (5.2.1.4).

5.2.1.4 Image Noise Consideration

The model includes the examination of noise resulting from the statistical properties of quantum imaging. Other sources of random variations are present in digital radiography units. These include scatter radiation and inhomogeneities of the radiation field resulting from the imaging setup. Resulting from the image acquisition there are electronic noise, quantization

noise (from analog-to-digital conversion), structure noise (e.g. from detector imperfections) and lag effect (e.g. from a memory effect of a present intensifying screen) additionally downgrading the imaging quality.

Also variations due to real structures of the patient under examination are to be taken as disturbing the imaging process if they cover structures that have to be seen and are of no diagnostic interest themselves. This so-called anatomical noise is an important contributor to image variations in thoracic imaging [80, 81].

There are efforts to use scattered radiation for imaging purposes [82, 83]. In projection radiography scattered radiation disturbs the imaging process. The presence of scatter affects the calculations in different ways. First we consider quanta that are scattered out of the direct path and subsequently back towards the detector. Previously all scattered photons were counted as absorbed (cf. section 5.2.1.1), now the share being scattered back needs to be subtracted. In order to evaluate the impact on the results of our model we introduce a variable g as the share of the non transmitted photons being scattered back to the detector. The two “transmission” values to be discriminated are then changed to $p' = p + (1 - p) \cdot g$ and $p'c' = pc + (1 - pc) \cdot g$. The definition of the contrast as half the difference of these values then is

$$\text{Eq. 5.2-11:} \quad \delta' = \frac{1}{2}(p - pc) \cdot (1 - g) = \delta \cdot (1 - g).$$

The limits of the count value t for the correct result are tightened to $dwn(\tilde{n}, p', \delta')$ and $up(\tilde{n}, p', \delta')$. With these modifications the formulas found above still hold valid. The general statistics do not change:

$$\text{Eq. 5.2-12:} \quad P(\tilde{n}) = P(\tilde{p} \in [p' - \delta'; p' + \delta']) = \sum_{i=dwn(\tilde{n}, p', \delta')}^{up(\tilde{n}, p', \delta')} \binom{\tilde{n}}{i} p'^i (1 - p')^{\tilde{n}-i}$$

If the new variable g is set to zero the formulas turn out the same as before. With rising g it gets harder to get $P(\tilde{n})$ above a predefined level (cf. section 5.2.1.1). An inclusion of energy dependences into the value of g seems adequate, because the dominant effect of interaction between radiation and matter changes from photo absorption to Compton scattering with rising energy.

The second influence of scatter radiation is most relevant for imaging of a detail in homogeneous surroundings: the addition of background noise to the imaging setup. The following inclusion of scattering as a source of background noise is applicable to the other noise sources mentioned above. Like in the previous considerations we introduce the background as an additional source of quanta reaching the detector.

The total number of quanta \hat{n} directed elsewhere is taken to be proportional to the number \tilde{n} counting the quanta directed from the source to the detector:

$$\text{Eq. 5.2-13:} \quad \hat{n} = \tilde{n} \cdot k$$

with the proportionality factor k . Introducing the probability f of one of those quanta being scattered into the detector leads to an additional binomial distribution to be included into the previous result (Eq. 5.2-12).

$$\text{Eq. 5.2-14:} \quad \hat{P}(\tilde{n}) = \text{P}(\tilde{p} \in [p'' - \delta'; p'' + \delta']) = \sum_{i=dwn''(\tilde{n}, p', \delta', k, f)}^{up''(\tilde{n}, p', \delta', k, f)} \sum_{j=0}^i \binom{\tilde{n}}{i-j} p'^{(i-j)} (1-p')^{\tilde{n}-(i-j)} \binom{\tilde{n}k}{j} f^j (1-f)^{\tilde{n}k-j}.$$

There is no change in the desired contrast resolution δ' , the expected average count value for the detector is changed to $p'' = p' + kf$. The limits of the count value t for the correct result are shifted up correspondingly to

$$\text{Eq. 5.2-15:} \quad dwn''(\tilde{n}, p', \delta', k, f) = \tilde{n}(p' + kf - \delta') \text{ and}$$

$$\text{Eq. 5.2-16:} \quad up''(\tilde{n}, p', \delta', k, f) = \tilde{n}(p' + kf + \delta').$$

The value of $\hat{P}(\tilde{n})$ gives the probability that in the model setup the detector recognizes a number of photons in a correct range defined by main absorption and contrast. The minimal exposure can still be defined as threshold number that gets this probability of a correct result above a predefined level (cf. Eq. 5.2-4).

5.2.2 Results for Large Area Contrast

The model described in 5.2.1 leads to various results for the large area contrast detection modeled. It is used for the quantification of well known relations as well as for the derivation of statements about optimal settings for this detection process.

5.2.2.1 Minimal Dose Dependencies on Desired Certainty

The minimal number of photons required for the imaging task defined above is dependent on the certainty level s of the desired gain of information. For even the highest number of photons sent through an absorber the measured absorption \tilde{p} will not be in the range defined by the maximal error δ around p with 100% certainty. Therefore if the desired certainty is set to one an infinitely high number of photons n or dose is required. The exponential rise of n with s is bent up against that limit. It is bent down close to $s=0\%$ for similar reasons. Figure 5.2-2 shows the dependence with the transmission of the main absorber fixed at $p=50\%$ and the contrast transmission fixed at $c=99\%$.

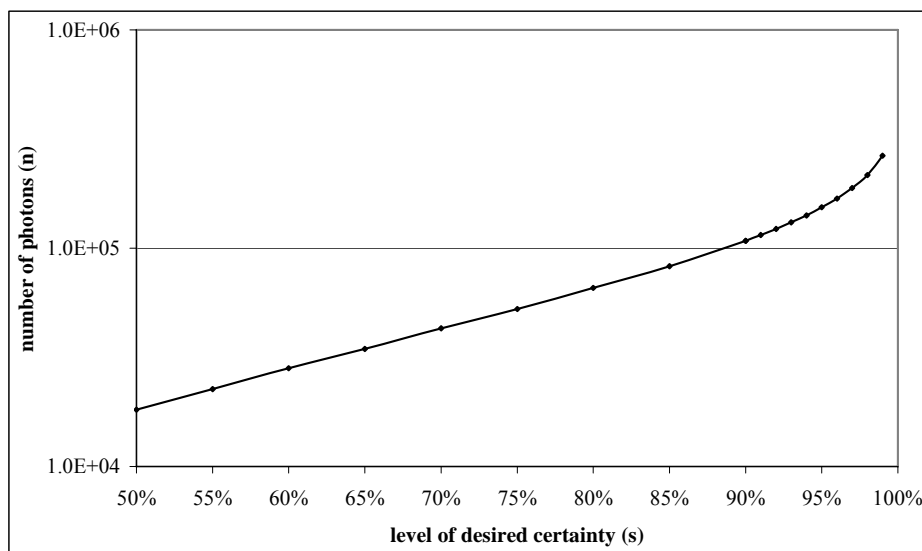


Figure 5.2-2: Exponential and over exponential rise of input photons n needed with the desired level of certainty s for a correct determination of the main absorption of $p=50\%$ at $c=99\%$.

For comparison the dependence of n on the transmission of the contrast c defining the width of the aiming interval is examined while the level of desired certainty is fixed at $s = 99\%$. For a fixed value of p n shows behavior similar to the variation of the certainty level (Figure 5.2-3): even the highest number of input photons cannot detect a contrast element of $c = 100\%$ transmission.

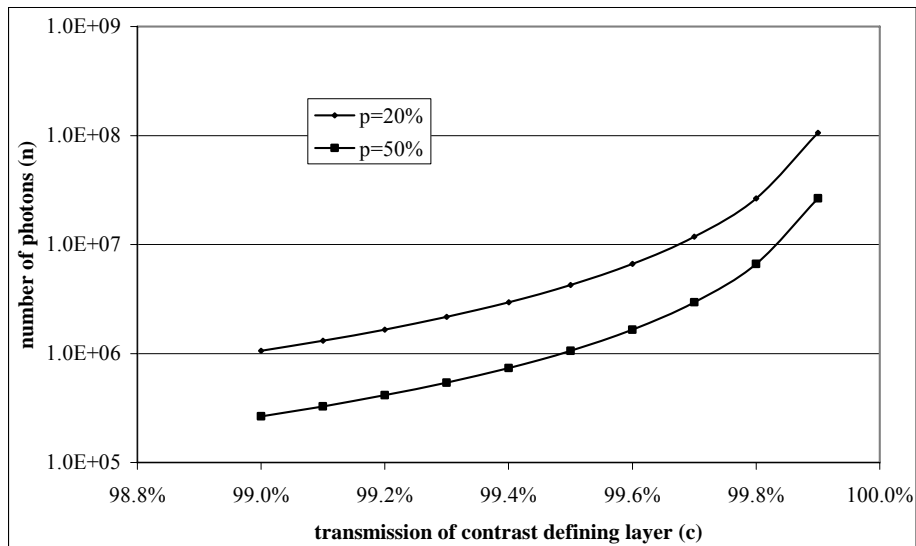


Figure 5.2-3: Over exponential rise of n with the transmission c of the layer defining the contrast.

With c rising from 99% to 99.9% the exposure sufficient to fulfill the imaging task rises approximately by a factor of 100. This result is consistent with the theoretical need for a hundredfold higher number of quanta for the tenfold higher information content.

5.2.2.2 Mutual Dependence of Minimal Dose and Energy

In order to get quantitative data about the change of n (Eq. 5.2-4) with an energy related figure the relation between p and c is fixed at a certain level and their variation synchronized through equation Eq. 5.2-7. The connection represents a certain thickness ratio between a main absorber and a layer of the same material defining the contrast one wants to resolve.

Figure 5.2-4 shows the change of the contrast transmission with main absorber transmission resulting from the connection for an example of $c=99\%$ at $p=50\%$ which leads to a thickness ratio of 1:69 ($k = 69$; Eq. 5.2-7).

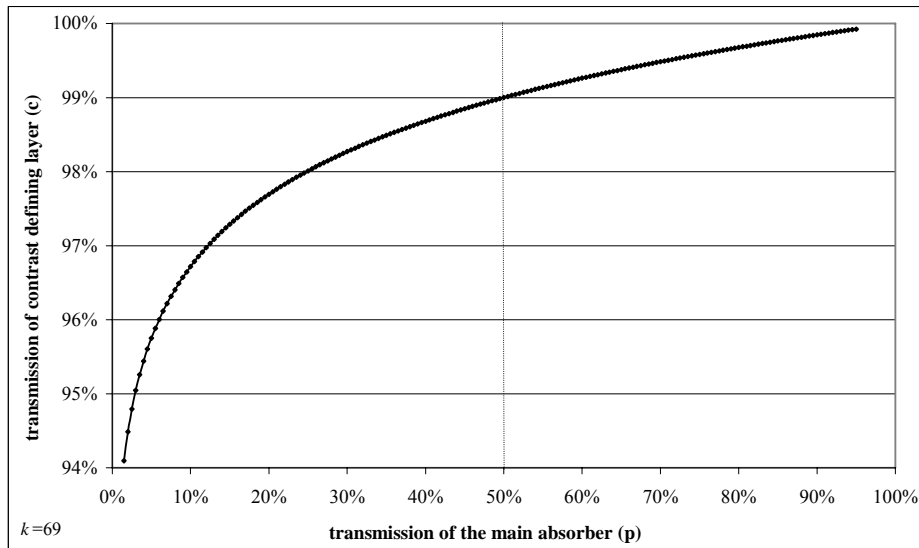


Figure 5.2-4: Coupled change of transmission of the main absorber p and the contrast absorber c representing homogeneous bodies of different thicknesses. The thickness of contrast defining layer is $1/69$ of the thickness of the main absorber in the data shown ($k=69$).

As the model is made to describe diagnostic radiography with every change of the main transmission p there has to be an appropriate change of the transmission c .

The connected variation of the transmissions present in this model makes it possible to use p as a measure of penetration strength. In the radiological context the quantity is directly connected to photon energy. The minimum exposure n can be plotted against it (Figure 5.2-5).

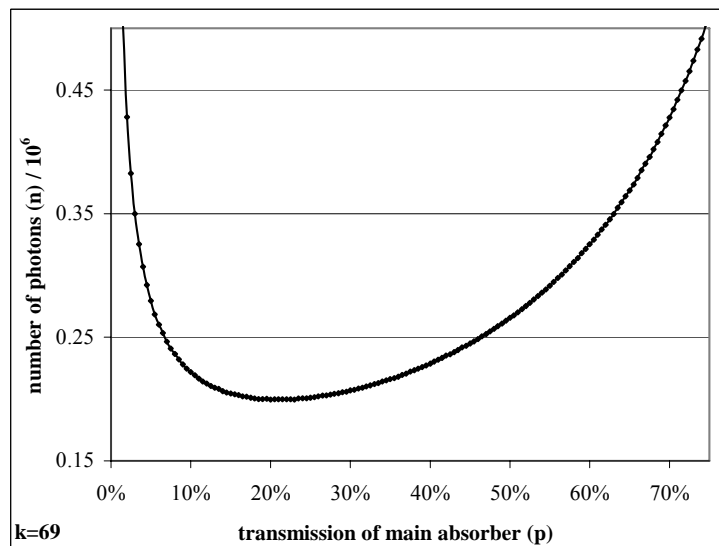


Figure 5.2-5: Number of photons n needed for the discrimination of a contrast transmission c behind a main absorber of transmission p connected by a ratio of thicknesses of $1:69$ which leads to $c = 99\%$ at $p = 50\%$.

The resulting dependence of n from p by one finds a minimum for the exposure at $p \approx 20\%$. A change in the energy of the input photons leading to a transmission of p just below 4.5% or just above 55% leads to a rise of n by a factor of 1.5. The change of the thickness ratio chosen to define the contrast resolution changes the values for n but does not change the shape of the curve. For example if c is set to $c = 99.9\%$ instead of $c = 99\%$ at $p = 50\%$ then n rises by a factor of hundred (Figure 5.2-6 and Figure 5.2-7). Similarly to the rise to the tenfold higher certainty (cf. section 5.2.2.1) the tenfold lower contrast detection needs a hundredfold higher dose. However the position of the minimum of n does not change due to these changes.

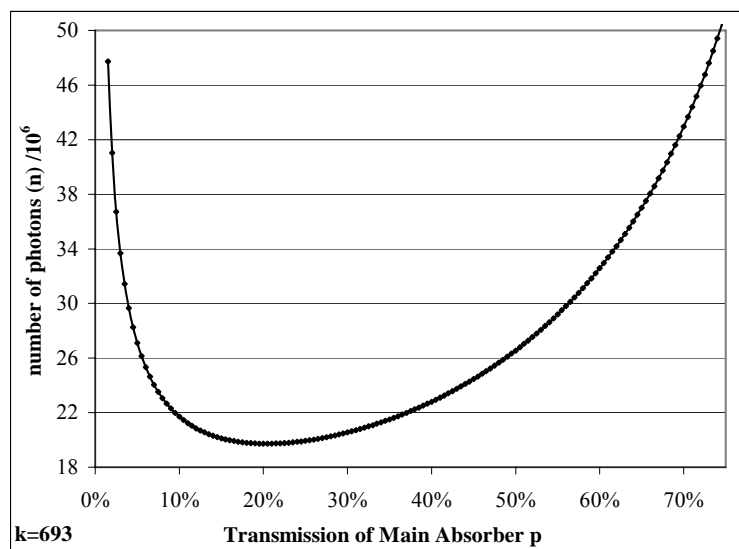


Figure 5.2-6: Number of photons n needed for the discrimination of a contrast transmission c behind a main absorber of transmission p connected by a ratio of thicknesses of 1:693 ($k=693$) which leads to $c = 99.9\%$ at $p = 50\%$.

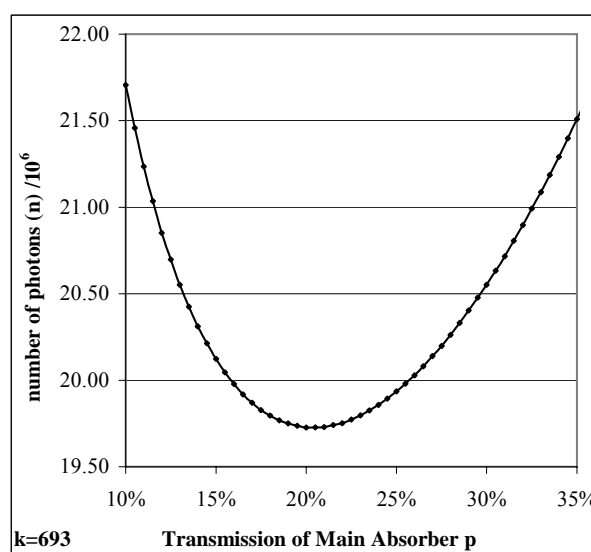


Figure 5.2-7: Minimum in the number of photons n needed for the discrimination of a contrast transmission c behind a main absorber of transmission p connected by a fixed ratio of thicknesses ($k=693$).

The material defining the contrast can be specified separately from the main absorber (Eq. 5.2-8 and Eq. 5.2-9) in order to generalize the setup. If the contrast is defined by a material different from the main absorber the minimal effort is moved away from the value of $p = 20\%$ and gets dependent on thickness ratios. In order to compare the curves of different thicknesses the number of needed photons n is divided by the respective minimum (Figure 5.2-8).

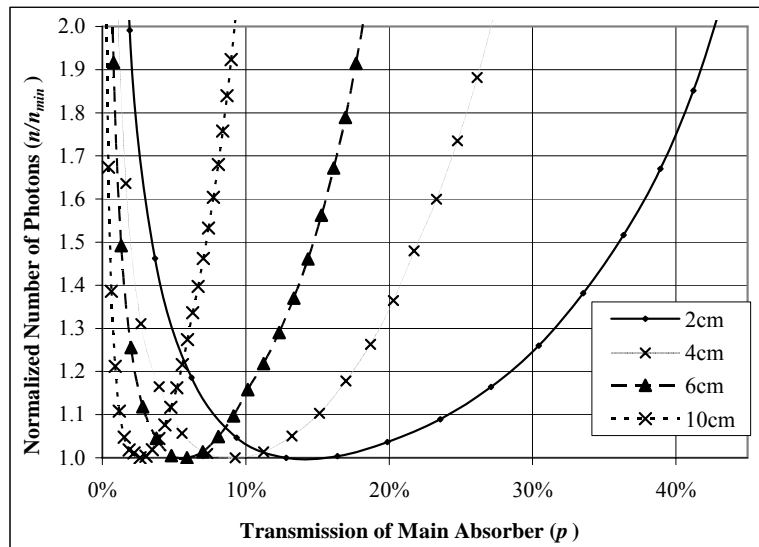


Figure 5.2-8: Number of photons needed to detect 100 μm bone (ICRP) behind differently thick blocks (cf. legend) of soft tissue (ICRP) divided by the respective minimal value versus transmission of the system.

In order to detect a thin layer of cortical bone contrast behind a layer of soft tissue it turns out to be useful to measure at a lower overall transmission for thicker specimens. It is not necessary to raise the energy in a way that keeps the overall transmission constant as would be indicated for the case of just a thickness contrast.

The specification of the material directly connects the transmission through the setup to the energy of radiation from a source of specific spectral behavior. E.g. the transmission scale can be translated directly to energy of monoenergetic exposure (Figure 5.2-9).

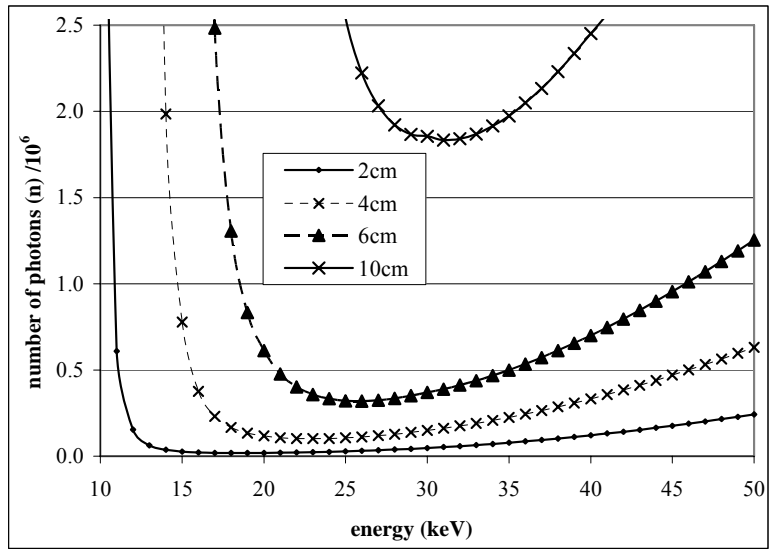


Figure 5.2-9: Number of photons needed to detect 100 μm bone (ICRP) behind of differently thick blocks (cf. legend) of soft tissue (ICRP) with an ideal detector.

It is found that most photons are needed for the detection behind the thickest main absorber as expected. The exposure leading to the information desired for a thick main absorber is always sufficient to gain the information for all thinner absorbers.

In order to evaluate the change of the shape of the curves the needed exposure is again normalized to their individual minimum (Figure 5.2-10). This way the values of the ordinate are giving the factor by that n is above the minimal value for each specimen combination.

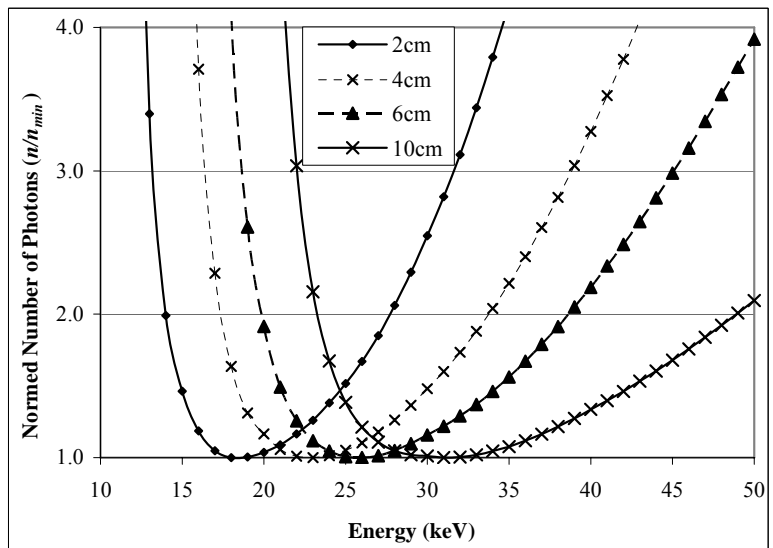


Figure 5.2-10: Numbers of photons needed to detect 100 μm bone (ICRP) behind different thicknesses (cf. legend) of soft tissue (ICRP) with an ideal detector divided by their respective minimum value.

With rising thickness of the specimen the minimum moves to higher energies and becomes wider. In spite of that the shape of the curves keeps always similar in relation to the energy where the minimum is found: An additional division of the energy scale by this energy for each curve reveals how n changes if the energy is displaced by multiplication with a factor below or above the optimal value (Figure 5.2-11 and Figure 5.2-12).

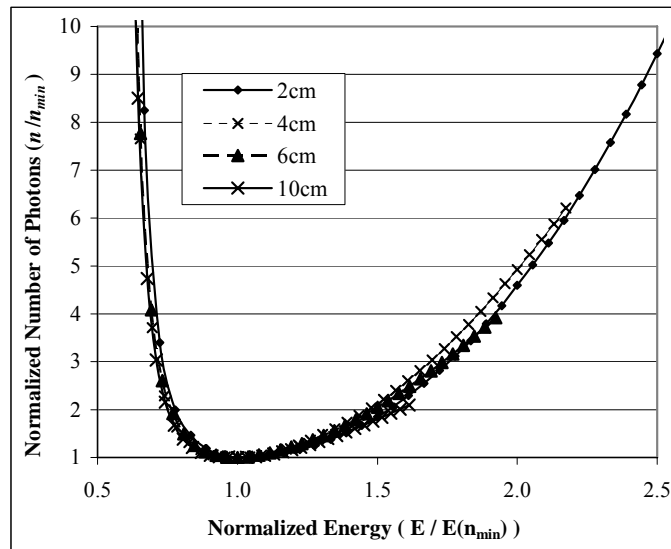


Figure 5.2-11: Number of photons needed to detect 100 μm bone (ICRP) behind differently thick blocks (cf. legend) of soft tissue (ICRP) divided by the respective minimum value versus the energy normalized to the energy of the minimum.

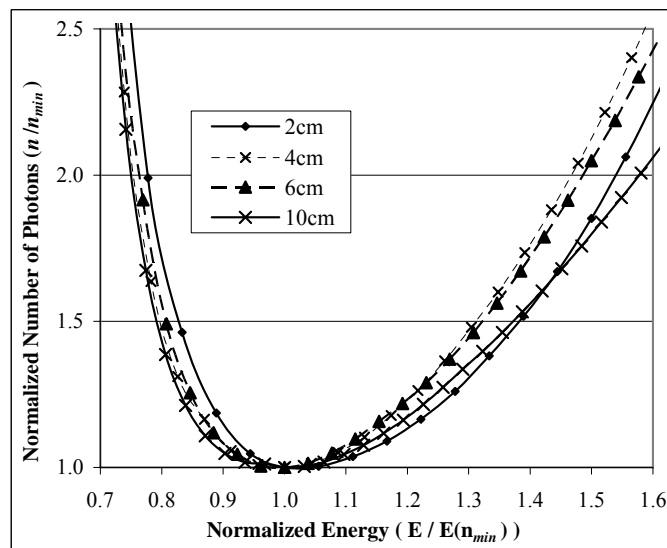


Figure 5.2-12: Minimum in the normalized number (see text) of photons needed to detect 100 μm bone (ICRP) behind differently thick blocks (cf. legend) of soft tissue (ICRP) versus the normalized energy (see text).

It is found that the resulting curves are very similar. Regardless of the overall thickness of the specimen a change of the energy from the respective optimal value by a factor the number of necessary photons is altered by a connected factor. For example a change of the quantum energy by a factor of 0.76 or 1.5 approximately doubles the number of quanta needed for all overall thicknesses (Figure 5.2-12 right).

At last it was examined if there was an influence of the thickness of the contrast layer (Figure 5.2-13 and Figure 5.2-14).

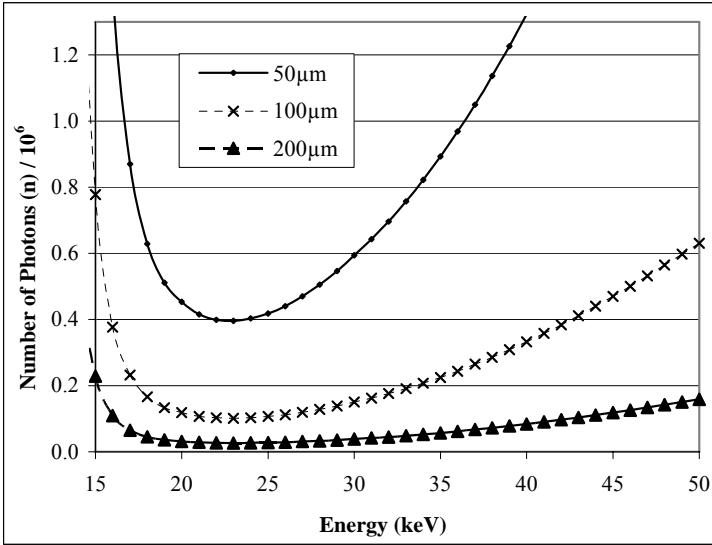


Figure 5.2-13: Number of photons needed to detect bone (ICRP) layers of three different thicknesses (cf. legend) behind a block of 4 cm soft tissue (ICRP) with an ideal detector.

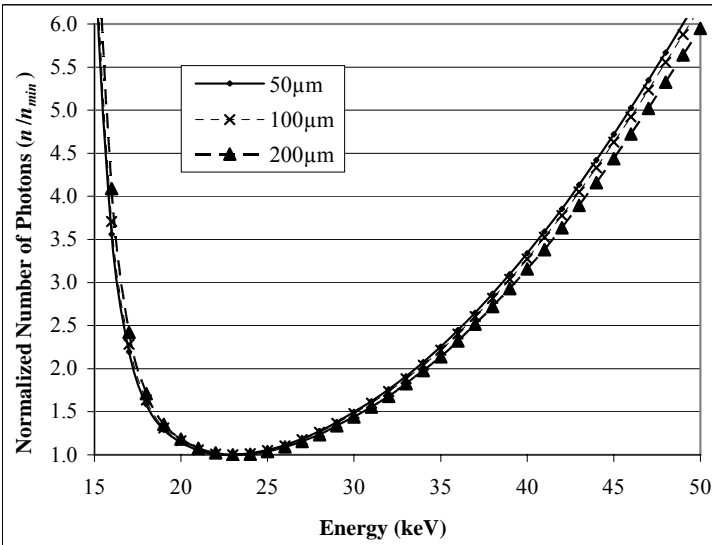


Figure 5.2-14: Number of photons normalized to their respective minimum value needed to detect bone (ICRP) layers of three different thicknesses (cf. legend) behind a block of 4 cm soft tissue (ICRP) with an ideal detector.

The relationship that a change of the contrast thickness is connected to a change in needed quanta proportional to the inverse of the square root is still valid. Dividing the curves by their minimum again, shows that there is no other influence (Figure 5.2-14).

The specification of materials also allows the inclusion of the energy dependence of the detection: The results are weighted with the quantum efficiency (as defined by Eq. 5.2-10) of the detector material taking into account their effective thickness (Figure 5.2-15).

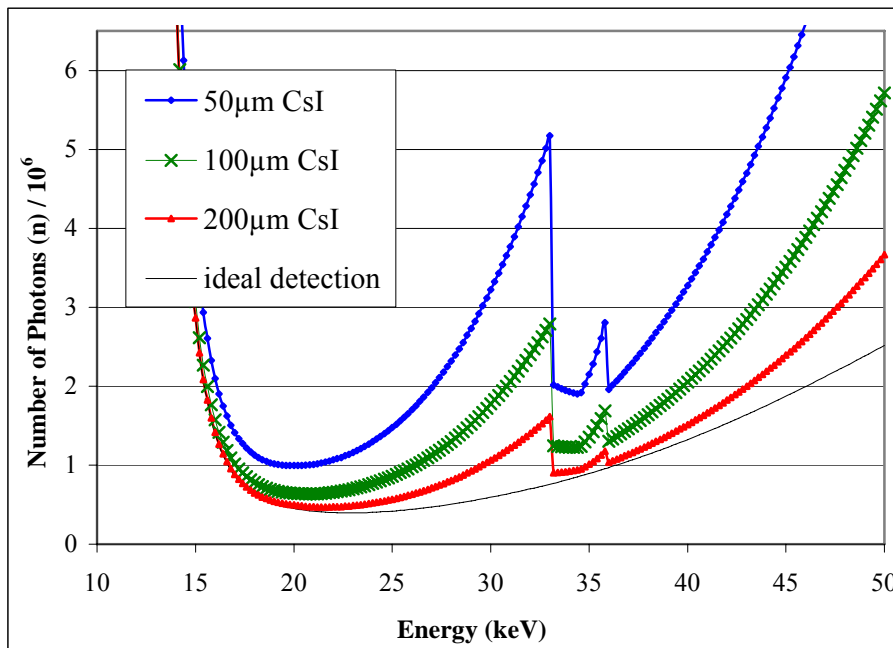


Figure 5.2-15: Minimum number of monoenergetic photons necessary to detect a 100µm bone layer (cortical bone ICRP) behind 4cm of soft tissue. The detection is approximated by the absorption of differently thick CsI-screens and an ideal detector.

Including a detector this way leads to an overlay of the results found before with the properties of the detection. As the re-absorption of detectable photons generated in a scintillator like CsI and the change of the resolution by their scattering in thicker detection layers are not taken into account the thickest sensitive layer will always lead to the best results because of its most effective absorption.

The position of the optimal energy might change abruptly with the presence of absorption edges of the detector material in the relevant range. For a given detector thickness, at a special thickness of the specimen, the measurement can get equally efficient above and below an absorption edge (Figure 5.2-16).

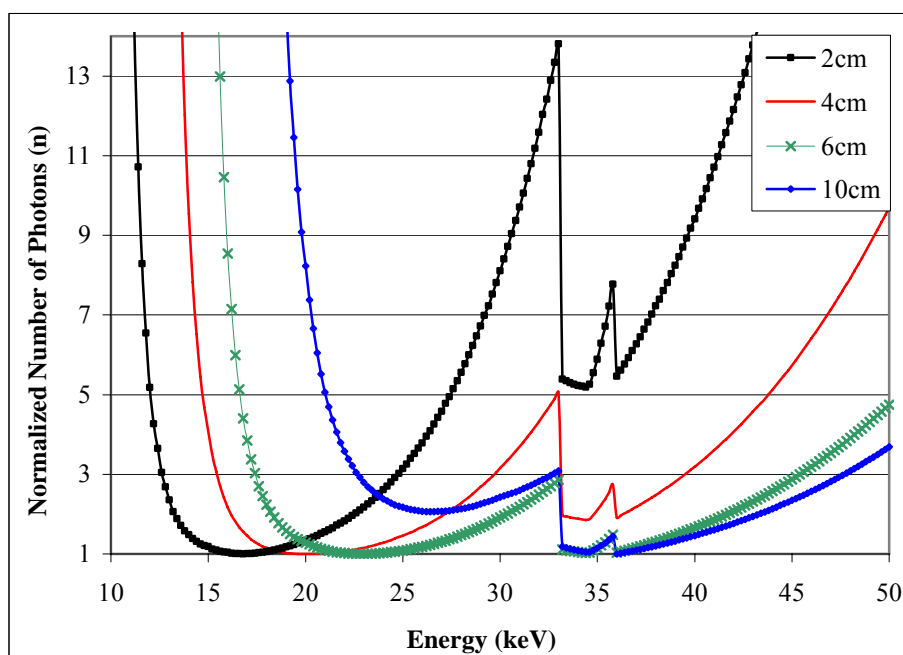


Figure 5.2-16: Number of monoenergetic photons necessary to detect a 100 μ m bone layer (cortical bone ICRP) behind different thicknesses of soft tissue (cf. legend) divided by their minimal value using a 50 μ m CsI-screen.

At a thickness of 6cm there are three virtually equivalent minima at 23 keV, 34 keV and 36 keV.

Also with this implementation of detector sensitivity into the model it is still seen that a misadjustment of the energy towards higher energies causes less detriment than a misadjustment to lower ones. This is especially true if there are absorption edges of the detector material for energies just slightly higher than the expected energy of the minimal dose. Thin objects lead to a tighter minimum around the optimal energy.

5.2.3 Results for Areal Resolution

Modifications in order to include areal resolution into the described model (cf. chapter 5.2.1.3) are leading to direct multiplication of the previous results with the number of pixels introduced whenever the task is to differentiate if a contrast layer is present or not between the radiation source and each pixel. The calculated number of photons is needed to be sent towards the sensitive area of each pixel.

In addition it may become necessary to distinguish if a pixel is half or three quarters shaded by a contrast layer in order to find edge-structures. The distinction of a pixel fully exposed from another one half-shaded by a contrast of transmission $c = 99\%$ turns out equal to its distinction from a pixel fully shaded by a contrast of transmission $c = 99.5\%$. It should be stressed that the desired certainty level s can be chosen lower if straight edge structures are to

be found as correlations between neighboring pixels can be evaluated. The inclusion of knowledge about the specimen in general can heavily reduce the imaging complexity. The measurement of the size of an object gets easier if location and especially shape are known.

5.2.4 Results for Noise Consideration

The variables defined in order to include the influence of noise (cf. section 5.2.1.4) describe various influences on an imaging system.

The share g of the quanta scattered out of line between source and a single detector being scattered back will be negligible ($g \approx 0$) in most cases. It has been introduced as the resulting formula can be used to investigate a pixel imaging system without absorption and just scattering at low angles. If in this case g is extended by the probability that photons scattered out of one beam line from source to pixel are replaced by those from other beam lines it can get close to unity. For regions of similar overall scatter properties (described by p) the identification of a contrast becomes impossible (cf. Eq. 5.2-11 and Eq. 5.2-12).

In the general description the factor g can be absorbed into the variable f as the probability of a photon directed elsewhere being scattered towards the detector. The factor is of the same magnitude as g but effectively weighted with all radiation the specimen is exposed to. The connection to the number of quanta sent in order to solve the imaging task is made by the inverse of the share of all radiation generated that is primarily directed to the detector of interest (k). In pixel imaging the number is at least equal to the pixel count. The product of both values leads to the significant expectation value of a background pixel count.

The three variables are depending on the geometrical setup of the source and the detector (mainly acting on k), the specimen materials, size, structure and orientation, and especially on the radiation quality (changing g and f).

A change of the results about the connection of minimal dose and energy of the applied photons (cf. section 5.2.2.2) is to be expected due to the change of the dominance of photo absorption to that of Compton scattering with higher energies. The minima found are expected to move to lower energies. The differences found for monoenergetic exposure result in different weighting when the results are combined in order to evaluate different spectral compositions of input radiation. Nevertheless the method still gives measures of efficiency for every level of energy that can be used as weight factor in this combination.

The structure of Eq. 5.2-14 can be understood as a convolution like combination of two binomial distributions. It directly shows how the inclusion of noise quantities demands higher exposure for the same contrast detection experiment by the inclusion of a second set of

binomial coefficients. The model combines different sources of image noise as pure statistical point processes. Mathematical approximations connect this exact result to the view of quantum imaging as combination of Poisson processes [21].

It is stressed that in the task definition described in this model the contrast to be detected is a quantity set into relation with the statistical variations of the system as the noise components. It can not be improved by image processing as it is defined to be a measure of information content. Image processing can help to visualize that what is present in an image dataset but it cannot generate information [84].

6 Measurements

In order to put the results of the simulations and the model calculations into connection with clinical x-ray systems experiments were performed at different computed radiography (CR) systems [85].

6.1 X-Ray Tube Behavior

Measurements for the characterization of the x-ray unit are performed in order to give a general idea about the switching behavior and stability of this kind of a system. It turns out that with exposure times in the range of a few milliseconds the tube voltage setting does not give direct information about the spectral composition of the generated x-ray field. The switching behavior of x-ray tubes is similar for all clinical systems due to their general construction [86]. The investigation is necessary in order to correctly relate the clinical phantom imaging results to the previous calculations.

Most extensive experiments made use of a mobile x-ray unit with a telescopic x-ray tube arm. A high-power high frequency x-ray generator (100 kHz) applies a tube voltage of 40 kV to 125 kV in 1 kV steps to the x-ray tube. The tube filtering was 2.5 mm Al, additional filters were not used. The corresponding x-ray spectra are found in different sources [69]. The nominal focal spot could be switched between 0.6 mm and 1.5 mm. The tube current time product could be adjusted between 0.1 mAs and 100 mAs or 320 mAs depending on the focal spot size. The exposure time could be adjusted from 1 ms to 5.3 s. The tube had a rotating tungsten anode; the anode angle was 14°.

Measurements of the switching behavior were performed using a commercial diagnostic dosimeter [87]. The accuracy of the dose and dose rate measurements is better than 5 % [87], the connected precision was found from repeated measurements to be better than 1 %. Backscattering was excluded by the detector setup of the dosimeter [86, 87]. The imaging of the phantom (cf. chapter 5.1.3) was performed at a distance of 1 m between the focal spot and the phantom entrance layer. The output dose behind one of the thinner steps was kept approximately constant at about 5 μ Gy in order to keep the CR reading system in a single operating mode. This was achieved by the adjustment of the mAs product at each setting of the tube voltage. As the setting of the mAs product was not continuously adjustable fixing the dose behind 20 mm PMMA at 5 μ Gy was achieved with a variation of 25 %. The Variations have to be taken into account when imaging properties are analyzed.

The following table gives the dose measurement results at the entrance side and exit side of the phantom:

Setting		Measurement	
kV	mAs	Dose 1 (μGy)	Dose 2 (μGy)
40	8.2	86.0	6.2
45	3.2	45.7	4.3
50	2.0	37.9	4.3
55	1.6	37.2	4.5
60	1.0	26.8	3.6
65	0.8	26.9	3.9
70	0.64	25.8	4.3
80	0.4	20.6	3.7
100	0.25	20.6	4.2

Table 6.1-1: Results of the dose measurements at the entrance side (dose 1) and exit side (dose 2) of the phantom (rounded to 0.1 μGy steps).

To evaluate the image data achieved regarding the effective spectra it is necessary to check the effective tube voltage and dose rate over time. Effects of tube voltages not adjusted at small exposure times influence the result. Therefore the adoption of the preset tube voltage at the different settings as above was examined by a suitable dosimeter (Figure 6.1-1 and Figure 6.1-2).

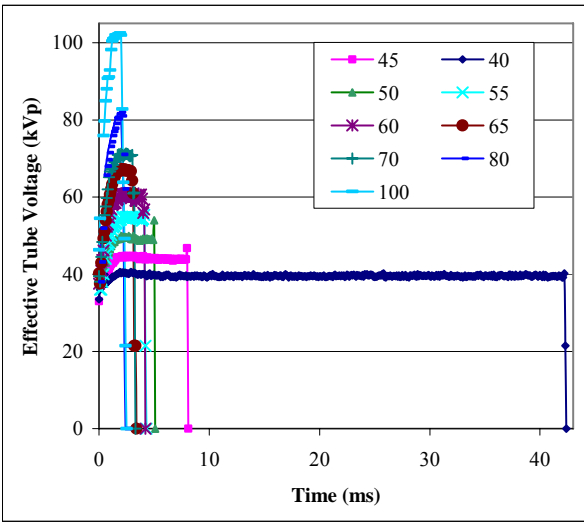


Figure 6.1-1: The overall variation in time of the effective tube voltage for an exposures leading to $\sim 5 \mu\text{Gy}$ behind 20 mm PMMA at different tube voltage settings (see legend).

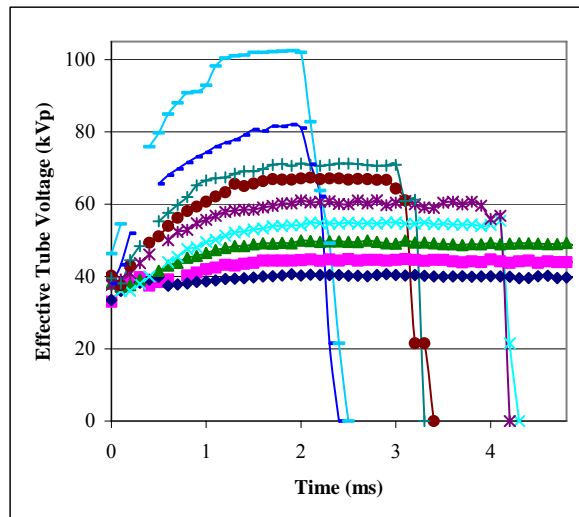


Figure 6.1-2: The power up behavior of the effective tube voltage for an exposures leading to $\sim 5 \mu\text{Gy}$ behind 20 mm PMMA at different tube voltage settings (legend see Figure 6.1-1).

The dosimeter was chosen to be capable of evaluating the incident x-ray spectrum to calculate the tube voltage used for its generation. The accuracy of the output of the effective tube voltage is better than 5 % according to the manual [87]. Apart from a switching gap shortly after the start of the exposure measurements are taken at a rate of 10 ms^{-1} [87] and exported accordingly in a text file. It is seen that the voltage set is reached just after 1.5 ms to 2 ms. For higher tube voltage settings above 50 kV the total exposure time adopts values in the same range as the output dose behind 20 mm PMMA is still fixed. A significant share of the exposure is thus generated with quanta of lower energy than expected from the spectrum corresponding to the values set.

In contrast to the gradual increase the tube voltage falls off very steep at the end of exposure. Even the slowest decrease at the highest tube voltage setting is faster than 0.5 ms.

Simultaneously to the effective tube voltage the effective dose rate is measured on the entrance side of the phantom (Figure 6.1-4).

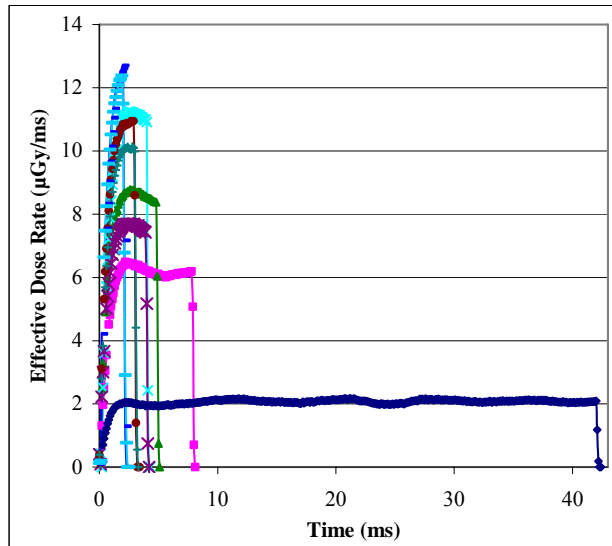


Figure 6.1-3: The overall variation in time of the effective dose rate for an exposures leading to $\sim 5 \mu\text{Gy}$ behind 20 mm PMMA at different tube voltage settings (see legend Figure 6.1-2).

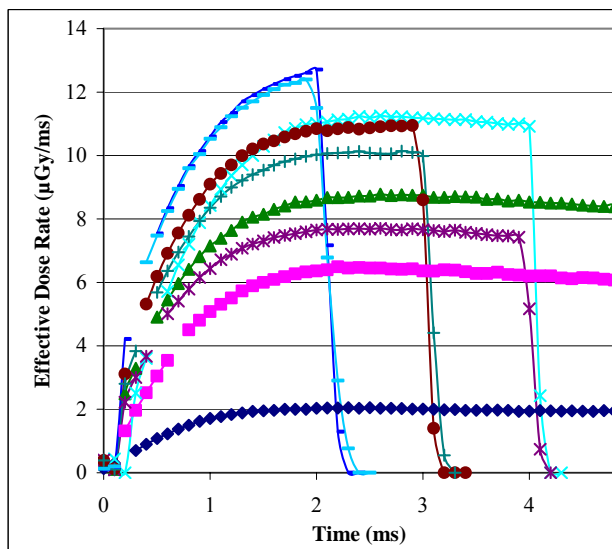


Figure 6.1-4: The power up behavior of the effective dose rate for an exposures leading to $\sim 5 \mu\text{Gy}$ behind 20 mm PMMA at different tube voltage settings (see legend Figure 6.1-2).

The rise to the maximum of this value is slower than the rise of the corresponding effective tube voltage. This is corresponding to the combined up regulation of the tube voltage and the tube current. The time integral over the dose rate gives the dose values for the entrance surface of the phantom (dose 1).

Variations of the effective tube voltage during the exposure are below 2 %. They are very fast and can be attributed to a measurement error of the tube voltage estimation or to variations from the high frequency high voltage generation (Figure 6.1-5).

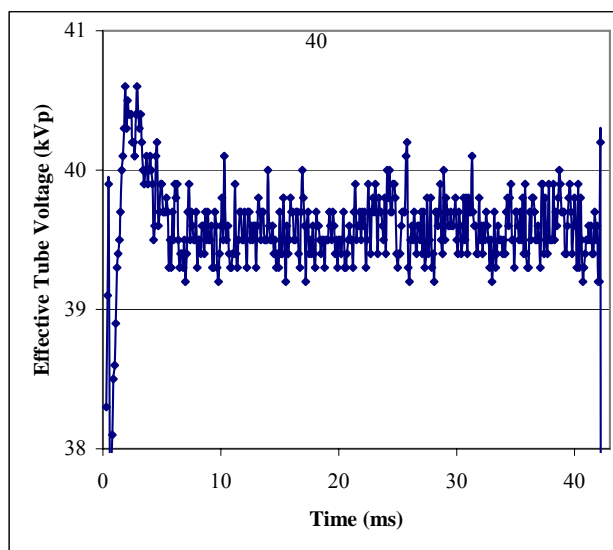


Figure 6.1-5: Variations of the effective tube voltage during the exposure with tube voltage set to 40 kV.

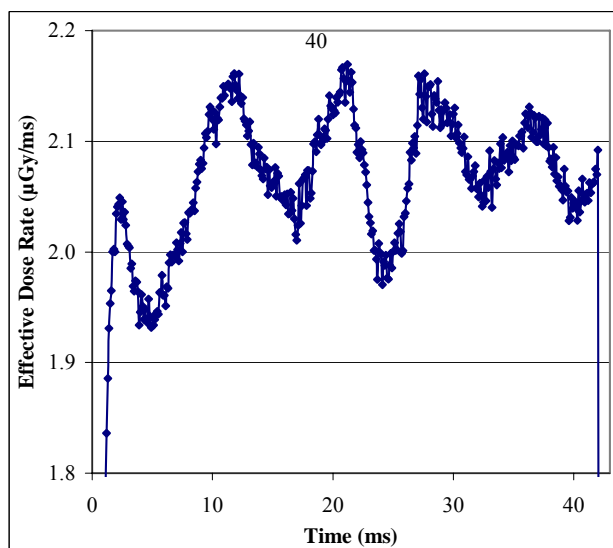


Figure 6.1-6: Variations of the effective dose rate during the exposure with tube voltage set to 40 kV.

The effective dose rate shows higher variations (Figure 6.1-6) up to about 5%. They show a periodic pattern with a frequency of about 125 Hz. As the tube voltage is constant in this frequency range and temperature variations e.g. of the hot cathode are not likely to be that fast the variation is most probably due to inhomogeneities of the rotating anode. The repetition rate would correspond to a rotation at about 7500 rounds per minute.

6.2 Imaging and Image Evaluation

Phantom images were of two crossed step like structures are taken. This is in order to be able to experimentally verify the results of the Monte Carlo simulations (cf. sections 5.1.3 and 5.1.5.3) and to put the results into relation to those of the model of information content and dose (sections 5.2.2, 5.2.3 and 5.2.4).

The physical phantom used is a modular setup of two crossed step-like structures of PMMA (10 mm steps) and aluminum (1 mm steps). On each step an element of 1 mm or 1.5 mm PMMA can be added to provide a low contrast step in the resulting images. The clearly structured setup of the phantom is relatively easy to be built in real (Figure 5.1-4) as well as easy to be virtually generated in the Monte Carlo simulation environment (cf. section 5.1.3).

Images of the phantom were taken at diverse x-ray units using three clinical CR systems. Two of these were based on conventional powder storage phosphor screens ($\text{BaFBr}_x\text{I}_{1-x}:\text{Eu}^{2+}$), one was manufactured to form needle structures ($\text{CsBr}:\text{Eu}^{2+}$) for enhanced spatial resolution [88]. The evaluation of the images was performed with the same imaging software tool kit and code as the evaluation of images resulting from the Monte Carlo Simulations [70]. The images can be adjusted to clearly show the 1 mm steps of aluminum and the 10 mm steps of PMMA are clearly seen in the images. Lower steps of 1 mm or 1.5 mm PMMA are hard to visualize (Figure 6.2-1).

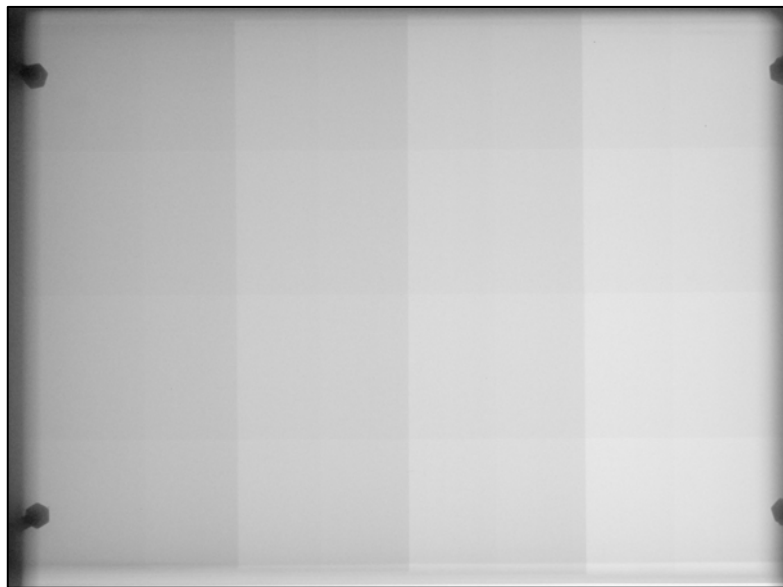


Figure 6.2-1: Radiograph of the phantom of two crossed step structures

The regular structure of the phantom is useful for automated evaluation of the images. As the lower steps covered about a third of their area the 16 clearly visible ones are divided into three regions of equal size. Misalignments between the resulting grid and the real material edges

could lead to wrong values of averages and standard deviations attributed to a certain step. In order to avoid these errors just the central parts of the regions were analyzed (Figure 6.2-3). The images are not exposed homogeneously over their whole area. The rotating anode is tilted between the direction to the hot cathode and the direction to the detector resulting in the so called Heel effect: The radiation generated from bremsstrahlung of incoming electrons is attenuated by the anode material corresponding to the length it travels through the anode material. There are parts of the specimen and detector exposed to radiation that is attenuated by a thicker layer of anode material than others because of the geometry. These parts will receive comparatively lower exposure. Also the spectral composition of the radiation is changed as low energy quanta are attenuated disproportionately stronger. These changes of intensity and spectral composition by the geometry of x-ray generation have been measured for similar systems as those used in this work [89]. The input differences are limited to about 10 %. The changes of the radiation field on each step as well as the whole phantom can be visualized directly or analyzed along line profiles (Figure 6.2-2). The heel effect was found to be stronger in the direction chosen for the aluminum step structure. It reduces the pixel values close to the edge of the image much more severe than the difference caused by 1 mm aluminum. In the central part of the image the change of the step thickness is the dominant factor changing the pixel value. Along the PMMA step structure the heel effect is overall weaker. The contrast steps of 10 mm PMMA are reproduced comparatively flat. Nevertheless the inhomogeneous exposure causes an offset variation of about 5% for the line profiles through steps at the edge of the image.

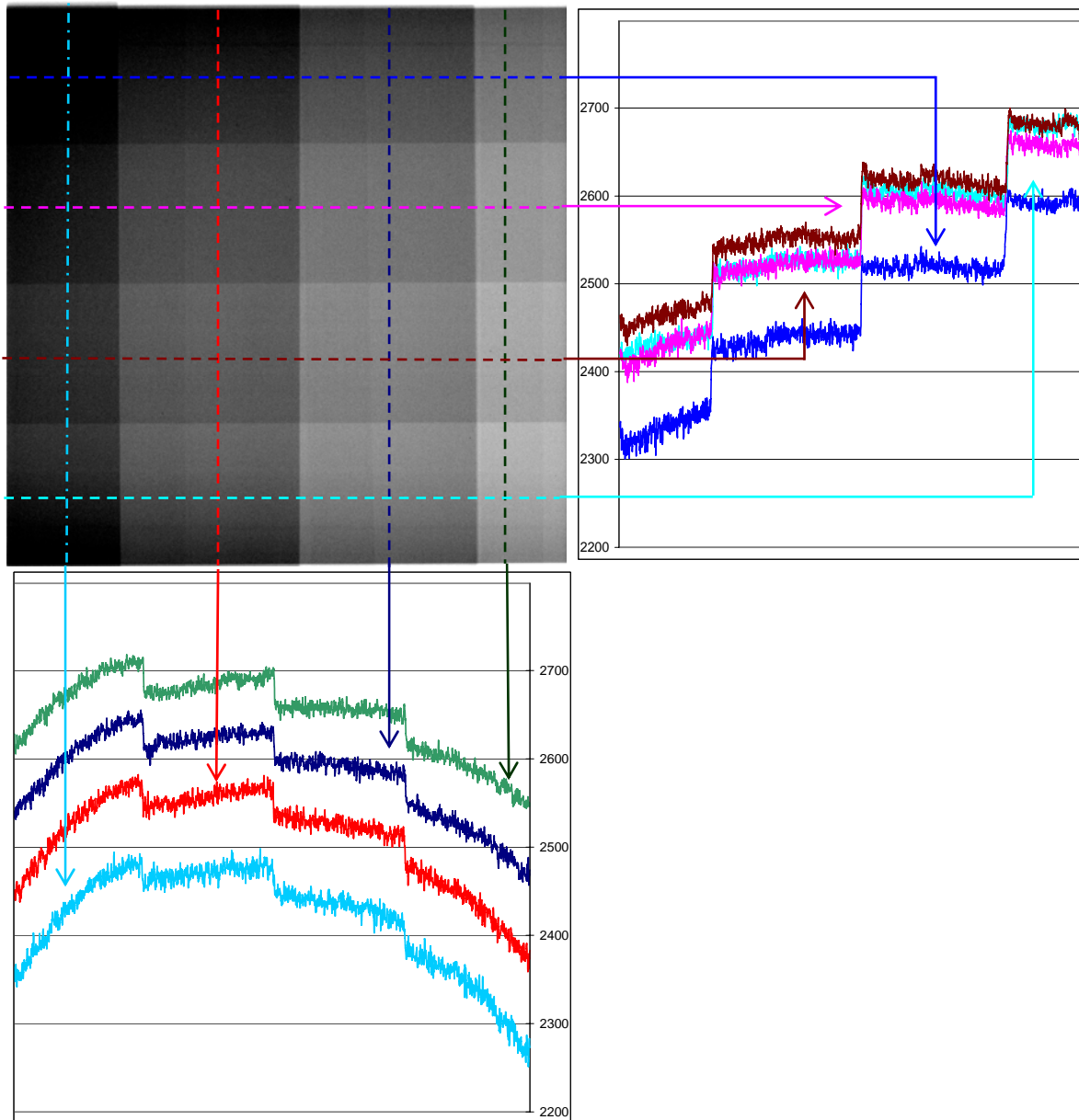


Figure 6.2-2: The heel effect visualized by appropriate settings of window level (brightness and contrast). Line profiles averaged over five parallel lines show the changes quantitatively.

In order to reduce influences of the heel effect each step was individually analyzed: The image data allowed linear fits to the mean change of pixel values in the two directions parallel to the edges of each step. The fits were combined to a bilinear function for the construction of a background matrix that could be subtracted from the image data (Figure 6.2-3, right).

This procedure is important for the statistical evaluation of the image. The standard deviation calculated from a region of interest gives comparable information about the noise properties only if there is no monotonous change in this region.

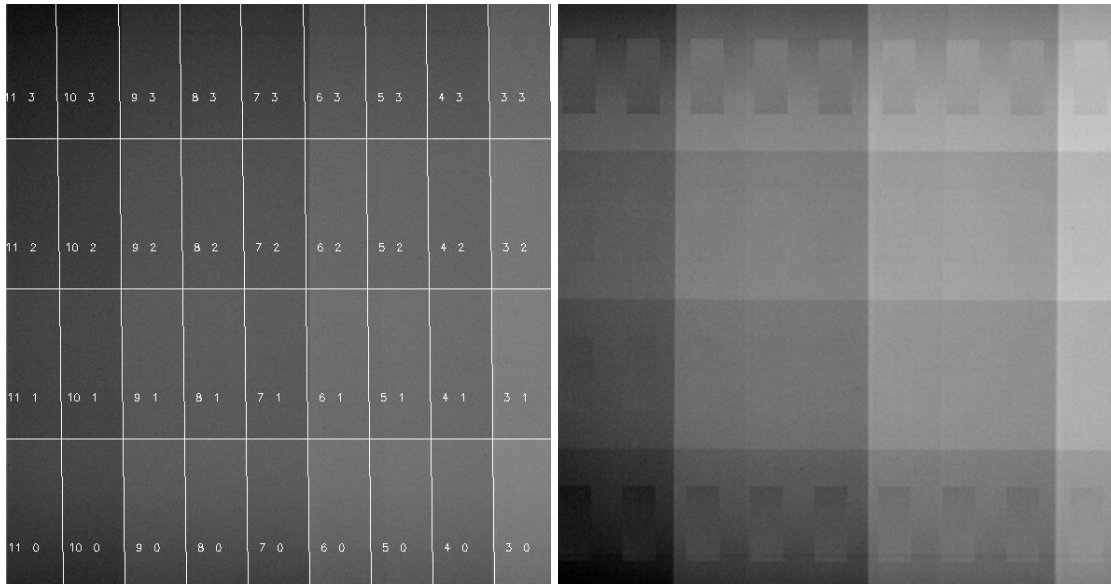


Figure 6.2-3: Separation of the central area of an image (left); the central part of each area is selected and corrected for the heel effect (right) before the used for image analysis.

The readout systems of the CR systems in use have been set to output of RAW data in order to achieve as far as possible straight information what was detected by the image plate. Differences resulting from changes of the radiation quality should not be equalized by post processing of the image data. Nevertheless it is not possible to fully avoid image processing included. It will be seen from the results that there are automated adjustments included in the different CR readers, e.g. the adaptation of the laser stimulating the photoemissions to the overall exposure. The available data about these processes is very limited as it involves confidential manufacturer information. Evaluation of images has to take into account that there are differences resulting from changes of reading system settings to be expected.

As mentioned before the heel effect influences the beam quality and the local exposure of the image. Although they were partly compensated for, these influences have to be kept in mind for in the evaluation of the experimental results, too.

6.3 Imaging Properties of Clinical CR Systems

The imaging properties of two CR systems are presented below in detail. One of them had a conventional powdered phosphor screen and the other one a needle structured phosphor screen (cf. section 6.2).

For the evaluation of the mean pixel values at different tube voltages they are divided by the input dose (cf. Table 6.1-1) in order to compensate for changes due to different exposure levels (Figure 6.3-1 and Figure 6.3-2).

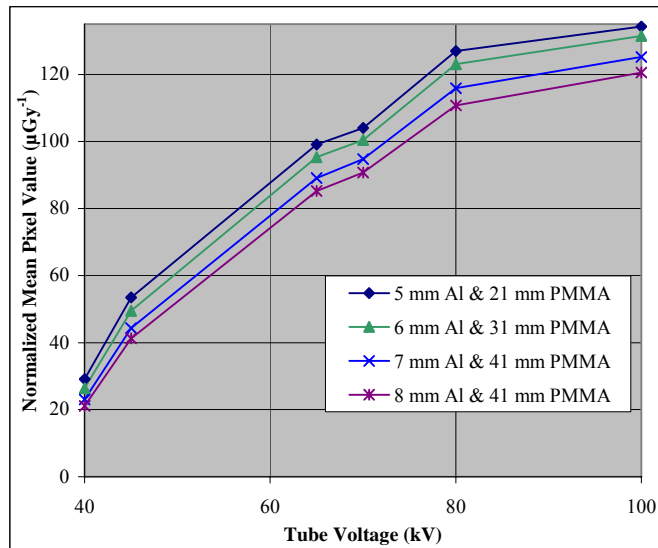


Figure 6.3-1: Rise of the mean pixel value of a standard CR system with the tube voltage.

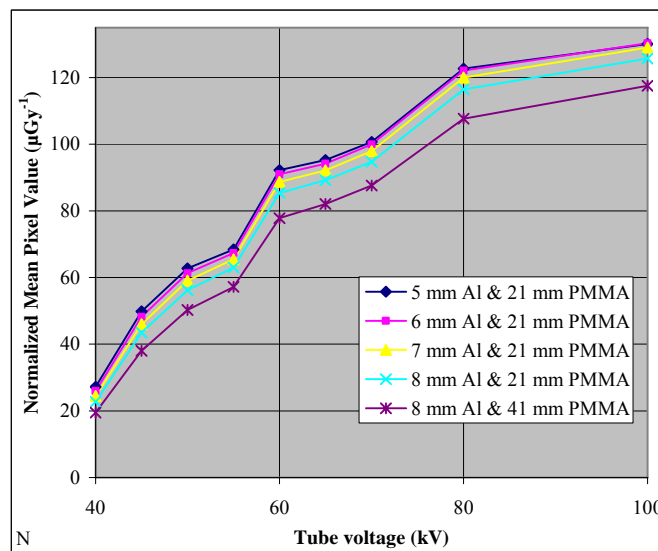


Figure 6.3-2: Rise of the mean pixel value of a needle structured CR systems with the tube voltage.

The rise of the pixel values for exposure with higher energies is clearly seen. The influence of the different step thicknesses is in comparison much smaller. The non-smooth behavior is attributed to image preprocessing: Histogram analysis shows that the detector systems delivers pixel values of a fixed range for all different exposures. The readout of the system is obviously fit into a pixel array of 12-bit depth by an image preprocessing algorithm. The additional presence of K-absorption edges in the detector material (e.g. Cesium at 36.0 keV) seems to interfere with the behavior of the preprocessor to non-smooth behavior of the pixel values vs. energy (e.g. at a tube voltage above 60 kVp for the needle CR system). The effect is damped by the width of the applied x-ray spectra.

The standard deviation of the pixel values is expected to rise with the square root of the applied dose. Therefore all values (Figure 6.3-3 and Figure 6.3-4) are to be divided by the square root of the input dose (cf. Table 6.1-1) for their comparability. As continuous changes of the background have been directly compensated for (see 6.2) the standard deviation is taken as a measure of noise.

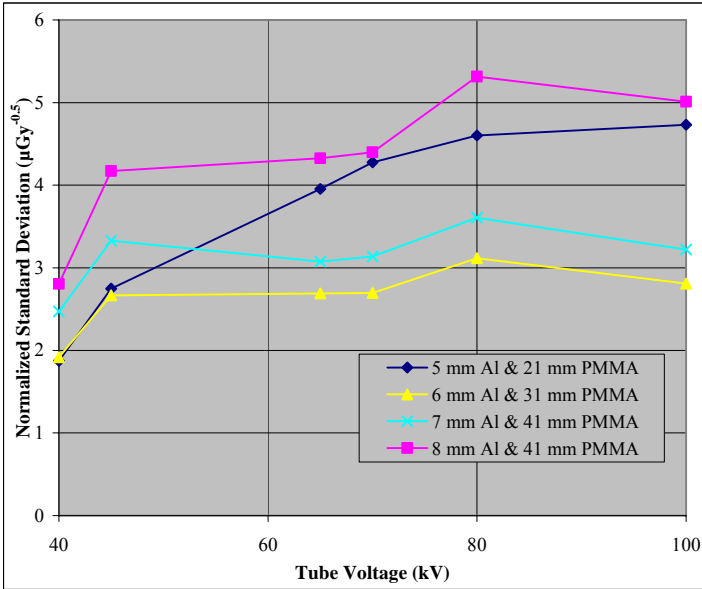


Figure 6.3-3: Change of noise properties of a standard CR system with tube voltage for differently thick absorbers of PMMA and aluminum.

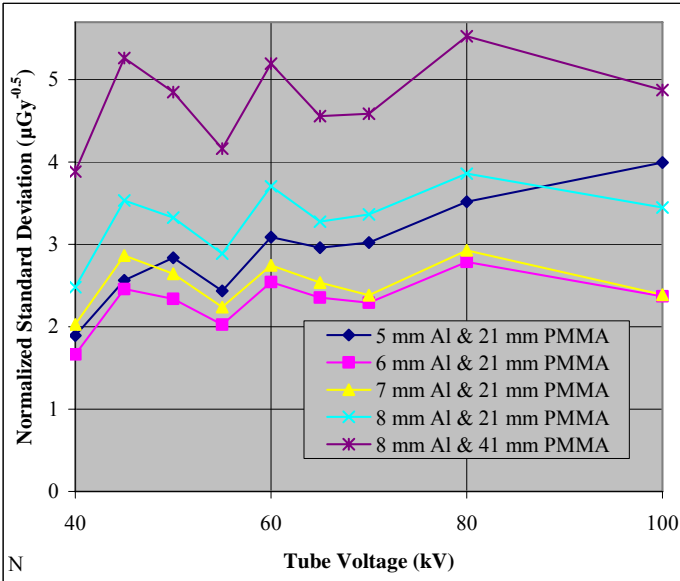


Figure 6.3-4: Change of noise properties of a needle CR system with tube voltage for differently thick absorbers of PMMA and aluminum.

It is seen that the noise level rises with the applied tube voltage. This is expected due to the Poisson characteristics of the process and the higher number of quanta reaching the detector at higher energies. The strongest rise is connected to the thinnest step. Again the graphs show non monotonic behavior which can be attributed to image pre-processing and detector spectral effects.

Also for the contrast (Figure 6.3-5) the influence of the input dose has to be compensated: the values read from the image data are divided by the input dose (cf. Table 6.1-1).

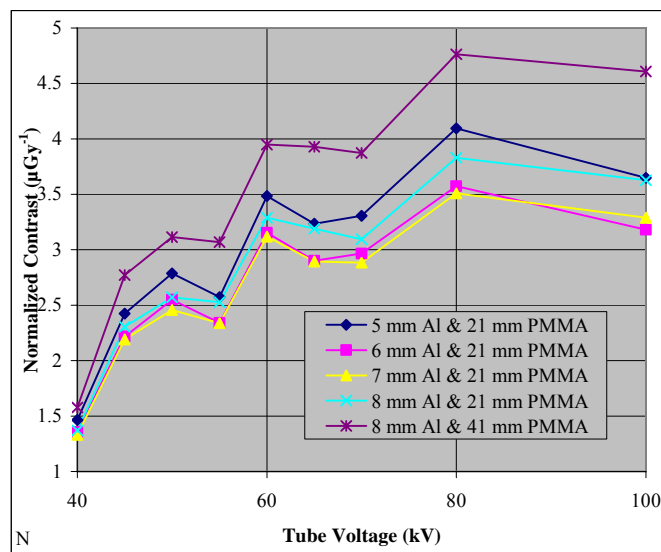


Figure 6.3-5: Contrast by 9 mm PMMA at different tube voltages normalized to the same input dose level (cf. text) behind differently thick main absorbers (see legend).

The result shows similar behavior as the standard deviation especially considering the non monotonic behavior. The contrast rises with higher applied tube voltage; the rise is strongest for the thickest step.

In order to find a measure of image quality the contrast has to be set into relation with the present image noise. This eliminates effects like linear changes of the grayscale. The results for the contrast to noise ratio (CNR; Figure 6.3-6) include normalization by division by the square root of the input dose (cf. Table 6.1-1).

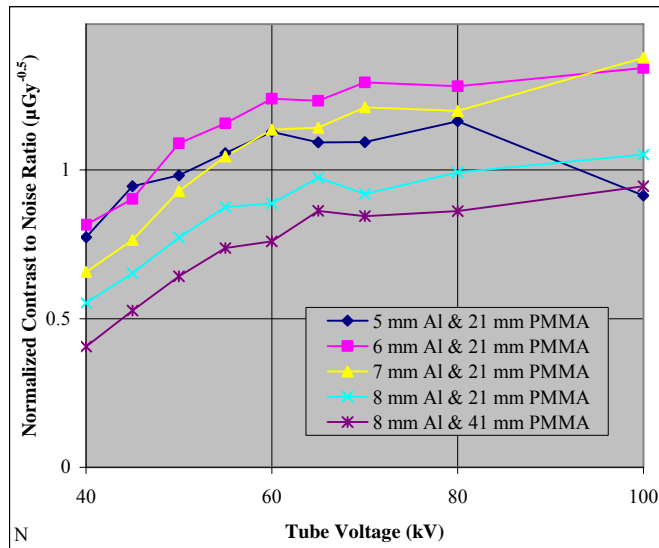


Figure 6.3-6: Contrast noise ratio by 9 mm PMMA at different tube voltages normalized to one input dose level (cf. text) behind differently thick main absorbers (see legend).

The individual non-monotonous behaviors of contrast and noise cancel each other out to some extent. This - in addition to the histogram analysis of the datasets mentioned above - indicates mathematical algorithms acting parallel on the contrast and noise properties.

As expected from the simulations performed (cf. section 5.1.5.3) the contrast to noise ratio rises at low energies with higher transmission through the main absorbing layers, the thinner the step the faster the rise. At higher energies the rise of the transmission through the contrast step becomes the dominant process. The contrast step used was relatively thick (9 mm PMMA) as thinner ones did not deliver a contrast high enough for evaluation. Therefore the falling CNR at high energies as predicted by the simulations is not reproduced. The curves shown in Figure 6.3-6 should be sorted by the overall thickness, the thickest curve lowest especially for low tube voltages. The different position of the curve of the thinnest step structure as well as the bend of this and one other curve towards their 100 kV value are attributable to inhomogeneous behavior of the preprocessing system. Apart from those deviations the CNR at low energies is best behind the thinner steps as expected: It is harder to detect a fixed change behind a thicker layer (cf. chapter 5.2).

In summary the clinical experiments delivered interesting results about the behavior of x-ray units concerning their switching behavior. To provide spectra with known properties exposure times have to be long or start and end must be realized by a shutter mechanism rather than by turning on the tube itself. The results of the simulations (cf. chapter 5.1) and calculations (cf. chapter 5.2) are satisfyingly confirmed. Problems are the relatively wide spectra generated by clinical x-ray tubes that make it difficult to get quantifiable results connected to the radiation

energy. A larger distance of the source from specimen and detector would reduce the influences of the heel effect. Difficulties concerning the restricted knowledge of properties of the detection systems, the raw data output and especially image preprocessing are harder to solve.

7 Conclusions and Outlook

7.1 Conclusion

Pediatric radiography of the thorax was examined in Monte Carlo simulations to calculate conversion factors for dose calculations at different radiation qualities. The dose absorbed by an organ gets highest with photon energies sufficiently high for the transmission into the depth of their location in the body but still low enough for local absorption. In the energy range of clinical relevance no severe change of the exposure of the organs was observed at a fixed entrance dose level.

The Monte Carlo simulation system has been used further in order to obtain spatially resolved transmission properties of a pediatric patient and especially the thoracic region. The patient was represented by a resized three-dimensional dataset obtained from tomographic data of a real patient (voxelmodel). The method was used in order to adapt a step phantom to the transmission behavior found and to compare the results. Evaluations of the imaging are restricted to medium resolution by the size of the volume elements of the voxelmodel and by computation power. For large area properties of imaging the simulations of step like structures delivered results in good agreement with analytical model calculations as well as in reasonable consistence with experimental data obtained with clinical x-ray systems.

The energy dependence of organ absorbed doses was found in a first view very similar to the energetic optimization of imaging, where enough quanta have to reach through to the detecting system but also have to be absorbed by the contrast elements to be imaged and by the detector. The optimal energy for enough transmission through the whole patient and absorption in a detecting system is expected to be higher than the one leading to highest absorbed dose in an organ especially if it is located close to the radiation entrance side of the patient. The calculation of the optimal spectral composition of radiation used for imaging has to take into account the properties of the object to be visualized as well as the generation and characteristics of scatter radiation in addition to the transmission and absorption properties of specimen and detector. These properties were included into a mathematical model for the calculation of optimal imaging. Further the definition of a basic imaging task and the desired security for the correct result allows the absolute quantification of the exposure needed. The highest exposure is always needed for the lowest contrast to be resolved in a thick or dense part of a patient. Calculations show that the optimal range of energy becomes tighter for thinner specimens. This stresses the need for radiation quality optimization especially in

pediatric radiology. A first step would be the adaptation of the energy to the part of highest absorption that needs to be accurately imaged and the adaptation of the exposure to the contrast causing the lowest change of this absorption. Of course more sophisticated optimization would compare exposure levels needed for different regions at different energies and include the expected dose absorbed by different organs and their sensitivity. Perfect optimization of large area imaging like the whole thorax region will lead to parameters just solving the most challenging part the image needs to visualize. If exposure level and energy enable to see a detail of the most difficult combination of low contrast and high overall absorption information about all other parts of the image are sufficiently represented in the image dataset.

Beyond this a local adaptation of the radiation properties similar to the slice specific tube current modulation in computed tomography [90] might be possible. The connected scenario of scanning the examination area pixel by pixel demands radiation sources of high intensity. With the use of a conventional X-Ray tube and restricting the exposure to single pixels by a movable aperture would approximately require the exposure times now used for whole images for every single pixel. This would lead to an acquisition time of more than an hour for a picture of $2000 * 2000$ pixels taken at 1 ms per pixel. A significant advantage would be gained on the other hand as the noise background from scatter radiation from the neighboring pixels is not generated. The effect is used similarly in slot scan scatter rejection techniques. Additionally the analysis of the scattering fraction detected by pixels not under direct illumination could deliver further information about specimen properties.

Here the aim was the optimization of digital radiography of a one-shot exposure. The calculations showed that there is just a relatively tight range of energy around the optimal value especially for thin specimens. This suggests that just a small part of a conventionally applied tube spectrum leads to a reasonably efficient gain of information.

For example a baby may be accidentally breathing in a 0.1 mm thin bone like object when choking on something while being fed and the object is to be found with 99 % certainty. The detector shall have a sensitive layer of CsI of 50 μm effective thickness effectively detecting every absorbed quantum. If the densest part of the region examined can be assumed to be equal to soft tissue of 4 cm thickness our calculations show that the optimal exposure for the procedure is monoenergetic at 20 keV (cf. section 5.2.2.2). The corresponding transmission through the densest region would be 3.7 %. The minimum of $2.6 \cdot 10^5$ image quanta that would have to be sent through the area of the object is increased by variations of the background (cf. section 5.2.4).

A rise of the highest absorption equal to an additional layer of 2 cm soft tissue would move the optimal energy to 23 keV, the transmission to 3.0 % and the minimum number of quanta to $1.05 \cdot 10^6$.

The optimal energies were found to be independent of the thickness of the material to be detected. The presence of scattering radiation is expected to move them slightly to lower values (cf. section 5.2.4). Anatomical noise can make the detection of the particle impossible even with the highest exposure if its shape projection is similar to anatomical structures or their superposition.

In today's clinical surroundings radiography the application of x-ray tube technology makes use of spectrally wide exposures. Narrowing the spectra by lower the tube voltage settings or application of additional filtration severely lowers the overall intensity of the radiation (cf. Figure 5.1-1). Through the connection between intensity and acquisition time spectra of this kind will have to keep a minimal width in order to be suitable for radiographic examinations.

Experiments and measurements performed at clinical x-ray units delivered results in reasonable coincidence with the Monte Carlo Simulations and model calculations. Effects disturbing the measurement have been identified and partly compensated. Especially the output settings of a CR-system being automatically adjusted make the accomplishment of really unprocessed raw data difficult. It turned out that the spectral and time resolved behavior of an x-ray unit has to be monitored closely past the obvious settings. This was found to be most important when imaging thin objects causes very short exposure times.

7.2 Outlook

As mentioned above the highest effect of optimization of an x-ray imaging process is found for imaging of thin objects of low overall contrast. Pediatric radiography of newborn or premature infants is such a low contrast imaging task.

A high resolution voxelmodel obtained directly from patient data of a premature or newborn child would be highly valuable. It could be used for high resolution imaging simulation. Its size variation should lead to recommendations for the exposure in connection with measures like the patients' thickness or weight.

Higher resolution voxel phantoms could allow realistic imaging simulations and a better adaptation of exposure to the region of the actual diagnostic question. A further adaptation of physical phantoms to the properties of an infant would make further experimental optimization possible.

The results suggest that there is a relatively tight energy optimal for a given imaging task especially for a thin specimen to be examined. Technical difficulties are opposing the generation of tight spectra by x-ray tube technology. Nevertheless individualized exposure with narrower spectra might be possible by thicker filtering and longer exposure times as long as the times do not rise into the range that would impose movement artifacts on the images. Different techniques of monochromatic x-ray generation may lead to further possibilities for the generation of optimal radiation [91].

There was no large change found to be expected in the possible detriment of a low dose exposure over the range of energies of use for clinical relevance. Nevertheless a closer assessment of such a change and its inclusion into the evaluation might change the result for an optimal exposure.

The direct use of clinical x-ray systems led to problems with data acquisition and evaluation. The experiments are not to interfere with daily routine and the possibilities for access to software and hardware is limited. A real scientific digital radiography system enabling exact measurements to provide knowledge about every part of the system will allow the detailed experimental validation of the analytical model and Monte Carlo simulations. Especially more exact measurements of noise properties in connection with high resolution Monte Carlo Simulations would be valuable for the inclusion into the mathematical model.

The optimization of pediatric thoracic radiology has to be based on a statement of pediatric radiologists what has to be seen with how high certainty. The relation of physical and clinical image quality has been confirmed before for thoracic radiography [92-94]. Nevertheless clinical studies are to prove the practical value of the results in pediatrics.

An optimization towards the threshold of seeing what is searched for possibly leads to prevention of secondary diagnoses. In clinical experience there is a chance to find important diagnostic information that none was looking for visualized collaterally on an image. The chance for such findings is minimized in some way by image optimization. This should be examined and needs to be taken into account when optimizing a clinical procedure.

In addition to the optimization of the information content of an image it is stressed that the information is only valuable if it is recognized by the radiologist. This directly leads to the necessity to optimize image processing and visualization [95].

The optimal use of digital detectors in pediatric radiology allows fewer repetitions for thoracic investigations due to better information content and lower doses especially for the youngest patients.

8 List of References

1. United Nations Scientific Committee on the Effects of Atomic Radiation (UNSCEAR), *Sources and effects of ionizing radiation, vol. I: sources. Report to the General Assembly, with annexes*. 2000, United Nations: New York.
2. Zankl, M., et al., *The construction of computer tomographic phantoms and their application in radiology and radiation protection*. Radiation and Environmental Biophysics, 1988. **27**: p. 153-164.
3. Petoussi-Henss, N., et al., *The GSF family of voxel phantoms*. Physics in Medicine and Biology, 2002. **47**: p. 89-106.
4. Becker, J., M. Zankl, and N. Petoussi-Henss, *A software tool for modification of human voxel models used for application in radiation protection*. Physics in Medicine and Biology, 2007(9): p. N195.
5. Schlattl, H., M. Zankl, and N. Petoussi-Henss, *Organ dose conversion coefficients for voxel models of the reference male and female from idealized photon exposures*. Physics in Medicine and Biology, 2007. **52**: p. 2123-2145.
6. Veit, R. and M. Zankl, *Influence of patient size on organ doses in diagnostic radiology*. Radiation Protection Dosimetry, 1992. **43**(1/4): p. 241-243.
7. Veit, R. and M. Zankl, *Variation of organ doses in paediatric radiology due to patient diameter, calculated with phantoms of varying voxel size*. Radiation Protection Dosimetry, 1993. **49**(1/3): p. 353-356.
8. Schlattl, H. and M. Zankl. *Dose distributions for cineangiographic examinations of coronary arteries*. in *The Monte Carlo Method: Versatility Unbounded in a Dynamic Computing World*. 2005. Chattanooga, TN: La Grange Park, USA: American Nuclear Society.
9. Kawrakow, I. and D.W.O. Rogers, *The EGSnrc code system: Monte Carlo simulation of electron and photon transport*. 2003, National Research Council of Canada (NRCC): Ottawa.
10. ICRU, *Image Quality in Chest Radiography*, in *Journal of the ICRU*. 2003, International Commission on Radiation Units and Measurements.
11. ICRP, *1990 Recommendations of the International Commission on Radiological Protection*. 1991, Pergamon Press: Oxford, UK.
12. Cook, J.V., et al., *Key factors in the optimization of paediatric X-ray practice*. The British Journal of Radiology, 2001. **74**: p. 1032-1040.
13. European Commission, *European guidelines on quality criteria for diagnostic radiographic images in paediatrics*, ed. M.M. Kohn, et al. Vol. EUR 16261. 1996, Luxembourg: Office for Official Publications of the European Communities.
14. Mooney, R. and P.S. Thomas, *Dose reduction in a paediatric X-ray department following optimization of radiographic technique*. The British Journal of Radiology, 1998. **71**: p. 852-860.
15. Schneider, K., *Evolution of Quality Assurance in Paediatric Radiology*. Radiat Prot Dosimetry, 1995. **57**(1-4): p. 119-123.
16. Schneider, K., M.M. Kohn, and G. Ernst, *The Derivation of Reference Dose Values to Chest X Rays in Paediatric Radiography*. Radiat Prot Dosimetry, 1998. **80**(1-3): p. 199-201.
17. ICRU, *Medical imaging - the assessment of image quality*. 1995, International Commission on Radiation Units and Measurements: Bethesda, MD.
18. Burgess, A.E., *The Rose model, revisited*. J Opt Soc Am A Opt Image Sci Vis, 1999. **16**(3): p. 633-46.

19. Cunningham, I.A. *Understanding Radiologic Image Quality: A linear Systems Approach*. in *SPIE Medical Imaging 2001*. 2001.
20. Cunningham, I.A. and R. Shaw, *Signal-to-noise optimization of medical imaging systems*. *J Opt Soc Am A*, 1999. **16**(3): p. 621-632.
21. Myers, K.J. and H.H. Barrett, *Foundations of Image Science*. 2004, Hoboken: John Wiley & Sons.
22. Dainty, J.C. and R. Shaw, *Image Science, principles, analysis and evaluation of photographic type imaging processes*. 1974, London, New York, San Francisco: Academic Press.
23. Nyquist, H., *Certain topics in telegraph transmission theory*. Transactions of the American Institute of Electrical Engineers, 1928: p. 617-644.
24. Williams, M., B. , P.A. Mangiafico, and P.U. Simoni, *Noise power spectra of images from digital mammography detectors*. *Medical Physics*, 1999. **26**(7): p. 1279-1293.
25. IEC, *Medical electrical equipment - characteristics of digital X-ray imaging devices - determination of the detective quantum efficiency*. 2003, International Electrotechnical Commission.
26. International Commission on Radiological Protection, *Photon, Electron, Proton and Neutron Interaction Data for Body Tissues*. 1992, International Commission on Radiation Units and Measurements: Bethesda, MD.
27. Turner, J.E., *Atoms, Radiation, and Radiation Protection, Second Edition*. 1995: John Wiley & Sons, Inc.
28. International Commission on Radiation Units and Measurements, *Patient Dosimetry for X-Rays Used in Medical Imaging*. *Journal of the ICRU*, 2005. **5**(2).
29. Seidenbusch, M., *Rekonstruktion von Organ- und Effektivdosen bei konventionellen Röntgenuntersuchungen*, in *Medizinische Fakultät 2006*, Ludwig-Maximilians-Universität: München.
30. Normenausschuß Radiologie (NAR), *Klinische Dosimetrie. Teil 7: Verfahren zur Ermittlung der Patientendosis in der Röntgendiagnostik*. 2003, Deutsches Institut für Normung e.V.
31. Attix, F.H., *Introduction to radiological physics and radiation dosimetry*. 1986, New York: John Wiley & Sons, Inc.
32. Krieger, H. and W. Petzold, *Strahlenphysik , Dosimetrie und Strahlenschutz (Band 1)*. 1992: Teubner Verlag.
33. Hubbell, J.H. and S.M. Seltzer. *Tables of X-Ray Mass Attenuation Coefficients and Mass Energy-Absorption Coefficients*. 2004 July 2004 [cited 2005 March 22]; version 1.4:[Available from: <http://physics.nist.gov/xaamdi>].
34. Regulla, D., et al., *Detection of Elevated RBE in Human Lymphocytes Exposed to Secondary Electrons Released from X-Irradiated Metal Surfaces*. *Radiation Research*, 2001. **155**(5): p. 744-747.
35. Regulla, D., et al., *Enhanced Values of the RBE and H Ratio for Cytogenetic Effects Induced by Secondary Electrons from an X-Irradiated Gold Surface*. *Radiation Research*, 2002. **158**(4): p. 505-515.
36. Regulla, D., et al., *Spatially Limited Effects of Dose and Let Enhancement near Tissue/Gold Interfaces at Diagnostic X Ray Qualities*. *Radiat Prot Dosimetry*, 2000. **90**(1-2): p. 159-163.
37. International Commission on Radiological Protection, *ICRP Publication 103: Recommendations of the International Commission on Radiological Protection*. *Annals of the ICRP*, 2007. **37**(2-3).
38. Cranley, K., et al., *Catalogue of Diagnostic X-Ray Spectra & Other Data*. 1997, Institute of Physics and Engineering in Medicine: York.

39. IEC, *Radiation conditions for use in the determination of characteristics for medical diagnostic X-ray equipment*. 1994, International Electrotechnical Commission.
40. Mould, R.F., *The discovery of radium in 1898 by Maria Sklodowska-Curie (1867-1934) and Pierre Curie (1859-1906) with commentary on their life and times*. Br J Radiol, 1998. **71**(852): p. 1229-1254.
41. United Nations Scientific Committee on the Effects of Atomic Radiation (UNSCEAR), *Ionizing radiation: sources and biological effects. Report to the General Assembly, with annexes*. 1982, United Nations: New York.
42. United Nations Scientific Committee on the Effects of Atomic Radiation (UNSCEAR), *Sources, effects and risks of ionizing radiation. Report to the General Assembly, with annexes*. 1988, United Nations: New York.
43. United Nations Scientific Committee on the Effects of Atomic Radiation (UNSCEAR), *Sources and effects of ionizing radiation, vol. II: Effects. Report to the General Assembly, with annexes*. 2000, United Nations: New York.
44. Geleijns, J., J.J. Broerse, and M.J.P. Brugmans, *Health effects of radiation exposure in diagnostic radiology*. European Radiology Supplements, 2004. **14** (1): p. 19-27.
45. International Commission on Radiological Protection, *1990 Recommendations of the International Commission on Radiological Protection*. 1991, Pergamon Press: Oxford, UK.
46. Wall, B.F., et al., *What are the risks from medical X-rays and other low dose radiation?* Br J Radiol, 2006. **79**(940): p. 285-294.
47. Andreo, P., *Monte Carlo techniques in medical radiation physics*. Physics in Medicine and Biology, 1991. **36**(7): p. 861-920.
48. Raeside, D.E., *Monte Carlo principles and applications*. PHYS. MED. BIOL., 1976. **21**(2): p. 181-197.
49. Metropolis, N. and S. Ulam, *The Monte Carlo Method*. Journal of the American Statistical Association, 1949. **44**(247): p. 335-341.
50. Hammersley, J.M. and D.C. Handscomb, *Monte Carlo methods*. 1979, Norwich: Chapman and Hall Ltd.
51. Kalos, M.H. and P.A. Whitlock, *Monte Carlo Methods, Volume I: Basics*. 1986, New York: John Wiley & Sons, Inc.
52. Jorgensen, W.L., *Perspective on "Equation of state calculations by fast computing machines"*. Theor Chem Acc, 2000(103): p. 225-227.
53. Salvat, F., J.M. Fernandez-Varea, and E. Acosta. *PENELOPE a Code system for Monte Carlo simulation of electron and photon transport*. Paris: Nuclear Energy Agency, Organisation for Economic Co-operation and Development.
54. Pia, M.G., *The Geant4 Toolkit: simulation capabilities and application results*. Nuclear Physics B - Proceedings Supplements, 2003. **125**: p. 60-68.
55. Hendricks, J.S., et al., *MCNPX extensions, version 2.5.0*. 2005, LANL: Los Alamos, USA.
56. Waters, L.S., *MCNPX User's Manual, version 2.3.0*. 2002, Los Alamos National Laboratory: Los Alamos, NM.
57. Verhaegen, F. and J. Seuntjens, *Monte Carlo modelling of external radiotherapy photon beams*. Phys. Med. Biol., 2003. **48**: p. R107-R164.
58. Smith, T., N. Petoussi-Henss, and M. Zankl, *Comparison of internal radiation doses estimated by MIRD and voxel techniques for a 'family' of phantoms*. European Journal of Nuclear Medicine, 2000. **27**(9): p. 1387-1398.
59. Zankl, M., et al., *Organ doses for a child in diagnostic radiology: comparison of a realistic and a MIRD-type phantom*, in *BIR Report 20: Optimization of Image Quality and Patient Exposure in Diagnostic Radiology*, B.M. Moores, et al., Editors. 1989, British Institute of Radiology: London, UK. p. 196-198.

60. Zankl, M., N. Petoussi-Henss, and A. Wittmann. *The GSF voxel phantoms and their application in radiology and radiation protection*. in *Workshop on Voxel Phantom Development*. 1996. Chilton, UK: National Radiological Protection Board.
61. Rogers, D.W.O., *Fifty years of Monte Carlo simulations for medical physics*. *Physics in Medicine and Biology*, 2006(13): p. R287.
62. Taranenko, V., M. Zankl, and H. Schlattl. *Voxel phantom setup in MCNPX*. in *The Monte Carlo Method: Versatility Unbounded in a Dynamic Computing World*. 2005. Chattanooga, TN: La Grange Park, USA: American Nuclear Society.
63. Hunt, J.G., et al., *The validation of organ dose calculations using voxel phantoms and Monte Carlo methods applied to point and water immersion sources*. *Radiat Prot Dosimetry*, 2004. **108**(1): p. 85-89.
64. Vilches, M., et al., *Monte Carlo simulation of the electron transport through thin slabs: A comparative study of penelope, geant3, geant4, egsrc and mcnpX*. *Nuclear Instruments and Methods in Physics Research Section B: Beam Interactions with Materials and Atoms*, 2007. **254**(2): p. 219-230.
65. Kawrakow, I. and A. Kawrakow. *EGSnrc Home Page*. [cited 2007; Available from: <http://www.irs.inms.nrc.ca/EGSnrc/home.html>].
66. Seltzer, S.M. and M.J. Berger, *Bremsstrahlung spectra from electron interactions with screened atomic nuclei and orbital electrons*. *Nuclear Instruments and Methods in Physics Research Section B: Beam Interactions with Materials and Atoms*, 1985. **12**(1): p. 95-134.
67. Seltzer, S.M. and M.J. Berger, *Bremsstrahlung energy spectra from electrons with kinetic energy 1 keV-10 GeV incident on screened nuclei and orbital electrons of neutral atoms with Z = 1 - 100**. *At. Data Nucl. Data Tables* ; Vol/Issue: 35:3, 1986: p. Pages: 345-418.
68. ICRU, *Stopping powers for electrons and positrons*. 1984, International Commission on Radiation Units and Measurements: Bethesda, MD.
69. Reilly, J. and D. Sutton, *Report 78 spectrum processor*. 1997.
70. *IDL Version 6.1*. 2004, Research Systems, Inc.
71. International Commission on Radiation Units and Measurements, *Tissue Substitutes in Radiation Dosimetry and Measurement*. 1989, International Commission on Radiation Units and Measurements: Bethesda, MD.
72. International Commission on Radiological Protection, *Basic anatomical and physiological data for use in radiological protection: the skeleton*. 1995, Pergamon Press: Oxford, UK.
73. International Commission on Radiological Protection, *Basic anatomical and physiological data for use in radiological protection: reference values*. 2002, Pergamon Press: Oxford, UK.
74. Cristy, M. and K.F. Eckerman, *Specific absorbed fractions of energy at various ages from internal photon sources, Part I: Methods*. 1987, Oak Ridge National Laboratory: Oak Ridge, TN.
75. Snyder, W.S., M.R. Ford, and G.G. Warner, *Estimates of specific absorbed fractions for monoenergetic photon sources uniformly distributed in various organs of a heterogeneous phantom*. 1978, Society of Nuclear Medicine: New York, NY.
76. ICRU, *Tissue substitutes in radiation dosimetry and measurement*. 1989, International Commission on Radiation Units and Measurements: Bethesda, MD.
77. Zankl, M., *Personal Communication*. 2005 - 2007.
78. Wolfram, S., *Mathematica*. 1988-2003, Wolfram Research, Inc.
79. Yaffe, M.J. and J.A. Rowlands, *X-ray detectors for digital radiography*. *Physics in Medicine and Biology*, 1997. **42**(1): p. 1.

80. Hoeschen, C., et al., *Comparison of technical and anatomical noise in digital thorax X-ray images*. Radiat Prot Dosimetry, 2005. **114**(1-3): p. 75-80.
81. Burgess, A.E., X. Li, and C.K. Abbey, *Visual signal detectability with two noise components: anomalous masking effects*. J Opt Soc Am A Opt Image Sci Vis, 1997. **14**(9): p. 2420-42.
82. Olivo, A., et al., *An innovative digital imaging set-up allowing a low-dose approach to phase contrast applications in the medical field*. Medical Physics, 2001. **28**(8): p. 1610-1619.
83. Schloraka, J.-P., et al., *Coherent scatter X-ray computed tomography in medical applications*. IEEE Nuclear Science Symposium Conference Record, 2002 **2**: p. 900 - 901.
84. Barton, P.G.J., *Contrast Sensitivity of the Human Eye and Its Effect on Image Quality*. 1999, Bellingham, Washington, USA: SPIE - The International Society for Optical Engineering.
85. Rowlands, J.A., *The physics of computed radiography*. Physics in Medicine and Biology, 2002(23): p. R123.
86. Schöfer, H., *Personal Communication*. 2007.
87. *dido 2000 - Bedienungsanleitung*. 2007, Quart GmbH.
88. Leblans, P.J., L. Struye, and P. Willems. *New needle-crystalline CR detector*. in *SPIE Medical Imaging*. 2001.
89. Hoeschen, C., *Das reale Strahlenbild bei einer Röntgenthoraxaufnahme*, in *Faculty of Natural Sciences*. 2002, Otto-von-Guericke University: Magdeburg.
90. Michael, G., M., et al., *Dose reduction in CT by anatomically adapted tube current modulation. I. Simulation studies*. Medical Physics, 1999. **26**(11): p. 2235-2247.
91. Habs, D. *Advanced Photonics for SPARC or other FAIR projects*. in *13th International Conference on the Physics of Highly Charged Ions*. 2007: Journal of Physics: Conference Series.
92. Sandborg, M., et al., *Comparison of model predictions of image quality with results of clinical trials in chest and lumbar spine screen-film imaging*. Radiation Protection Dosimetry, 2000. **90**(1-2): p. 173-176.
93. Sandborg, M., et al., *Demonstration of correlations between clinical and physical image quality measures in chest and lumbar spine screen-film radiography*. The British Journal of Radiology, 2001. **74**: p. 520-528.
94. Sund, P., et al., *Comparison of visual grading analysis and Determination of detective quantum efficiency for evaluating system performance in digital chest radiography*. European Radiology, 2004. **14**(1): p. 48 - 58.
95. Hoeschen, C., Reissberg, S., Döhring, W., *The importance of optimizing the image processing for different digital X-ray detectors to get as much information as possible from the radiographs*. Proceedings of SPIE, 2002. **4682**: p. 828-838.

Appendix

A List of Figures

FIGURE 4.2-1: TYPICAL SHAPE OF A POINT SPREAD FUNCTION.....	10
FIGURE 4.3-1: DOMINANCE OF PHOTOELECTRIC EFFECT (τ) OR COMPTON EFFECT (σ) FOR PHOTONS OF DIFFERENT ENERGY PENETRATING MATTER OF DIFFERENT ATOMIC NUMBER (Z). THE LINE INDICATES EQUAL PROBABILITY FOR BOTH PROCESSES (ADAPTED FROM [32])......	18
FIGURE 4.3-2: LINEAR ATTENUATION COEFFICIENT μ , ENERGY-ABSORPTION COEFFICIENT μ_{en} AND THE CONTRIBUTIONS FROM PHOTOELECTRIC EFFECT τ , COMPTON SCATTERING σ_s , COMPTON ENERGY TRANSFER σ_{tr} AND PAIR-PRODUCTION κ AS FUNCTIONS OF ENERGY FOR PHOTONS IN WATER [27].	19
FIGURE 4.3-3: ANGULAR DISTRIBUTION OF PHOTOELECTRONS IN DEPENDENCE OF THE INCIDENT PHOTON'S ENERGY; THE ARROW INDICATES THE FORWARD DIRECTION [32]......	20
FIGURE 4.3-4: ANGULAR DISTRIBUTION OF ELECTRONS RELEASED IN COMPTON INTERACTIONS IN DEPENDENCE OF THE INCIDENT PHOTON'S ENERGY; THE ARROW INDICATES THE FORWARD DIRECTION [32].	20
FIGURE 4.3-5: ANGULAR DISTRIBUTION OF PHOTONS AFTER COMPTON SCATTERING IN DEPENDENCE OF THE INCIDENT PHOTON'S ENERGY; THE ARROW INDICATES THE FORWARD DIRECTION [32].	21
FIGURE 4.4-1: THE ATTRIBUTABLE LIFETIME RISK FROM A SINGLE SMALL DOSE AT VARIOUS AGES AT THE TIME OF EXPOSURE, (MULTIPLICATIVE MODEL, ASSUMING A DDREF OF 2). THE HIGHER RISK FOR THE YOUNGEST AGE GROUP WILL NOT BE EXPRESSED UNTIL LATE IN LIFE (ADAPTED FROM [45])......	26
FIGURE 4.5-1: PRINCIPLE OF MONTE CARLO CALCULATION OF PHOTON HISTORIES	27
FIGURE 5.1-1: SPECTRA OF AN X-RAY TUBE WITH WOLFRAM CATHODE AND FILTERED BY 3 MM ALUMINUM AND 0.1 MM COPPER, PEAK VOLTAGE FROM 45 kV TO 75 kV.....	32
FIGURE 5.1-2: IMAGING SIMULATION.....	33
FIGURE 5.1-3 ANTERIOR VIEWS OF THE VIRTUAL PHANTOM:	35
FIGURE 5.1-4: STEP PHANTOM OF TWO CROSSED STEP LIKE STRUCTURES SET UP MODULARLY OF PMMA STEPS OF 1 MM AND 10 MM, AND OF ALUMINUM STEPS OF 1 MM AND ADDITIONAL OPTIONAL ALUMINUM LAYERS. ...	41
FIGURE 5.1-5: TRANSMISSION HISTOGRAM OF THE PIXEL VALUES OF AN "ABSORBER" OF 100% TRANSMISSION; E.G. HERE 290 INCIDENT QUANTA PER IMAGE PIXEL RESULT IN A STANDARD DEVIATION OF 6%.	43
FIGURE 5.1-6: CONVERSION COEFFICIENTS FOR EQUIVALENT ORGAN DOSE PER AIR KERMA FREE IN AIR FOR DIFFERENT ORGANS EXPOSED TO PRIMARY RADIATION IN THORACIC RADIOGRAPHY AP WITH SPECTRA OF VARIOUS PEAK VOLTAGES (SPECTRA AS SHOWN IN FIGURE 5.1-1, IRRADIATION GEOMETRY AS SPECIFIED IN SECTION 5.1.1).	44
FIGURE 5.1-7: CHANGE OF CONVERSION COEFFICIENTS FOR EQUIVALENT DOSE PER AIR KERMA FREE IN AIR FOR DIFFERENT ORGANS NOT FULLY EXPOSED TO PRIMARY RADIATION IN THORACIC RADIOGRAPHY AP WITH SPECTRA OF VARIOUS PEAK VOLTAGES (SPECTRA AS SHOWN IN FIGURE 5.1-1, IRRADIATION GEOMETRY AS SPECIFIED IN SECTION 5.1.1)......	45
FIGURE 5.1-8: CONVERSION COEFFICIENTS FOR EQUIVALENT ORGAN DOSE PER AIR KERMA FREE IN AIR FOR DIFFERENT ORGANS EXPOSED TO PRIMARY RADIATION IN THORACIC RADIOGRAPHY AP FOR MONOENERGETIC PHOTONS (IRRADIATION GEOMETRY AS SPECIFIED IN SECTION 5.1.1).	46

FIGURE 5.1-9: CONVERSION COEFFICIENTS FOR EQUIVALENT ORGAN DOSE PER AIR KERMA FREE IN AIR FOR DIFFERENT ORGANS NOT FULLY EXPOSED TO PRIMARY RADIATION IN THORACIC RADIOGRAPHY AP FOR MONOENERGETIC PHOTONS (IRRADIATION GEOMETRY AS SPECIFIED IN SECTION 5.1.1).	46
FIGURE 5.1-10: IMAGING SIMULATION OF THE TRANSMISSION BEHAVIOR OF THE THORACIC REGION OF THE VIRTUAL BABY PHANTOM WITH 10^7 MONOENERGETIC PHOTONS WITH 20 KEV (LEFT), 35 KEV (MIDDLE), AND 50 KEV (RIGHT). THE REGION OF INTEREST FOR THE TRANSMISSION EXAMINATION IS INDICATED BY THE RED FRAME.	47
FIGURE 5.1-11: INVERTED VIEW OF THE SAME IMAGES SHOWN IN FIGURE 5.1-10 (DARK = HIGH PHOTON COUNT).	47
FIGURE 5.1-12: TRANSMISSION OF THE LUNG REGION OF A PEDIATRIC PATIENT AS FUNCTION OF PHOTON ENERGY AVERAGED OVER THE REGION OF INTEREST (CF. FIGURE 5.1-10).....	48
FIGURE 5.1-13: TRANSMISSION HISTOGRAMS OF THE LUNG REGION OF THE VOXEL PHANTOM AT DIFFERENT ENERGIES (KEV) COMPARED TO THE INPUT DISTRIBUTION (LINEAR SCALE).....	49
FIGURE 5.1-14: TRANSMISSION HISTOGRAMS OF THE LUNG REGION OF THE VOXEL PHANTOM AT DIFFERENT ENERGIES (KEV).	49
FIGURE 5.1-15: OVERALL WIDTH OF THE TRANSMISSION HISTOGRAMS PRODUCED BY A SIMULATION OF THORACIC IMAGING OF THE BABY VOXEL PHANTOM VS. ENERGY OF INCIDENT PHOTONS.	50
FIGURE 5.1-16: MONOENERGETIC IMAGING SIMULATION OF 10^7 INCIDENT PHOTONS AT 20 KEV, 30 KEV, 40 KEV AND 50 KEV (FROM LEFT) TO EVALUATE THE TRANSMISSION BEHAVIOR OF A PHANTOM CONSISTING OF A ALUMINUM STEP (3 MM, 2 MM, 1 MM, 0 MM; FROM THE LEFT IN EACH IMAGE) CROSSED WITH A PMMA STEP (10 MM, 20 MM, 30 MM, 40 MM).	51
FIGURE 5.1-17: TRANSMISSION OF DIFFERENT ABSORBER STEPS VERSUS ENERGY OF MONOENERGETIC EXPOSURE. HERE THE AVERAGE NUMBER OF INCIDENT PHOTONS PER IMAGE PIXEL WAS 71.5.	51
FIGURE 5.1-18: ENERGY DEPENDENCE OF THE CONTRAST BETWEEN VARIOUS MAIN ABSORBERS (SEE LEGEND) AND ABSORBERS RESPECTIVELY THICKER BY AN ADDITIONAL LAYER OF 10 MM PMMA (71.5 INCIDENT QUANTA PER IMAGE PIXEL).	52
FIGURE 5.1-19: ENERGY DEPENDENCE OF THE NOISE (AS DEFINED IN SECTION 5.1.1) BEHIND DIFFERENTLY THICK ABSORBERS (SEE LEGEND) WITH AND WITHOUT AN ADDITIONAL CONTRAST ELEMENT OF 10 MM PMMA (FOR 71.5 INCIDENT QUANTA PER IMAGE PIXEL).	53
FIGURE 5.1-20: ENERGY DEPENDENCE OF THE CONTRAST TO NOISE RATIO CNR_e OF A CONTRAST INTRODUCED BY AN ADDITIONAL STEP OF 10 MM PMMA BEHIND DIFFERENTLY THICK ABSORBERS (71.5 INCIDENT QUANTA PER IMAGE PIXEL; THE ERROR BARS EXEMPLIFY RESULTS OF GAUSSIAN ERROR PROPAGATION).	54
FIGURE 5.1-21: COMPARISON OF THE TRANSMISSION CURVE OF A STEP ABSORBER PHANTOM TO THE AVERAGE TRANSMISSION OF THE THORAX REGION OF THE RESIZED VOXELMODEL “BABY” (CF. SECTION 5.1.2).	55
FIGURE 5.2-1: MODEL OF A TRANSMISSION IMAGING SYSTEM WITHOUT SPATIAL RESOLUTION.	57
FIGURE 5.2-2: EXPONENTIAL AND OVER EXPONENTIAL RISE OF INPUT PHOTONS N NEEDED WITH THE DESIRED LEVEL OF CERTAINTY S FOR A CORRECT DETERMINATION OF THE MAIN ABSORPTION OF $p=50\%$ AT $C=99\%$	63
FIGURE 5.2-3: OVER EXPONENTIAL RISE OF N WITH THE TRANSMISSION C OF THE LAYER DEFINING THE CONTRAST.	64
FIGURE 5.2-4: COUPLED CHANGE OF TRANSMISSION OF THE MAIN ABSORBER P AND THE CONTRAST ABSORBER C REPRESENTING HOMOGENEOUS BODIES OF DIFFERENT THICKNESSES. THE THICKNESS OF CONTRAST DEFINING LAYER IS $1/69$ OF THE THICKNESS OF THE MAIN ABSORBER IN THE DATA SHOWN ($k=69$).	65

FIGURE 5.2-5: NUMBER OF PHOTONS N NEEDED FOR THE DISCRIMINATION OF A CONTRAST TRANSMISSION C BEHIND A MAIN ABSORBER OF TRANSMISSION P CONNECTED BY A RATIO OF THICKNESSES OF 1:69 WHICH LEADS TO $C = 99\%$ AT $P = 50\%$.	65
FIGURE 5.2-6: NUMBER OF PHOTONS N NEEDED FOR THE DISCRIMINATION OF A CONTRAST TRANSMISSION C BEHIND A MAIN ABSORBER OF TRANSMISSION P CONNECTED BY A RATIO OF THICKNESSES OF 1:693 ($k=693$) WHICH LEADS TO $C = 99.9\%$ AT $P = 50\%$.	66
FIGURE 5.2-7: MINIMUM IN THE NUMBER OF PHOTONS N NEEDED FOR THE DISCRIMINATION OF A CONTRAST TRANSMISSION C BEHIND A MAIN ABSORBER OF TRANSMISSION P CONNECTED BY A FIXED RATIO OF THICKNESSES ($k=693$).	66
FIGURE 5.2-8: NUMBER OF PHOTONS NEEDED TO DETECT 100 μM BONE (ICRP) BEHIND DIFFERENTLY THICK BLOCKS OF SOFT TISSUE (ICRP) DIVIDED BY THE RESPECTIVE MINIMAL VALUE VERSUS TRANSMISSION OF THE SYSTEM.	67
FIGURE 5.2-9: NUMBER OF PHOTONS NEEDED TO DETECT 100 μM BONE (ICRP) BEHIND A BLOCK OF SOFT TISSUE (ICRP) WITH AN IDEAL DETECTOR.	68
FIGURE 5.2-10: NUMBERS OF PHOTONS NEEDED TO DETECT 100 μM BONE (ICRP) BEHIND DIFFERENT THICKNESSES OF SOFT TISSUE (ICRP) WITH AN IDEAL DETECTOR DIVIDED BY THEIR RESPECTIVE MINIMUM VALUE.	68
FIGURE 5.2-11: NUMBER OF PHOTONS NEEDED TO DETECT 100 μM BONE (ICRP) BEHIND A BLOCK OF SOFT TISSUE (ICRP) DIVIDED BY THE RESPECTIVE MINIMUM VALUE VERSUS THE ENERGY NORMALIZED TO THE ENERGY OF THE MINIMUM.	69
FIGURE 5.2-12: MINIMUM IN THE NORMALIZED NUMBER (SEE TEXT) OF PHOTONS NEEDED TO DETECT 100 μM BONE (ICRP) BEHIND A BLOCK OF SOFT TISSUE (ICRP) VERSUS THE NORMALIZED ENERGY (SEE TEXT).	69
FIGURE 5.2-13: NUMBER OF PHOTONS NEEDED TO DETECT BONE (ICRP) LAYERS OF THREE DIFFERENT THICKNESSES BEHIND A BLOCK OF 4 CM SOFT TISSUE (ICRP) WITH AN IDEAL DETECTOR.	70
FIGURE 5.2-14: NUMBER OF PHOTONS NORMALIZED TO THEIR RESPECTIVE MINIMUM VALUE NEEDED TO DETECT BONE (ICRP) LAYERS OF THREE DIFFERENT THICKNESSES BEHIND A BLOCK OF 4 CM SOFT TISSUE (ICRP) WITH AN IDEAL DETECTOR.	70
FIGURE 5.2-15: MINIMUM NUMBER OF MONOENERGETIC PHOTONS NECESSARY TO DETECT A 100 μM BONE LAYER (CORTICAL BONE ICRP) BEHIND 4CM OF SOFT TISSUE. THE DETECTION IS APPROXIMATED BY THE ABSORPTION OF DIFFERENTLY THICK CSI-SCREENS AND AN IDEAL DETECTOR.	71
FIGURE 5.2-16: NUMBER OF MONOENERGETIC PHOTONS NECESSARY TO DETECT A 100 μM BONE LAYER (CORTICAL BONE ICRP) BEHIND DIFFERENT THICKNESSES OF SOFT TISSUE DIVIDED BY THEIR MINIMAL VALUE USING A 50 μM CSI-SCREEN. AT A THICKNESS OF 6CM THERE ARE THREE VIRTUALLY EQUIVALENT MINIMA AT 23 KEV, 34 KEV AND 36 KEV.	72
FIGURE 6.1-1: THE OVERALL VARIATION IN TIME OF THE EFFECTIVE TUBE VOLTAGE FOR AN EXPOSURES LEADING TO $\sim 5\ \mu\text{Gy}$ BEHIND 20 MM PMMA AT DIFFERENT TUBE VOLTAGE SETTINGS (SEE LEGEND).	76
FIGURE 6.1-2: THE POWER UP BEHAVIOR OF THE EFFECTIVE TUBE VOLTAGE FOR AN EXPOSURES LEADING TO $\sim 5\ \mu\text{Gy}$ BEHIND 20 MM PMMA AT DIFFERENT TUBE VOLTAGE SETTINGS (LEGEND SEE FIGURE 6.1-1).	77
FIGURE 6.1-3: THE OVERALL VARIATION IN TIME OF THE EFFECTIVE DOSE RATE FOR AN EXPOSURES LEADING TO $\sim 5\ \mu\text{Gy}$ BEHIND 20 MM PMMA AT DIFFERENT TUBE VOLTAGE SETTINGS (SEE LEGEND FIGURE 6.1-2).	78
FIGURE 6.1-4: THE POWER UP BEHAVIOR OF THE EFFECTIVE DOSE RATE FOR AN EXPOSURES LEADING TO $\sim 5\ \mu\text{Gy}$ BEHIND 20 MM PMMA AT DIFFERENT TUBE VOLTAGE SETTINGS (SEE LEGEND FIGURE 6.1-2).	78

FIGURE 6.1-5: VARIATIONS OF THE EFFECTIVE TUBE VOLTAGE DURING THE EXPOSURE WITH TUBE VOLTAGE SET TO 40 kV.....	79
FIGURE 6.1-6: VARIATIONS OF THE EFFECTIVE DOSE RATE DURING THE EXPOSURE WITH TUBE VOLTAGE SET TO 40 kV.....	79
FIGURE 6.2-1: RADIOGRAPH OF THE PHANTOM OF TWO CROSSED STEP STRUCTURES.....	80
FIGURE 6.2-2: THE HEEL EFFECT VISUALIZED BY APPROPRIATE SETTINGS OF WINDOW LEVEL (BRIGHTNESS AND CONTRAST). LINE PROFILES AVERAGED OVER FIVE PARALLEL LINES SHOW THE CHANGES QUANTITATIVELY.	82
FIGURE 6.2-3: SEPARATION OF THE CENTRAL AREA OF AN IMAGE (LEFT); THE CENTRAL PART OF EACH AREA IS SELECTED AND CORRECTED FOR THE HEEL EFFECT (RIGHT) BEFORE THE USED FOR IMAGE ANALYSIS.....	83
FIGURE 6.3-1: RISE OF THE MEAN PIXEL VALUE OF A STANDARD CR SYSTEM WITH THE TUBE VOLTAGE.....	84
FIGURE 6.3-2: RISE OF THE MEAN PIXEL VALUE OF A NEEDLE STRUCTURED CR SYSTEMS WITH THE TUBE VOLTAGE.	84
FIGURE 6.3-3: CHANGE OF NOISE PROPERTIES OF A STANDARD CR SYSTEM WITH TUBE VOLTAGE FOR DIFFERENTLY THICK ABSORBERS OF PMMA AND ALUMINUM.....	85
FIGURE 6.3-4: CHANGE OF NOISE PROPERTIES OF A NEEDLE CR SYSTEM WITH TUBE VOLTAGE FOR DIFFERENTLY THICK ABSORBERS OF PMMA AND ALUMINUM.....	85
FIGURE 6.3-5: CONTRAST BY 9 MM PMMA AT DIFFERENT TUBE VOLTAGES AT ONE INPUT DOSE LEVEL BEHIND DIFFERENTLY THICK MAIN ABSORBERS (SEE LEGEND).....	86
FIGURE 6.3-6: CONTRAST NOISE RATIO BY 9 MM PMMA AT DIFFERENT TUBE VOLTAGES AT EQUALIZED INPUT DOSE LEVEL BEHIND DIFFERENTLY THICK MAIN ABSORBERS (SEE LEGEND).	87

B Acknowledgements

I thank Prof. Dr. Dr. Herwig G. Paretzke for providing the possibility to conduct this PhD project at his institute of radiation protection and for his supervision of my work, stimulating discussions, valuable advice and excellent leadership of the Institute of Radiation Protection at the GSF.

I thank Dr. Christoph Hoeschen for supporting this project by stimulating discussions, valuable advice and excellent leadership of the medical physics group.

I thank Matthias Greiter for highly enjoyable conversation mutually solving physical and administrative problems connected to our PhD processes.

I thank Maria Zankl for creating and providing the voxelmodel, Dr. Helmut Schlattl for administrative help with the Monte Carlo Code and very helpful discussion.

I thank Janine Becker for helping with IDL based visualization and computer maintenance.

I thank Prof. Dr. Karl Schneider, Mr. Murry Kohn and Dr. Claus-Peter Wallner and the team of the department of pediatric radiology at the “Dr. von Haunersches Kinderspital”, University of Munich (LMU), for their support, providing all the possibilities of a clinical environment, clinical knowledge, valuable advice and clinical datasets.

Dr. Eugen Mangel and his team at the department of radiology at the clinical centre Starnberg for the use of diverse equipment and their advice based on clinical expertise.

I thank my wife, my parents and all my family for their support, for keeping me up and for their strong believe in me. This work is dedicated to them.

By optimizing radiographic imaging this work is part of a program aiming for reduction of patient dose that is supported by the European research project RISC-RAD under contract number FI 6R-CT2003-508842.

C Example of Mathematica Code for Model Calculations

```
(* This Program evaluates how many random samples have to be taken
to distinguish a (Transmission) probability of p from a Transmission
probability p*c;
with a significance greater than s;
p and c are varied synchronously;
the distinction is described by a range p + - delta(c);
p is defined by a certain thickness of one material (e.g. soft
tissue ICRP)
and c by a certain thickness of another material (e.g. cortical bone
ICRP) in order to introduce energy dependent evaluations;
Print commands commented out served for debugging the code;
*)
(*** ** ** ** ** DEFINITION OF MATERIAL PROPERTIES ** ** *****)
(* Material and Thickness of main absorber (p) *)
(* pdata input as [Energy(MeV),  $\mu/\rho$ ], see "pdata final" below*)
(* 20070413 : NIST data for ICRP SoftTissue *)
pdata = {(* SINGULARITIES NEED TO BE COMMENTED OUT (cf Fit
algorithm) *)
{1.00*10^-03, 3.829*10^+03}, {1.50*10^-03, 1.286*10^+03},
{2.00*10^-03, 5.755*10^+02}, {3.00*10^-03, 1.792*10^+02},
{4.00*10^-03, 7.681*10^+01}, {5.00*10^-03, 3.947*10^+01},
{6.00*10^-03, 2.283*10^+01}, {8.00*10^-03, 9.604*10^+00},
{1.00*10^-02, 4.937*10^+00}, {1.50*10^-02, 1.558*10^+00},
{2.00*10^-02, 7.616*10^-01}, {3.00*10^-02, 3.604*10^-01},
{4.00*10^-02, 2.609*10^-01}, {5.00*10^-02, 2.223*10^-01},
{6.00*10^-02, 2.025*10^-01}, {8.00*10^-02, 1.813*10^-01},
{1.00*10^-01, 1.688*10^-01}, {1.50*10^-01, 1.490*10^-01},
{2.00*10^-01, 1.356*10^-01}};
(* pthickness in cm; pdensity ( $\rho$ ) in g/cm3 *)
pthickness = 10;
pdensity = 1.06;
(* FIT  $\mu$  ALGORITHM *)
(* piecewise fit with {1, x, 1/x, 1/x^2, 1/x^3} decay *)
(* import data *)
fxmuedata = pdata;
(* initial piece *)
```

```

fxmuedatai = Table[fxmuedata[[k]], {k, 1, 3}];
fitfxmuedata[
  x_] = Fit[fxmuedatai, {1, x, 1/x, 1/x^2, 1/x^3}, x]*UnitStep[-(x -
fxmuedatai[[1, 1]])*(x - fxmuedatai[[2, 1])]];
(* All following pieces *)
For[i = 0, i ≤ Dimensions[fxmuedata][[1]] - 3, i = i + 1;
  fxmuedatai = Table[fxmuedata[[k]], {k, i, i + 2}];
  fitfxmuedatai[
    x_] = Fit[fxmuedatai, {1, x, 1/x, 1/x^2, 1/x^3}, x]*UnitStep[-(x -
fxmuedatai[[2, 1]])*(x - fxmuedatai[[3, 1])]];
  fitfxmuedata[x_] = fitfxmuedata[x] + fitfxmuedatai[x];
  ]
(* EXPORT FUNCTION *)
fpdata[x_] = fitfxmuedata[x] ;
(* END OF FIT μ ALGORITHM *)
(* trmfp : TransmissionFunction[Energy (keV)] calculated as exp[-
(μ/ρ)*ρ*pthickness]*)
trmfp[ergy_] = Exp[-fpdata[ergy/1000]*pdensity*pthickness];
Plot[trmfp[ergy], {ergy, pdata[[1, 1]]*1000,
pdata[[Dimensions[pdata][[1]], 1]]*1000}, AxesOrigin -> {0, 0},
  AxesLabel -> {"Energy (keV)", "Transmission p"}, PlotRange ->
{Automatic, Automatic}];

(* Material and Thickness of contrast absorber (c) *)
(* cdata input as [Energy(MeV), μ/ρ], see "cdata final" below*)
(* 20070413 : NIST data for ICRP CorticalBone *)
cdata = {(* SINGULARITIES COMMENTED OUT
{1.00*10^-03, 3.781*10^+03}, {1.03542*10^-03, 3.452*10^+03},
{1.07210*10^-03, 3.150*10^+03}, {1.07210*10^-03, 3.156*10^+03},
{1.18283*10^-03, 2.434*10^+03}, {1.30500*10^-03, 1.873*10^+03},
{1.30500*10^-03, 1.883*10^+03}, {1.50000*10^-03, 1.295*10^+03},
{2.00000*10^-03, 5.869*10^+02}, {2.14550*10^-03, 4.824*10^+02},
{2.14550*10^-03, 7.114*10^+02}, {2.30297*10^-03, 5.916*10^+02},
{2.47200*10^-03, 4.907*10^+02}, {2.47200*10^-03, 4.962*10^+02},
{3.00*10^-03, 2.958*10^+02}, {4.00*10^-03, 1.331*10^+02},
{4.03810*10^-03, 1.296*10^+02}, {4.03810*10^-03, 3.332*10^+02},
*){5.00*10^-03, 1.917*10^+02}, {6.00*10^-03, 1.171*10^+02},
{8.00*10^-03, 5.323*10^+01}, {1.00*10^-02, 2.851*10^+01},

```

```

{1.50*10^-02, 9.032*10^+00}, {2.00*10^-02, 4.001*10^+00},
{3.00*10^-02, 1.331*10^+00}, {4.00*10^-02, 6.655*10^-01},
{5.00*10^-02, 4.242*10^-01}, {6.00*10^-02, 3.148*10^-01},
{8.00*10^-02, 2.229*10^-01}, {1.00*10^-01, 1.855*10^-01},
{1.50*10^-01, 1.480*10^-01}, {2.00*10^-01, 1.309*10^-01}}
(* cthickness in cm; cdensity ( $\rho$ ) in g/cm3 *)
cthickness = 0.01;
cdensity = 1.92;
(* FIT  $\mu$  ALGORITHM *)
(* piecewise fit with {1, x, 1/x, 1/x^2, 1/x^3} decay *)
(* import data *)
fxmuedata = cdata;
(* initial piece *)
fxmuedatai = Table[fxmuedata[[k]], {k, 1, 3}];
fitfxmuedata[x_] = Fit[fxmuedatai, {1, x, 1/x, 1/x^2, 1/x^3},
x]*UnitStep[-(x - fxmuedatai[[1, 1])*(x - fxmuedatai[[2, 1]])];
(* All following pieces *)
For[i = 0, i ≤ Dimensions[fxmuedata][[1]] - 3, i = i + 1;
  fxmuedatai = Table[fxmuedata[[k]], {k, i, i + 2}];
  fitfxmuedatai[x_] = Fit[
  fxmuedatai, {1, x, 1/x, 1/x^2, 1/x^3}, x]*UnitStep[-(
  x - fxmuedatai[[2, 1])*(x - fxmuedatai[[3, 1]])];
  fitfxmuedata[x_] = fitfxmuedata[x] + fitfxmuedatai[x];
]
(* EXPORT FUNCTION *)
fcdata[x_] = fitfxmuedata[x];
(* END OF FIT  $\mu$  ALGORITHM *)

(* trmfc : TransmissionFunction[Energy (keV)] calculated as exp[-
( $\mu/\rho$ )* $\rho$ *cthickness] *)
trmfc[ergy_] = Exp[-fcdata[ergy/1000]*cdensity*cthickness];
Plot[trmfc[ergy], {ergy, cdata[[1, 1]]*1000, cdata[[Dimensions[
  cdata][[1]], 1]]*1000}, AxesOrigin -> {0, 0}, AxesLabel -> {"
  Energy (keV)", "Transmission c"}, PlotRange -> {Automatic,
Automatic}];
(* Print[trmfc[5]]; *)

(* Material and Thickness of sensitive detector layer (det) *)

```



```

(* detdata input as [Energy(MeV),  $\mu/\rho$ ] *)
(* 20070413 : NIST data for CsI *)
detdata =
{{1.00000*10^-03, 9.234*10^+03}, {1.03199*10^-03, 8.653*10^+03},
{1.06500*10^-03, 8.098*10^+03}, {1.06500*10^-03, 8.339*10^+03},
{1.06854*10^-03, 8.281*10^+03}, {1.07210*10^-03, 8.224*10^+03},
{1.07210*10^-03, 8.387*10^+03}, {1.14230*10^-03, 7.344*10^+03},
{1.21710*10^-03, 6.413*10^+03}, {1.21710*10^-03, 6.569*10^+03},
{1.50000*10^-03, 4.132*10^+03}, {2.00000*10^-03, 2.114*10^+03},
{3.00000*10^-03, 7.880*10^+02}, {4.00000*10^-03, 3.836*10^+02},
{4.55710*10^-03, 2.752*10^+02}, {4.55710*10^-03, 5.174*10^+02},
{4.70229*10^-03, 4.851*10^+02}, {4.85210*10^-03, 4.510*10^+02},
{4.85210*10^-03, 5.637*10^+02}, {5.00000*10^-03, 5.296*10^+02},
{5.01190*10^-03, 5.268*10^+02}, {5.01190*10^-03, 7.511*10^+02},
{5.09924*10^-03, 7.193*10^+02}, {5.18810*10^-03, 6.881*10^+02},
{5.18810*10^-03, 7.453*10^+02}, {5.27305*10^-03, 7.196*10^+02},
{5.35940*10^-03, 6.875*10^+02}, {5.35940*10^-03, 7.923*10^+02},
{5.53401*10^-03, 7.323*10^+02}, {5.71430*10^-03, 6.761*10^+02},
{5.71430*10^-03, 7.268*10^+02}, {6.00000*10^-03, 6.448*10^+02},
{8.00000*10^-03, 3.071*10^+02}, {1.00000*10^-02, 1.711*10^+02},
{1.50000*10^-02, 5.815*10^+01}, {2.00000*10^-02, 2.686*10^+01},
{3.00000*10^-02, 9.045*10^+00}, {3.31694*10^-02, 6.923*10^+00},
{3.31694*10^-02, 2.122*10^+01}, {3.45483*10^-02, 2.687*10^+01},
{3.59846*10^-02, 1.719*10^+01}, {3.59846*10^-02, 3.027*10^+01},
{4.00000*10^-02, 2.297*10^+01}, {5.00000*10^-02, 1.287*10^+01},
{6.00000*10^-02, 7.921*10^+00}, {8.00000*10^-02, 3.677*10^+00},
{1.00000*10^-01, 2.035*10^+00}, {1.50000*10^-01, 7.290*10^-01},
{2.00000*10^-01, 3.805*10^-01}};
(* ListPlot[detdata]; *)
(* three detector thicknesses in cm *)
detthicknessa = 0.005;
detthicknessb = 0.01;
detthicknessc = 0.02;
(* detdensity ( $\rho$ ) in g/cm3 *)
detdensity = 4.51;
(* FIT  $\mu$  ALGORITHM including singularities *)
(* singularities in the material data are fit from both sides *)
(* piecewise fit with {1, x, 1/x, 1/x^2, 1/x^3} decay *)

```

```

(* import data *)
fxmuedata = detdata;
(* initial piece *)
fxmuedatai = Table[fxmuedata[[k]], {k, 1, 3}];
fitfxmuedata[x_] = Fit[fxmuedatai, {1, x, 1/x, 1/x^2, 1/x^3}, x]
  *UnitStep[-(x - fxmuedatai[[1, 1])*(x - fxmuedatai[[2, 1]])];
(* All following pieces *)
For[i = 0, i ≤ Dimensions[fxmuedata][[1]] - 3, i = i + 1;
  fxmuedatai = Table[fxmuedata[[k]], {k, i, i + 2}];
  If[fxmuedatai[[2, 1]] == fxmuedatai[[3, 1]], {(* Print["JUMPCASE"];
*)
  (* in case of a singularity move to piece after jump *)
  i = i + 2; fxmuedatai = Table[fxmuedata[[k]], {k, i, i + 2}];
  fxmuedatai = Table[fxmuedata[[k]], {k, i, i + 2}];
  fitfxmuedatai[x_] = Fit[fxmuedatai, {1, x, 1/x, 1/x^2, 1/x^3}, x]
    *UnitStep[-(x - fxmuedatai[[1, 1])*(x - fxmuedatai[[3, 1]])];
  If[fxmuedatai[[2, 2]] > fxmuedatai[[1, 2]] || fxmuedatai[[3, 2]] >
fxmuedatai[[2, 2]], {
  (* Print["DECAY FIT NOT SIUTABLE (switch to linear fit)"]; *)
  fitfxmuedatai[x_] = Fit[Table[fxmuedata[[k]], {k, i, i + 1}], {1,
x}, x]
  *UnitStep[-(x - fxmuedatai[[1, 1])*(x - fxmuedatai[[2, 1]])]
  + Fit[Table[ fxmuedata[[k]], { k, i + 1, i + 2}], {1, x}, x]
  *UnitStep[-(x - fxmuedatai[[2, 1])*(x - fxmuedatai[[3, 1]])];}]
},
{(* regular piece *)
  fitfxmuedatai[x_] = Fit[fxmuedatai, {1, x, 1/x, 1/x^2, 1/ x^3},
x]
  * UnitStep[-(x - fxmuedatai[[2, 1])*(x - fxmuedatai[[3, 1]])];
  (* Print["RegularCase"]; *)});
fitfxmuedata[x_] = fitfxmuedata[x] + fitfxmuedatai[x];
]
(* EXPORT FUNCTION *)
fdetdata[x_] = fitfxmuedata[x] ;
(* Plot[fdetdata[ergy], {ergy, detdata[[1, 1]],
detdata[[Dimensions[detdata][[1]], 1]]}, AxesOrigin -> {0,
0}, AxesLabel -> {"Energy (keV)", "
Absorption CsI"}, PlotRange -> {Automatic, Automatic}]; *)

```

```

(* END OF FIT  $\mu$  ALGORITHM including jumps *)
(* absfdet : AbsorptionFunction[Energy (keV)] calculated as 1 -
  exp[-( $\mu/\rho$ )* $\rho$ *detthickness]*)
absfdeta[ergy_] = 1 - Exp[-
fdetdata[ergy/1000]*detdensity*detthicknessa];
absfdetb[ergy_] = 1 - Exp[-
fdetdata[ergy/1000]*detdensity*detthicknessb];
absfdetc[ergy_] = 1 - Exp[-
fdetdata[ergy/1000]*detdensity*detthicknessc];
Plot[{absfdet[ergy], absfdetb[ergy], absfdetc[ergy]}, {
  ergy, detdata[[1, 1]]*1000,
  detdata[[Dimensions[detdata][[1]], 1]]*1000}, AxesOrigin -> {0, 0},
  AxesLabel -> {"Energy (keV)
", {"Absorption", detthickness *10000, " $\mu\text{m CsI}$ "}, PlotRange -> {
Automatic, Automatic}}];

(*** ** ** ** ** INPUT ** ** ***)
s = 0.99; (* ** value for level of signifcance s ** *)
(* Print[pdata[[1, 1]]]; *)
start = 5; (* (Round[pdata[[1, 1]]*200 - 0.5] + 1)*5.; ** start
value for energy ** *)
incr = 0.2; (* ** increment value for energy ** *)
final = 50; (* Round[pdata[[Dimensions[pdata][[1]], 1]]*200 -
0.5]*5.; *)
      (* ** end value for energy ** *)
step = Round[(final - start)/incr + 0.51];
Print[step, " Absorbtion steps (p&i) from ", start, " to ", final,
"MeV" ]

(*** ** ** ** ** DEFINITIONS ** ** ***)
<< Statistics`NormalDistribution`
Array[b, step];
up := Function[{n, delta}, Min[Floor[n*delta], n]]
(*2007 simplification: exploit symmetries *)
(* dwn := Function[{n, p, delta}, Max[Ceiling[n*(p - delta)], 0]] *)
(*2007 simplification: exploit symmetries *)
(*

```

```

fxbinomi := Function[{n, p, i}, Binomial[n, i]*(p^i)*((1 - p)^(n -
i))]
fxsumbinomi := Function[{n,
p, delta}, Sum[fxbinomi[n, p, i], {i, dwn[n, p, delta], up[n,
p, delta]}]]
*)
fxnormal :=
Function[{n, p, i}, PDF[NormalDistribution[0,
Sqrt[n*p*(1 - p)]], i]]
(* 2007 simplification: exploit symmetries *)
fxsum := Function[{n, p, delta},
fxnormal[n, p, 0] + 2* Sum[fxnormal[n, p, i], {i, 1, up[n,
delta]}]]
(* 2007 simplification: exploit symmetries *)
(* fxsum describes the probability for the result of a sample
experiment of probability p be within the range p - delta to p +
delta through the normal distribution approximation to fxsumbinomi
*)
(* problems at nodes of fit :
Plot[trmfc[ergy], {ergy, 20, 45}, AxesLabel -> {"Energy (keV)",
"Transmission c"},
PlotRange -> {Automatic, Automatic}];
For[i = 49, i ≤ 51, i = i + 0.2, Print[i, ",", trmfc[i], ",",
trmfp[i]];]
Print[trmfp[50.00000001], ",", 1.* trmfp[0.1*500], ",",
1.*trmfp[49.99999]] *)

(* INITIALISATION *)
For[i = 1, i ≤ step, i++, b[i] = {0, 0, 0, 0, 0, 0, 0};]
i = 0;
fxstarttime = AbsoluteTime[];
Print[cthickness, "cm
Cortical Bone (ICRP) behind ", pthickness, "cm Softtissue (ICRP)" ]
Print[]

(* INPUT VALUES AND RECURSIONS *)
Print[Date][[1]], ",", Date[][[2]], ",", Date[][[3]], ",",
Date[][[4]], ",", Date[][[5]], ",", Date[][[6]];]

```

```

Print[]
Print["up , c , p , E , s , n , ", detthicknessa, "cm CsI , ",
detthicknessb, "cm CsI , ", detthicknessc, "cm CsI"]
For[egy = start, egy ≤ final, egy = egy + incr, i = i + 1;
(* avoid problems at nodes of fit *)
egya = egy + 0.000000000001;
p = trmfp[egya];
c = trmfc[egya];; (* c is the contrast defined by an
additional layer of 1/693 of the thickness of the main sample *)
delta = (1 - c)*p/2;
(* delta is half the difference between transmission p and p*c *)
n ∈ Integers; n = 243161; (* startvalue incl. "Ebene -2"*)
(* iteration *)
fxrecursiontime = AbsoluteTime[];
(*Print["beginne Ebene -2 : n= ", n];*)
While[fxsum[n, p, delta] < s, n = n + 210000];; n = n - 210000;
(*Print["Ebene -2 fertig: n= ", n];*)
While[fxsum[n, p, delta] < s, n = n + 21000];; n = n - 21000;
(*Print["Ebene -1 fertig: n= ", n];*)
While[fxsum[n, p, delta] < s, n = n + 7000];; n = n - 7000;
(*Print["Ebene 1 fertig: n= ", n];*)
While[fxsum[n, p, delta] < s, n = n + 3000];; n = n - 3000;
(*Print["Ebene 2 fertig: n= ", n];*)
While[fxsum[n, p, delta] < s, n = n + 1500];; n = n - 1500; (*
Print["Ebene 3 fertig: n= ", n];*)
While[fxsum[n, p, delta] < s, n = n + 500];; n = n - 500;
(*Print["Ebene 4 fertig: n= ", n, "; p=", p, "; delta= ", delta, ";
fxsum=", fxsum[n, p, delta]]];*)
(*a = fxsum[n, p, delta]; Print[a];*)
While[fxsum[n, p, delta] < s, n =
n + 100];; n = n - 100; (* Print["Ebene 5 fertig: n= ", n];*)
While[fxsum[n, p, delta] < s, n = n + 50];; n = n - 50;
(*Print["Ebene 6 fertig: n= ", n];*)
While[fxsum[n, p, delta] < s, n = n + 10];; n = n - 10;
(*Print["Ebene 7 fertig: n= ", n];*)
While[fxsum[n, p, delta] < s, n = n + 1];
(* print & save result *)
(*Print["c=", c, ";delta=", delta, ";p= ", p, ";n=", n, "" ];*)

```

```

(*Print["Für die Bestimmung einer Durchgangswahrscheinlichkeit von
", p, " mit einer
Genauigkeit ", c, " mit einer Sicherheit von P = ", fxsum[n, p,
c]];*)
(*Print["ist eine Bestrahlung mit n = ", n, " Photonen nötig"];*)
ndeta = n/(1000000*absfdeta[egy]);
ndetb = n/(1000000*absfdetb[egy]);
ndetc = n/(1000000*absfdetc[egy]);
Print[c, ",", p, ",", egy, ",", s, ",", n/1000000.,
",", ndeta, ",", ndetb, ",", ndetc];
b[i] = {c, p, egy, s, n/1000000., ndet};
]
Print["Calculation took ", AbsoluteTime[] - fxstarttime, "sec."]

(* Exported text ready for import to spreadsheet program *)

```

D Curriculum Vitae

D.i Contact Information

Felix Schöfer

GSF - National Research Center for Environment and Health, GmbH
Institute of Radiation Protection / Medical Physics

office address: Ingolstaedter Landstraße 1, 85764 Neuherberg, Germany

phone: ++49-89-3187-3463

fax: ++49-89-3187-19-3463

e-mail: felix.schoefer@gsf.de

internet: <http://www.gsf.de/iss/medphys/eng/>

address: Farinellstraße 8, 80796 München, Germany

D.ii Private Information

Date of Birth: 08/05/1977

Place of Birth: Munich, Germany

Citizenship: German

Marital Status: married

D.iii Education

1997 Abitur
(school: Gymnasium Grafing, Jahnstraße 17, 85567 Grafing)

1998-2004 Studies of Physics
Ludwig-Maximilians-Universität München

2000 Vordiplom in Physics
Ludwig-Maximilians-Universität München

2004 Diplom in Physics
Ludwig-Maximilians-Universität München
Thesis Title: "Electron-Phonon-Interaction
in Low-Dimensional Semiconductor Heterostructures"

2004-2007 Doctoral Studies
GSF - National Research Center for Environment and Health
Institute of Radiation Protection, Medical Physics Group
Technische Universität München

Erklärung

Ich erkläre an Eides statt, dass ich die der Fakultät für Physik der Technischen Universität München zur Promotionsprüfung vorgelegte Arbeit mit dem Titel

Optimierung der Relation von Bildqualität und Dosis
in der pädiatrischen Projektionsradiographie

im GSF Forschungszentrum für Umwelt und Gesundheit, Institut für Strahlenschutz

unter der Anleitung und Betreuung durch Prof. Dr. Dr. Herwig G. Paretzke

ohne sonstige Hilfe erstellt und bei der Abfassung nur die gemäß § 6 Abs. 5 angegebenen Hilfsmittel benutzt habe.

Ich habe die Dissertation in keinem anderen Prüfungsverfahren als Prüfungsleistung vorgelegt.

Ich habe den angestrebten Doktorgrad noch nicht erworben und bin nicht in einem früheren Promotionsverfahren für den angestrebten Doktorgrad endgültig gescheitert.

Die Promotionsordnung der Technischen Universität München ist mir bekannt.

München, den 21.11.2007